TOWARDS PROPRIOCEPTIVE GRASPING WITH SOFT ROBOTIC HANDS

By

Thassyo da Silva Pinto

A DISSERTATION

Submitted to
Michigan State University
in partial fulfillment of the requirements
for the degree of

Electrical Engineering—Doctor of Philosophy

2021

ABSTRACT

TOWARDS PROPRIOCEPTIVE GRASPING WITH SOFT ROBOTIC HANDS

By

Thassyo da Silva Pinto

Various robotic hands, gloves, and grippers have been developed for manufacturing, prosthetics, and rehabilitation. However, the use of rigid links and joints presents challenges in control and safe interactions with humans. The emerging field of soft robotics seeks to create machines that are soft, compliant, and capable of withstanding damage, wear and high stress. This dissertation is focused on advancing soft actuators, soft sensors, and perception for ultimately realizing proprioceptive grasping with soft robotic hands.

In this work, several types of soft pneumatic actuators (SPAs) have been tested, fabricated, and tested, including one embedded with 3D-printed conductive polylactic acid (CPLA) layer capable of stiffness tuning and shape modulation. A gripper made of two soft actuators has been prototyped to demonstrate grasping of objects of different sizes and shapes, with desired posture-holding capabilities.

Carbon nanotube (CNT)-based flexible sensor arrays have been designed, fabricated, and integrated to SPAs to provide distributed strain measurements. The presented approach allows customized design of stretchable sensor arrays with varied size and shape. Simulation and experimentation have been performed in order to analyze the soft actuator deformation during bending, and to confirm the capability of the integrated sensor array for capturing the actuator deformation.

3D printing of touch and pressure sensors has been further investigated for potential use in robotic hands. In particular, a novel process has been introduced for producing soft conductors and pressure sensors, involving first 3D-printing microchannels in soft substrates and then filling the channel with liquid metal. With a PolyJet printer, functional straight microchannels have been fabricated with sizes down to 150 $\times$ 150 micrometers in the cross-section area. In addition, spiral-shaped pressure sensors have been developed with a cross-section size of 350 $\times$ 350 micrometers and overall thickness of 1.5 mm (50A and 70A Shore Hardness). Although the sensors require

a relatively large pressure threshold to operate, they have shown the ability to withstand high pressures up to 1 MPa and thus have potential to be used in industrial applications among others.

Finally, preliminary computational exploration of intelligent grasping has been performed. In particular, the classification of soft grasped objects has been examined through a neuroevolution process for artificial brains. Simulation with SOFA (Simulation Open Framework Architecture) has been conducted to produce the emulated contact force measurements, which have been used to train artificial neural networks, including Markov Brains from the Modular Agent-Based Evolver (MABE) platform, to properly classify the shape and stiffness of the grasped objects.

This dissertation is dedicated to my parents, to my brother and to my sisters for loving me unconditionally, for understanding and supporting me in pursuit of my dreams and career aspirations.

ACKNOWLEDGEMENTS

I would like to thank the Department of Electrical and Computer Engineering, the Department of Mechanical Engineering, the Department of Microbiology and Molecular Genetics, the Department of Integrative Biology, and the Institute for Quantitative Health Science & Engineering at Michigan State University. Also, I thank the support of the Smart Microsystems Lab, Adami Lab, and Hintze Lab members that contributed to this dissertation work. This research was supported by Coordenação de Aperfeiçoamento de Pessoal de Nível Superior (CAPES) under the Science Without Borders program (BEX-13404-13-0), National Science Foundation (DBI-0939454, ECCS-1549888, CMMI-1940950), and MSU Foundation Strategic Partnership Grant Program (16-SPG-Full-3236).

PREFACE

Whether its primitive purpose was for throwing rocks or providing enhanced locomotion, the human hand evolved in a way that allows us to perform very complicated tasks such as playing instruments, cooking, crafting and painting. It is true that it takes quite some time to learn fine motor skills, but the hand's complex feedback system plays an important role when training our brain for different manipulation tasks. Moreover, the inherent compliance in human hands provides adaptive grasping of objects with different stiffnesses and shapes. Although automated machines are now capable of executing repetitive manipulation tasks without exhaustion, they can only work with well-defined settings and in very restricted environments. If it is desired for robots one day to leave the manufacturing sites and laboratories to work alongside humans at home or workplaces, advanced manipulation skills will be crucial. The human life has thrived in varying and complex environments, so robots interacting with it will need to have the same dexterous and flexible grasping that humans do.

TABLE OF CONTENTS

LIST OF TABLES

LIST OF FIGURES

LIST OF ALGORITHMS

KEY TO SYMBOLS AND ABBREVIATIONS

AgNW Silver Nanowire

AI Artificial Intelligence

ANN Artificial Neural Network

CAD Computer-Aided Software

CGP Cartesian Genetic Programming

CNT Carbon Nanotube

EGaIn Eutectic Gallium-Indium

ER Evolutionary Robotics

FEM Finite Element Method

GA Genetic Algorithm

HMM Hidden Markov Model

IPA Isopropyl Alcohol

MABE Modular Agent-Based Evolution platform

MB Markov Brain

PDMS Polydimethylsiloxane

PID Proportional-Integral-Derivative

PLA Polylactic Acid

PWM Pulse Width Modulation

SPA Soft Pneumatic Actuator

SOFA Simulation Open Framework Architecture

Chapter 1

Introduction

Grippers are widely used by animals and machines in order to interact with their environment. In biological organisms, different gripper structures were naturally evolved for specific grasping and manipulation tasks, taking multiple forms such as mouth, hands, pincers, beaks, trunks and tentacles. Besides using their natural grippers as organs of action, many animals rely on such mechanisms for exploring their surroundings, which provides the link between a living organism and the world around it.

As the demand for fast, precise and continuous manufacturing processes increased over the years, robots were developed for tasks involving grasping and manipulation of objects in dangerous or unpleasant working conditions in place of human workers. Traditionally, these robotic systems have been composed of rigid bodies made from stiff materials such as metals (steel, aluminum) and ceramics. They are widely applied in industry and can be preprogrammed to execute specific tasks with efficiency, but with constrained adaptability. In order to maintain a safe work environment inside a factory, robots are placed in a different area than humans since their rigid links and joints can be harmful for human interaction. The addition of compliant materials in common actuation mechanisms can lead to the development of safer systems and enable grasping and manipulation of unknow objects.

Soft robotics is an emerging and continuously growing field, which allows applications where

robots can interact with humans safely in factories, in the field or at home [1]. A soft robot is primarily made out of soft and extensible materials such as silicone rubbers [2], synthetic fibers [3] or gels [4], enabling large deformation and absorption of energy generated from impacts. The highly deformable components allow the robotic system to experience theoretically infinite degrees of freedom. In addition, the compliant structure mitigates the impact of the environment uncertainty and produces complex motion with simple control inputs. In contrast to its hard-robotic counterparts, soft robots can be fabricated with simple steps and inexpensive and lightweight materials, and permit mimicry of biological functionalities though their intrinsic elements [5] [6].

Techniques commonly used in robotics for kinematic and dynamic modeling cannot be directly applied to soft robots due to their continuum structure and highly nonlinear deformations. A great challenge for dynamic modeling of soft robots remains due to their heterogeneous body compositions and complex boundary conditions. The investigation of new functional materials with modulated stiffness properties and proprioceptive sensing, as well as novel control schemes for soft sensory-motor devices, will be critical in the development of enhanced soft robotic systems.

1.1 Biological Sensory Signals and Natural Grasping

Sensory receptors are the bridges which connects our minds to the outside world. Different kinds of stimuli (light, sound, temperature, or mechanical deformation) generate electrical signals in the form of symbols which can be interpreted by the central nervous system [7]. In addition, a given sensory receptor, biological or engineered, for example, has a well-defined range of stimuli for a particular response type. Various species have similar underlying sensory mechanisms, but there is a wide variation in the sensitivity spectrum. Previous studies in crustaceans have shown that stretch receptor neurons can register the muscle length [8]. When the receptor muscle is stretched, the detritus become deformed and their membrane potential is reduced. Besides sending information to the nervous system, stretch receptors have direct effects on motoneurons connected to the same muscle group. This feedback system is important to regulation of muscle movement.

The human hand and wrist are comprised of 27 bones, 48 muscles and 22 degrees of freedom [9]. It is a versatile tool capable of executing a variety of basic grasps which have been discussed in medical literature [10]. Moreover, it displays conformability on both large and small scales, since the fingers can curl around objects during grasping, while localized deformation happens at the finger and palm tissues to adapt its surface. Furthermore, our hands are equipped with a great sophisticated sensory system. Its complexity level is evident based on the number of nerves in the hand and the portion of brain dedicated to information processing and movement control [11]. Figure 1.1 shows several skin sensors present on the hand. Sensory receptors located at the hand tissue (skin, muscle, or joints) provide somatic sensations such as touch, pressure, temperature, pain, and position. These somatosensory mechanisms allow us to determine the texture and shape of objects that we palpate.

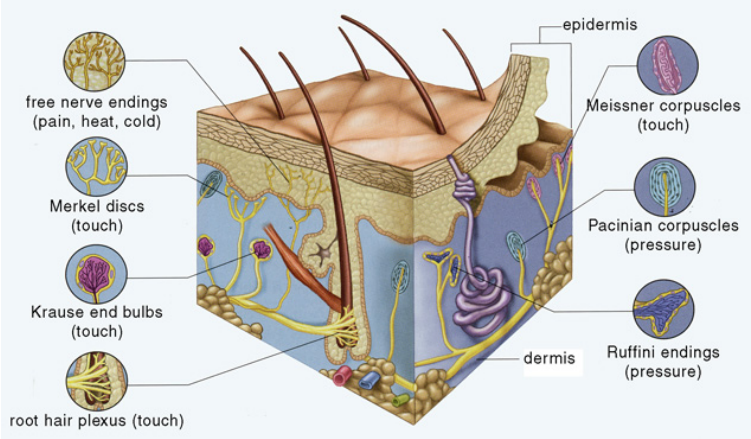

Figure 1.1: Some of the sensors in the skin of a hand and their respective interpreted stimuli such as touch, pressure, and heat (Adapted from [12]).

Many other neural structures play a role in additional important aspects of somatic sensation. The primary motor cortex (M1), which is located in the back of the frontal lobe, is considered as the main site for motor control. Studies concerned with brain activity measurement through functional magnetic resonance imaging (fMRI) have shown that the activation of M1 [13] and the left inferior parietal lobule (IPL) [14] are compulsory for the somatic perception of hand-object interactive movement. With these low-level and high-level feedback loops, the hand can be said to

be an organ with a certain amount of distributed control. Clues about higher aspects of sensory and motor integration involved in human hand grasping tasks will not only contribute to somatosensory studies, but also lead to insightful design and control approaches for a new generation of robotic grippers.

1.2 Robotic Grasping and Soft Robotic Grippers

A robotic gripper design can range from a servo-driven claw with multiple fingers to suction cups powered by vacuum. In industry, grippers may be precise and employed in different workspaces, but they are designed to perform very particular tasks with well-defined parts [15]. Their flexibility is very limited since a magnetic gripper will not be able to pick up thermoplastics, and a suction-based gripper for glass plates is useless for manipulating machined parts. This problem could be solved by having a collection of grippers for a set of tasks; however, there are a few downsides for this approach, such as the high cost to keep an inventory of multiple grippers, interruption of manufacturing process for gripper change, and lack of compatibility for tactile and force sensors across multiple grippers. In fact, tactile sensing is key to dexterous manipulation since it allows the application of feedback-based control algorithms that exploit the sensor signals for techniques such as grasp stability estimation, tactile object recognition and force control [16] (Figure 1.2).

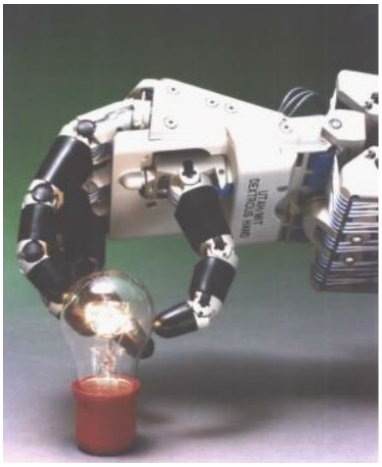

Figure 1.2: The Utah/M.I.T. Dexterous Hand with tendon-driven actuation [16].

As an alternative to rigid mechanisms, grippers with soft structures can be developed for more versatile and adaptive grasping. Its compliance allows higher intrinsic robustness to uncertainty in actuation and perception, reduces the number of elements to be controlled, and offers larger tolerance to external perturbations when manipulating a broad range of objects and conforming to the static environment. Moreover, the fabrication of soft hands is faster and less expensive than their rigid counterparts. For instance, a universal gripper based on the jamming of granular materials [17] can be used to pick up a wide range of different objects through vacuum-induced reversible jamming transitions without sensory feedback. Furthermore, a hydraulic-driven soft gripper for underwater applications enables delicate manipulation and sampling of fragile marine species on the deep reef [18]. A soft robotic approach can also be beneficial in the design of wearable devices for human assistive technologies. Soft robotic gloves driven by pneumatic systems [19] or cable actuation [20] can provide robotic-assisted therapy during post-stroke hand rehabilitation exercises.

Although compliance allows adaptive grasping, it is difficult to estimate the specific configuration of a soft hand or gripper due to its malleability. The information about a robotic gripper configuration can be useful for decision making during manipulation. Not only it can determine if a grasp is successful, but it can also detect a particular object's shape as well as if it is picked up in the desired pose. A 3D convolutional neural network (CNN) can be trained to estimate suitable grasps poses for previously unseen objects by learning features and a classifier from point cloud data [21]. The combination of bending and force sensors on a soft robotic gripper, along with a sensor model and grasping algorithm, can identify an object on a single grasp after characterization and training [22]. Therefore, proprioceptive feedback in soft hands is essential for complex manipulation of objects. This collection of sensory data will enable robots to grasp tools intended for use on a certain orientation (pose), ensure appropriate grasping forces, and plan interaction between the grasped object and its workspace. By achieving seamless grasping interaction with similar dexterity and flexibility as human hands, robots will be able to robustly use tools in different tasks and scenarios.

1.3 Integration of Flexible and Stretchable Sensors

An existing challenge is the integration of sensing devices in the structure of a soft mechanism, for feedback control of the system. Several control schemes for soft robotic systems have been explored by researchers [23][24][25]; however, feedback control of soft robots using compact, integrated sensors is generally limited. The most common methods for sensor measurement in soft robotics are resistive and capacitive technologies [26]. These sensors are usually fabricated using nanoscale conductive materials deposited over a flexible substrate such as polydimethylsiloxane (PDMS), which remains one of the best choices for stretchable sensor substrates due to its flexibility and resistance to high temperatures and chemical processes [27]. 3D microfluidic systems can be easily created in PDMS with complex geometries and topologies, by taking advantage of the fact that PDMS is an elastomer and provides a way of controlling bending, weaving, and braiding through mold templates [28], making them suitable for micro-scale sensor applications. Optical fibers and piezoresistive materials can also be used as soft sensors. A tactile sensor sleeve based on fiber-optic light modulation [29] can be incorporated in the body of a soft manipulator for pressure sensing; however, large instrumentation devices are required for measuring the light intensity variation. Commercially available sensors can be embedded in a soft pneumatic actuator skin [30], but their size and shape cannot be customized for various applications.

Microfluidic devices are another sensing modality that can be embedded into soft robotic structures and actuation mechanisms to provide a closed-loop feedback system. Microfluidics is the science and technology of systems that process or manipulate small amounts of fluids, using channels with dimensions of tens to hundreds of micrometers [31]. Several microfluidic structures have been applied extensively in many sensing applications such as force detection [32][33], strain gauges [34][35], flow rate measurement [36], and noninvasive health analysis [37][38][39]. Current research has identified the deformability and mobility of liquid metals (LMs) in deformable microstructures, which brings significant potential for soft robots and machines [40]. LM alloys such as EGaIn (75.5 wt% gallium and 24.5 wt% indium) [41] and Galinstan (68.5 wt% gallium, 21.5 wt% indium, and 10 wt% tin) [42], have been extensively applied in the design of soft sen-

sors due to their capabilities in simultaneously presenting many unique physical properties such as low melting point, excellent liquidity, high electrical conductivity, good thermal conductivity, low vapor pressure, and low toxicity in comparison to mercury. Some examples of LM-infused microfluidic sensors include wearable soft sensors for human gait measurement [43][44], soft gloves for hand motion detection [45], soft tactile sensors for force feedback in micromanipulation [46], and soft pneumatic actuators with embedded microfluidic sensing [47][48][49]. A number of other methods for patterning liquid metals in 2D and 3D allow the creation of metallic microstructures, stretchable conductors and sacrificial templates for microfluidic channels [50][51][52]. In the near future, it is believed that LM-based soft machines will play many roles in biomedicine and small mechanical systems.

1.4 Artificial Intelligence and Evolutionary Robotics

When machines are capable of performing tasks in an intelligent manner, we usually define this ability as Artificial Intelligence (AI). A vast number of research sub-fields in AI have studied different techniques in achieving intelligent machines, not only for describing aspects of human intelligence, but also with aims to create machines with better performance than humans in well-defined problem settings (playing strategy games, recognize visual or auditory patterns, and driving a car on a crowded street) [53].

An AI model can learn through training data (machine learning) or evolve desired performance based on fitness functions (evolutionary algorithms). In evolutionary systems, a machine is capable of developing other submachines according to their ability to perform tasks in an environment simulating the real word. The theory of evolution was developed in Charles Darwin's On the Origin of Species by Means of Natural Selection (1859), which basically states that variations occur during reproduction, and they will be preserved in successive generations with approximate proportion to their effect on reproductive fitness. A popular method in evolutionary computation is the application of genetic algorithms (GA), where a population of artificial chromosomes (genotype),

encoding the characteristics of an individual (phenotype), selectively reproduces the chromosomes of individuals with higher performance and applying random changes for several cycles (generations).

Similarly, autonomous robots can be automatically created based on a technique called Evolutionary Robotics (ER), where artificial organisms can develop their own skills without human intervention [54]. The general idea behind ER is that an initial population of artificial chromosomes, encoding either the control system or the morphology of a robot, are randomly created and placed in a virtual environment. The fittest robots are selected based on their performance in various tasks, and then allowed to reproduce while applying genetic operations such as mutation, crossover, and duplication. Multiple cycles of this process are repeated until a robot with the desired performance is born (Figure 1.3). This technique has been applied in applications ranging from the evolution of self-organizing behavior in a swarm of robots [55] to evolving gaits for legged robots [56].

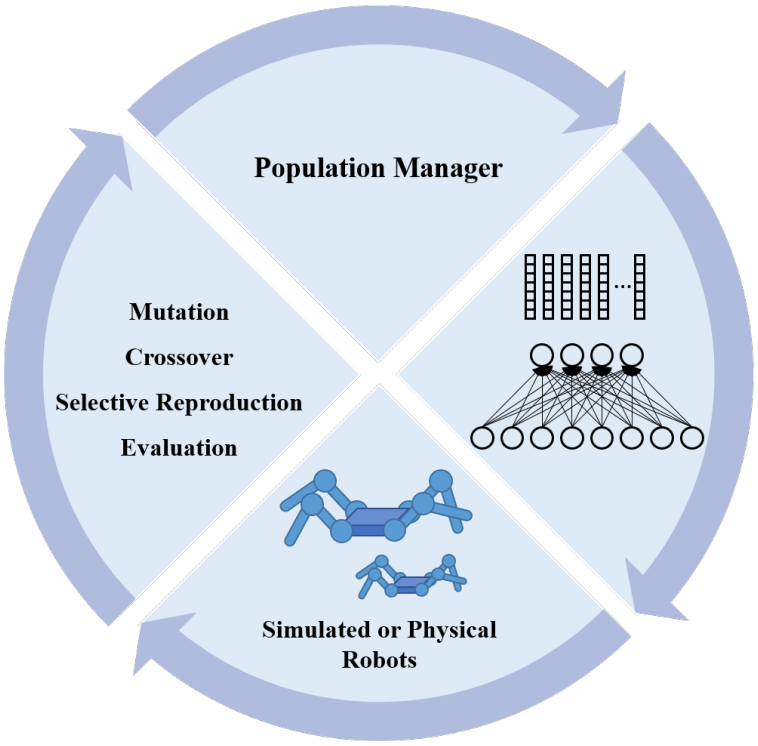

Figure 1.3: Artificial evolution of a population of robots without human intervention.

It is interesting to note that the field of ER is based on a fundamental concept defined as embodied cognition [57], which, instead of viewing intelligence as merely a matter of symbol processing within the brain of a living organism or a control system of a robot, perceives the latter as something arising from the interaction between brain, body, and environment. In addition, certain processes that would originally be performed by the brain can be outsourced to the body by means of morphological computation. In this case, a soft robotic hand can grip a complex object with less control effort due to its material elasticity, providing automatic adaptivity for grasping unknow objects.

Furthermore, an important process in ER studies is the ability to transfer simulated brains (controllers) to real-word robotic systems (transferability). For instance, a simulation tool with voxel-resolution soft, actuatable materials, can evolve soft-bodied robots with multiple body-plans and gaits for different fitness functions, mimic cardiac electrophysiology, generate squeezing for small spaces, and achieve swimming locomotion [58][59][60][61]. However, the transferability process in these computational tools is limited or even impossible due to unmatched parameters between the simulated environment and real-world soft robots. The ability of computational evolution to develop unexpected novel solutions, combined with simulation of realistic material properties, may favor the creation of soft robotic grippers with more natural mobility and enhanced sensory-motor coordination.

1.5 Contributions and Outline

Our vision for achieving robust and adaptable robotic grasping is by means of biological inspiration, sensory feedback (proprioception), soft and stretchable materials (morphological computation), and computational evolution of control systems (embodied intelligence). Here we present contributions for each of those areas, tackling specific aspects involved in the overall challenge of grasping and manipulating objects with a robotic hand. This dissertation is organized as follows:

- **Chapter 2: Materials, Design, Fabrication, Simulation and Controllers for Soft Actuators**

  This chapter describes the first building block in our system. We explain the materials and designs used in the fabrication of soft pneumatic actuators (SPAs). Different investigated processes are described such as soft lithography and 3D-printing, with varied SPA shapes and actuation modes. In addition, we discuss the simulation of these devices using finite element method (FEM), which can be used to study their mechanical behavior prior to fabrication. A custom-built pneumatic platform is used for controlling the SPAs via graphical and embedded software in several experiments. A novel approach for modulating the SPA stiffness is presented, using a 3D-printable conductive PLA (CPLA) material that can be integrated to the SPA structure and used in grasping tasks.

- **Chapter 3: Fabrication, Characterization and Integration of CNT-based Flexible Sensors**

  The integration of sensors within an SPA should allow the measurement of distributed deformation without affecting its advantageous malleability. In line with this reasoning, we have developed a novel type of sensor arrays made of CNT straing gauges and AgNW electrodes via a screen-printing process. A detailed recipe for fabricating and characterizing these sensors arrays is provided. Moreover, we have performed experiments on SPAs with integrated sensor arrays in order to measure each sensor deformation (change in resistance) and estimate the actual SPA curvature during bending. The results show agreement with the observed SPA deformation and provide a first step in the implementation of sensor arrays for localized measurements and feedback control with proprioceptive sensors in soft robotic mechanisms.

- **Chapter 4: 3D-Printing of Liquid Metal-Based Stretchable Conductors and Pressure Sensors**

  Microfluidic devices control fluids on the micrometer-scale and are commonly used for lab-

on-chip applications, such as sensors, micropumps and biological analysis. Commonly reported fabrication methods for achieving flexible microfluidic structures are labor-intensive, require many cumbersome steps, and have limited options for materials. This chapter presents a rapid-manufacturing technique using a PolyJet 3D-printer for creating soft microfluidic substrates embedded with liquid metals to generate stretchable conductors and pressure sensors. By using this novel method, several spiral-shaped soft pressure sensors with multimaterial-based substrates can be 3D-printed simultaneously in less than six minutes. Experiments have revealed that these 3D-printed microfluidic pressure sensors are very robust, capable of withstanding high pressures up to 1 MPa.

- **Chapter 5: Computational Evolution of Controllers for Soft Robots**

  Computationally evolved controllers for soft robotic hands have the potential to identify object shape and hardness or provide pose estimation for decision making tasks. In this chapter, we present some preliminary studies for the classification task of soft grasped objects through neuroevolution processes of artificial brains. A combination of 3D physics engines and digital evolution tools provided a substrate for investigating the classification of several grasping conditions from emulated contact force and pressure measurements. Identified solutions from different evolved AI models are compared. In addition, a road map for achieving fully proprioceptive soft grasping is discussed.

- **Chapter 6: Summary and Discussion**

  This chapter summarizes our contributions and future lines of work presented in this dissertation. Finally, we conclude with some thoughts regarding the remaining challenges in proprioceptive grasping with soft robotic hands.

Chapter 2

Materials, Design, Fabrication, Simulation and Controllers for Soft Actuators

2.1 Elastomeric Materials for Soft Robots

In order to achieve robots that realize deformation with less energy, their body should be fabricated with low modulus materials such as elastomers. A method for measuring the rigidity of a certain material is by determining its Young's modulus (modulus of elasticity), which defines the ratio of stress to percent elongation of prismatic bars (homogenous) subject to axial loading and small deformations [62]. Although soft robots are made from heterogeneous and irregular structures that undergo large deformations, the Young's modulus is valuable information for comparing the rigidity of materials used in the fabrication soft robotic systems (see Figure 2.1). Conventional robots are built out of materials with elastic modulus within the range of 10^9 to 10^{12} Pa (metals or hard plastics). In contrast, natural organisms are often composed of materials within the range of 10^2 to 10^8 Pa (skin or muscle tissue), orders of magnitude lower than the range for traditional robots. This great mismatch prevents rigid robots from interacting directly with humans and biologically compatible systems, whereas provides soft robots a promising opportunity to address these issues.

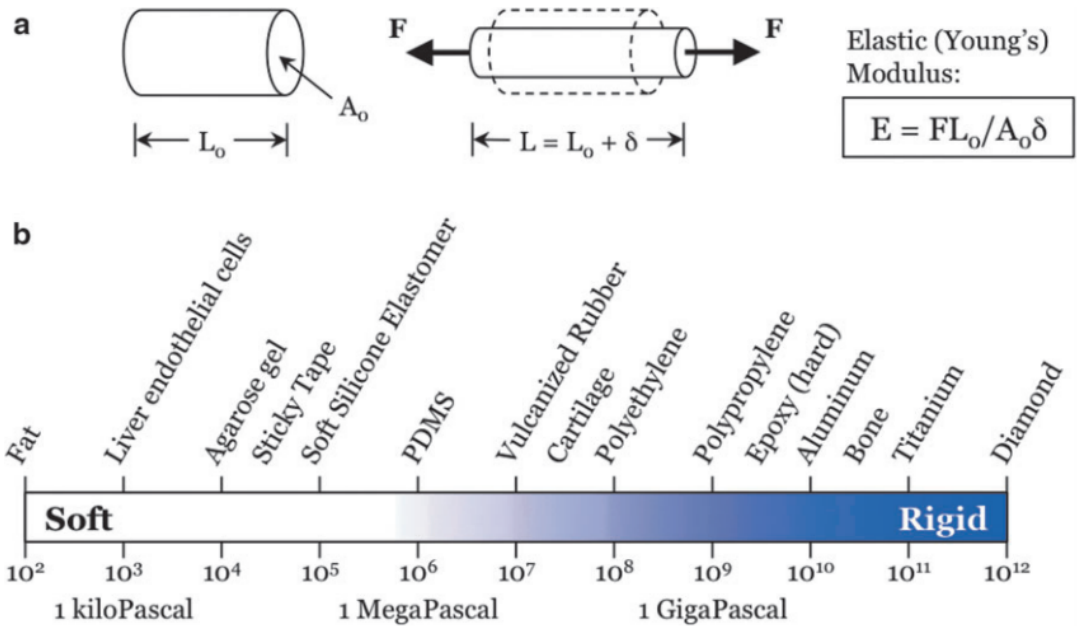

Figure 2.1: Young's moduli of engineered and biological materials. (a) Elongation of a homogenous prismatic bar, and (b) the elastic (Young's) modulus scales for various materials. (Adapted from [62])

Platinum-based silicone-rubbers are often chosen as the basis in the fabrication of soft components due to their low moduli (durometer as low as 05-00), allowing high strains and curing processes at the room temperature. Nevertheless, the modeling of silicone-based structures presents challenges due to their nonlinear nature. The nonlinear theory of elasticity, which constitutes the theoretical basis for the study of hyperelastic materials, uses a strain-energy function to describe in energetic terms the mechanical behavior of this class of materials [63]. For an isotropic material, the strain energy can be described as

$$\Psi_{iso} = \Psi(I_1, I_2, I_3) \tag{2.1}$$

where I_1, I_2, and I_3 are strain invariants

$$I_1 = \sum_{i=1}^{3} \lambda_i^2, \quad I_2 = \sum_{i,j=1}^{3} \lambda_i^2 \lambda_j^2, \quad I_3 = \prod_{i=1}^{3} \lambda_i^2, \quad i \neq j \tag{2.2}$$

with λ_1, λ_2 and λ_3 representing the principal stretches. The hyperelastic material models (Table A1) are more suited to explain the nonlinear behavior of elastomers under the assumption of incompressibility. In the case of uniaxial tension of an incompressible material

$$\lambda_1\lambda_2\lambda_3 = 1, \quad \lambda_2 = \lambda_3 = \lambda^{-1/2}, \quad \lambda_1 = \lambda > 1 \tag{2.3}$$

and the gradient of deformation is defined as

$$F = \begin{bmatrix} \lambda & 0 & 0 \\ 0 & \lambda^{-1/2} & 0 \\ 0 & 0 & \lambda^{-1/2} \end{bmatrix} \tag{2.4}$$

with the right $\underset{\sim}{C}$ and left $\underset{\sim}{b}$ Cauchy-Green tensors,

$$\underset{\sim}{C} = F^T F = \begin{bmatrix} \lambda^2 & 0 & 0 \\ 0 & \lambda^{-1} & 0 \\ 0 & 0 & \lambda^{-1} \end{bmatrix}, \quad \underset{\sim}{b} = FF^T = \begin{bmatrix} \lambda^2 & 0 & 0 \\ 0 & \lambda^{-1} & 0 \\ 0 & 0 & \lambda^{-1} \end{bmatrix}, \quad \underset{\sim}{C} = \underset{\sim}{b} \tag{2.5}$$

The invariants (2.2) can be now be defined from the right (deformation) or left (spatial) Cauchy-Green tensors

$$\begin{aligned} I_1 &= tr(\underset{\sim}{C}) = tr(\underset{\sim}{b}), \\ I_2 &= \frac{1}{2}((tr(\underset{\sim}{C}))^2 - tr(\underset{\sim}{C})^2) = \frac{1}{2}((tr(\underset{\sim}{b}))^2 - tr(\underset{\sim}{b})^2), \\ I_3 &= det(\underset{\sim}{C}) = det(\underset{\sim}{b}) \end{aligned} \tag{2.6}$$

In Section 2.3, we use a numerical approach to simulate the behavior of soft actuators with the strain-energy function of different hyperelastic models.

2.2 Soft Actuator Design Parameters and Fabrication Processes

Many types of actuation mechanisms can be applied in soft robots [64]. The most well-known and widely used soft actuator is the pneumatic artificial muscle (PAM) developed by J. L. McKibben in the 1950s [65]. These artificial muscles consist of an inflatable bladder inside a braided mesh. The actuator can produce axial contraction and radial expansion movement when pressurized by air gas (Figure 2.2). In present days, this technology is commercialized by many companies which provide fluidic muscles in different configurations and dimensions for applications that can closely emulate biological movements.

(a)

(b)

Figure 2.2: Custom-built pneumatic artificial muscles (PAM). (a) Fabricated PAMs with different dimensions and materials for linear motion, and (b) elongation testing using weight plates.

In our work, we have mostly explored the fabrication of soft pneumatic bending actuators consisting of fluidic channels in an elastomer (Figure 2.3). When filled with pressurized fluid, the channels expand, causing the soft actuator to bend towards a strain-limiting layer. The inflatable structure is made from rubber or elastomer (Table A2), while the material used for the inextensible layer can be paper, fabric, plastic film or another elastomer with higher durometer.

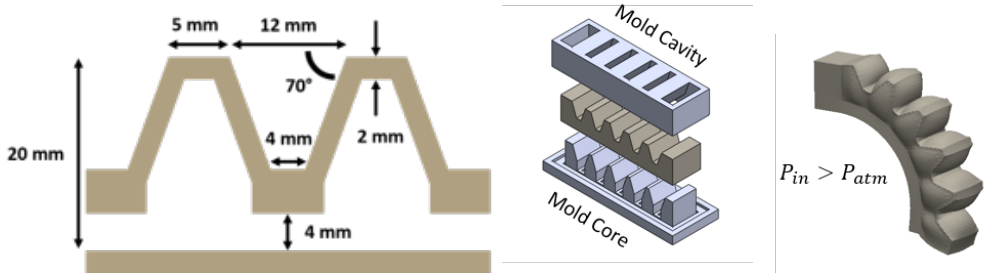

(a) (b) (c)

Figure 2.3: Design approach for the soft actuator and mold parts. (a) Cross-section of the SPA with representative dimensions; (b) core and cavity sides of the 3D-printed mold; (c) inflation state of the SPA.

Similarly, there are different fabrication processes available for creating compliant robotic components such as soft lithography (casting) [66], 3D-printing [67], and photopatterning [68]. A soft lithography process can be divided into three main steps: material preparation, vacuum degassing, and curing. The specific shape of the actuator is achieved through the design of cavity and core parts of a mold. In a specific study [69], we designed a mold using a CAD software (SolidWorks, Dassault Systemes) with a square cross-section of 25 $\times$ 20 mm and length of 100 mm. As shown in Figure 2.3a, the SPA design included topographical features, a similar concept as in [70], and with 70° angle to allow higher bending. The mold was made of polylactic acid (PLA) thermoplastic and fabricated with a 3D printer (MakerBot Replicator, MakerBot Industries). In addition, we designed a 2-part mold with molded-in assembly features to facilitate the removal of the soft actuator after the curing process (Figure 2.3b). We first mixed a two-part liquid silicone rubber (Dragon Skin 30, Smooth-On) and filled the mold with the uncured material. The silicone mixture was then degassed in a vacuum chamber at -95 kPa and allowed to cure for 16 hours at the room temperature. The curing time can be shortened by heating up the poured solution over a hot plate or inside a lab oven in compatible temperature ranges. Once the curing process was completed, the soft actuator was removed from the mold and a thin layer of silicone was bonded to the SPA bottom surface for covering the hollow chambers and enabling fluidic actuation. In order to supply compressed air to the soft actuator chambers (see Figure 2.3c), a silicone-based tubing with similar

durometer was inserted through the bottom layer of the actuator structure. The fabricated device is shown in Figure 2.4.

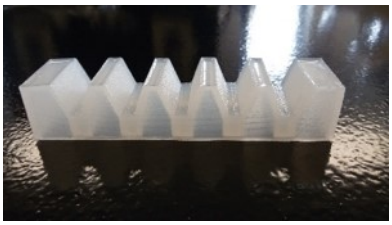

Figure 2.4: The fabricated SPA made of silicone rubber.

2.3 Soft Actuator Simulation

Simulation of soft actuators and flexible sensors is an important process in the study of soft robotic systems, in order to analyze their mechanical behavior, frequency response and design performance. An analytical model can provide some insights into the response of soft components to external forces for a given geometry. However, it cannot capture the interactions of internal elements with different materials. Finite Element Method (FEM) models provide the nonlinear response of the system as well as visualization of the soft component deformation and global performance in multiple configurations. We have simulated several soft bending actuator prototypes, using a finite element analysis software (Abaqus/CAE, Dassault Systemes). The geometries of the soft actuator and the sensor substrate were designed as solid bodies and meshed using solid tetrahedral quadratic hybrid elements (C3D10H element type), with 48,253 nodes and 30,144 elements. The Dragon Skin 30 and PDMS materials were modeled as an incompressible Yeoh material (μ = 2.38 kPa) [71] and incompressible Neo-Hookean material (μ = 1.84 MPa) [72], respectively. As shown in Figure 2.5a, the simulated soft bending actuator achieved a quarter bending when a pressure of 40 kPa was applied to its inner chamber. The uniaxial strains values at nodes 4455, 4365 and 4275 were measured from the SPA bottom surface in the converged solution (Figure 2.5b).

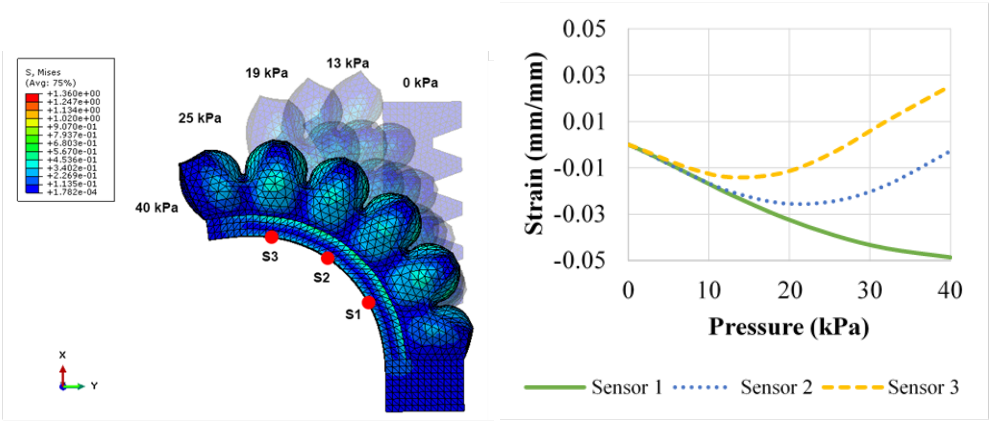

(a) (b)

Figure 2.5: Finite element simulation of the SPA. (a) Contour plot of the SPA FEM model (DragonSkin/PDMS), and its sequential deformation as pressure increases. (b) Graph of the strain values at each node corresponding to a potential sensor location (S_1, S_2, and S_3 in (a)).

2.4 Pneumatic System Hardware and Control Software

In general, fluid-driven actuators for soft robots can be powered by compressed atmospheric air [73], hydraulic systems [74], combustion [75], microfluidic logic [76], and through phase changing of low boiling point fluids [77]. There are many pneumatic energy sources available to power soft robots, and some important aspects should be considered such as selecting the appropriate compressor configuration (single, parallel, series) and matching the soft robotic project specifications (energy density, heat, pressure/flow rate) [78].

A custom-built pneumatic platform has been fabricated based on an open-source design available from the Soft Robotics Toolkit [79]. This platform allows the control of up to 4 independent pressure channels for a wide range of soft robotic applications (Figure 2.6). The control board has as its pressure source a 28 psi dual head miniature compressor (BTC-IIS, Parker Hannifin) with both positive and negative pressure (vacuum) operation modes. All channels are activated by a group of 3-way solenoid valves (VQ110U-6M, SMC), receiving amplified control signals from transistors that are connected to a microcontroller (Mega 2560, Arduino). In order to allow pressure feedback control, pressure gauge sensors (ASDXAVX100PGAA5, Honeywell) with analog

measurement capabilities are attached to each channel output.

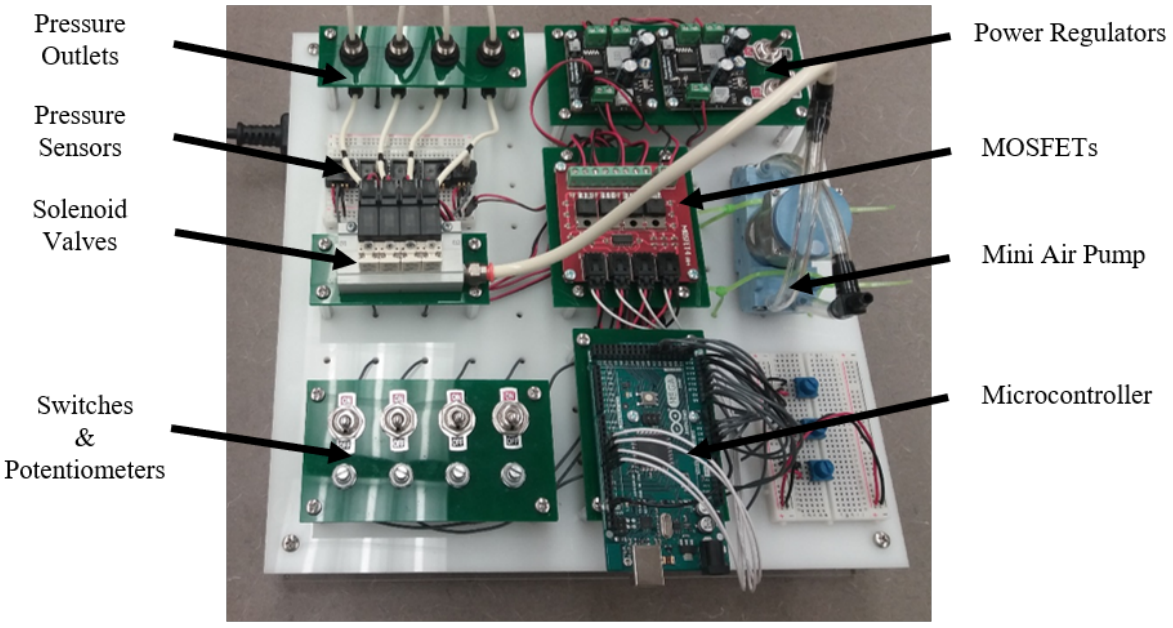

Figure 2.6: A control platform for fluidic soft robotic components. The mini air compressor is the energy source for fluidic soft actuators.

Using this hardware framework, different control strategies can be implemented via software. A commonly applied method for controlling the output pressure in a pneumatic system uses PWM signals. The PWM duty cycle percentage in combination with its wave frequency, can generate open/close commands to the solenoid valves, thus affecting the outlet pressure value at a certain time. Although a manual approach can be achieved for selecting output values by using switchers/potentiometers, an autonomous robot requires automatic computation of its desired output in response to its current input values. Therefore, a proportional-integral-derivative (PID) controller is designed to minimize the error of the pressure output (PWM duty cycle) at a given outlet based on a desired setpoint in both static (constant pressure) and dynamic (cyclic wave, trajectory) conditions. A PID controller is defined as

$$u(t) = K_p e(t) + K_i \int e(t)dt + K_d \frac{de}{dt}, \qquad e(t) = r(t) - y(t) \tag{2.7}$$

with K_p, K_i, K_d, being the controller gains for tuning and $r(t)$, $y(t)$, $e(t)$ being the setpoint value, actual output, and tracking error, respectively.

Multiple control programs were developed using different programming languages, each for a particular application and compatibility with additional components. A LabVIEW virtual instrument (VI) was created for easy interaction between the experimenter and the pneumatic platform due to its user-friendly interface (Figure 2.7). Besides being able to select a manual or automatic control mode, the program can also plot real-time data as well as save reports about collected measurements. In this method, the microcontroller behaves as a data acquisition board (serial communication) and all higher-level computation processes are performed by the computer. As an alternative, the control scheme was also encoded on a single executable file, C++, and as a script, Python, for compatibility with Linux-based systems. However, all user interactions are instead performed through a terminal window (command line). The main advantages of the aforementioned methods are the high-speed computation for a multiple-input multiple-output (MIMO) system and the communication across many devices such as cameras (image tracking), allowed by current computer architectures. Some drawbacks are the communication delay and potential network noises (USB, Bluetooth, Wi-Fi), along with parallel processing of competing services. In addition, an embedded version of the control software was developed for low cost prototyping boards. This allows an increase in sensor sampling rate and data processing since a cross-communication between two computer architectures is eliminated (firmware and software), and internal microcontroller registers can be manipulated directly. Different filtering techniques were implemented via software due to the pressure sensor sensitivity and potential environment noise. One approach was to use a first-order low-pass filter, which has the transfer function

$$H(s) = \frac{\omega}{s + \omega} \tag{2.8}$$

with $\omega = 2\pi f_c$, and f_c as the cut-off frequency. For processing signals in the sampled time domain, the low-pass filter can be discretized as

$$y(k) = y(k-1)e^{-aT} + x(k-1)(1 - e^{-aT}) \tag{2.9}$$

where a is the coefficient representing the cut-off frequency in the sampled time domain (radians per second) and T is the sampling time of the original signal (seconds).

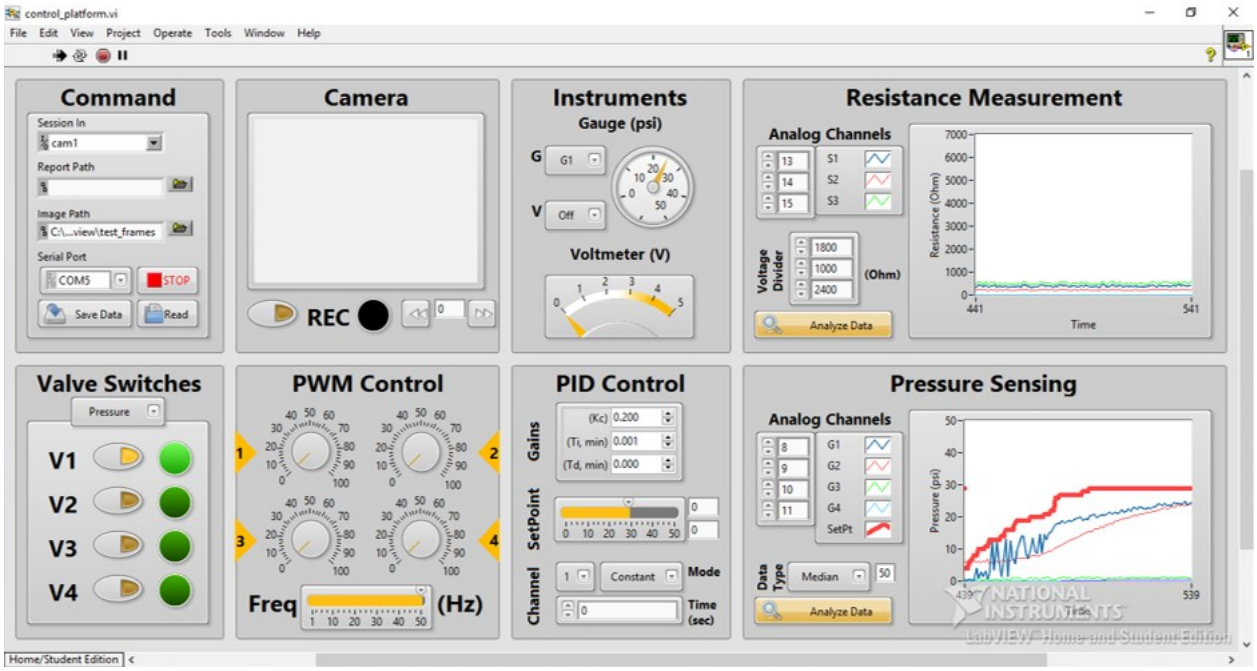

Figure 2.7: Control software with user interface developed in LabVIEW. The software allows manual and automatic control of all output pressures in the pneumatic board for static or continuous setpoint values.

2.5 Soft Actuator Stiffness Modulation

A great challenge in the soft robotics research area is the variability and controllability of the deformability and compliance of soft robots. Several stiffening approaches are found in the literature,

such as the use of active actuators arranged in an antagonistic manner and the use of semiactive actuators that can change their elastic properties [80]. In particular, electrically conductive materials with stiffness changing properties [81] can also be embedded in soft robotic devices to allow rigidity modulation in specific scenarios where relatively high forces and fixed posture are required. In [82], a collaborative work with Mohammed Al-Rubaiai, allowed the investigation of integrating 3D-printable conductive polylactic acid (CPLA) material with the SPA structure, using it as an inextensible layer as well as to actively modulate the soft actuator stiffness at desired locations. This study has been divided in two parts: (1) characterization of the thermomechanical properties and FEM simulation of the CPLA material; and (2) fabrication, integration, and experimental validation of SPA-CPLA devices. My contributions are related to the second part of this work. As shown in Figure 2.8, additional soft actuator designs are developed with 3D-printed resin-based molds (Form 2, Formlabs). A thin layer of silicone is applied to the SPA bottom surface and cured for covering the hollow chambers and enabling fluidic actuation. In order to modulate the stiffness of the SPA, a flat sheet made of CPLA (CDP11705, Proto-pasta) is integrated with the device. Local indentations are designed in the flat sheet geometry to facilitate bending at the hinge locations. Since the material is supplied as a filament, a fused deposition modeling (FDM) 3D printer (QIDITECH I, QIDI Technology) is used to fabricate the conductive sheet.

Thin copper wires are soldered to each hinge using silver paste (Silver Conductive Wire Glue, Amazon), without affecting the device flexibility. The CPLA sheet is encapsulated through a silicone rubber bath to allow adhesion with the SPA. A single rectangular (20 mm $\times$ 140 mm) silicone sheet (2 mm thickness) is placed inside a glass container with the CPLA sheet laying on top. The silicone mixture is poured inside the container up to a margin of 2 mm above the CPLA sheet. The SPA and encapsulated CPLA are bonded together using uncured silicone. In order to prevent slippage during grasping experiments, an additional anti-slip feature enabled with surface texture is included in the design of the SPA-CPLA. This component is molded with the same silicone material as the SPA. Figure 2.9 shows the picture of a fabricated prototype. The dimensions of all parts in the actuator are listed in Table A3.

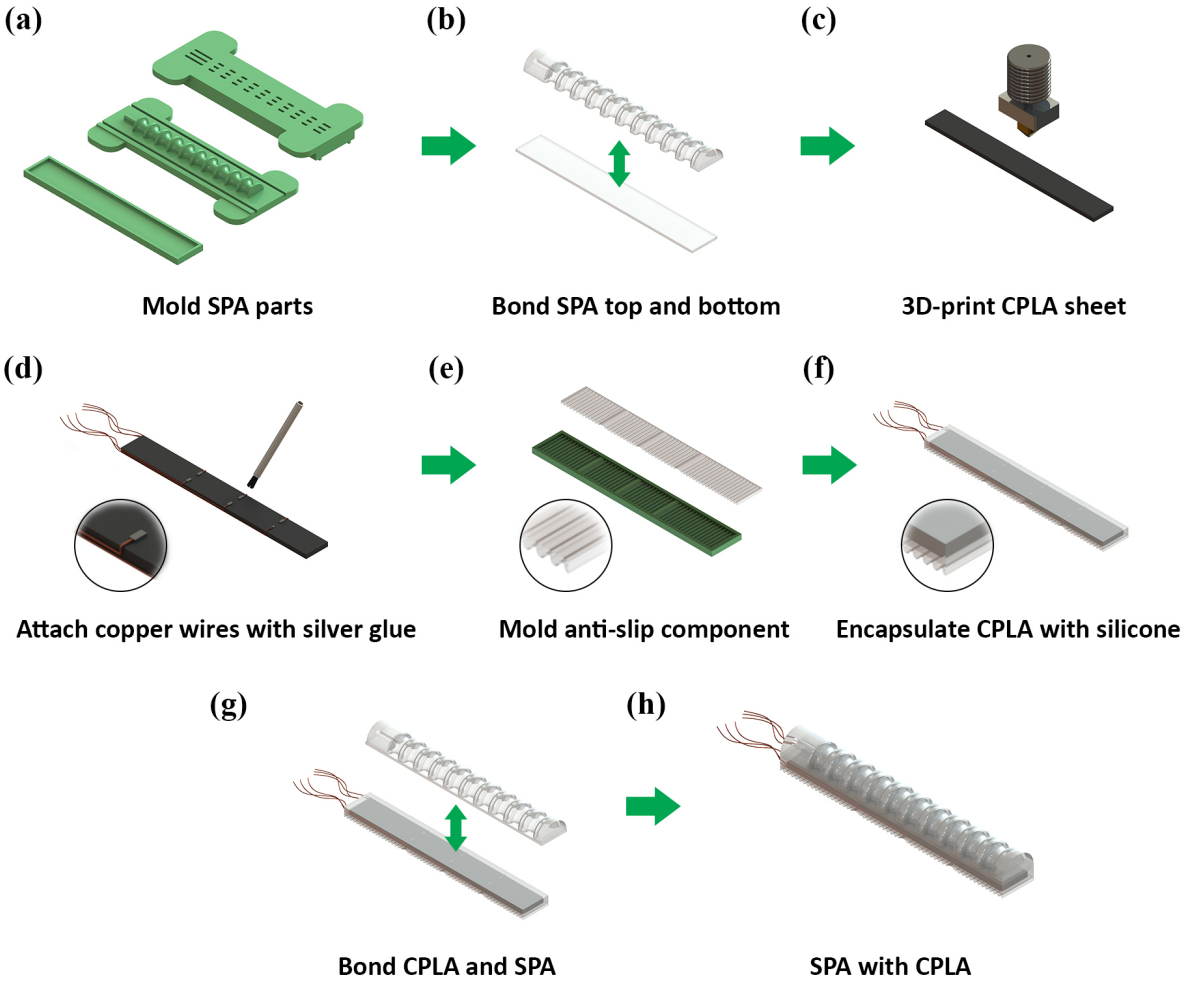

Figure 2.8: Fabrication of the SPA with a CPLA sheet integrated to its bottom layer. (a) 3D-printed mold parts forfabricating the SPA components; (b) Following curing, the upper and bottom parts of the SPA are bonded together; (c) The CPLA is 3D-printed using a FDM 3D-printer; (d) Thin copper wires are glued to the CPLA using a silver paste; (e) An anti-slip feature to prevent slippage during grasping; (f) The CPLA is encapsulated with uncured silicone; (g) The SPA and the encapsulated CPLA are bonded to complete the fabrication; (h) The final SPA-CPLA device after curing time.

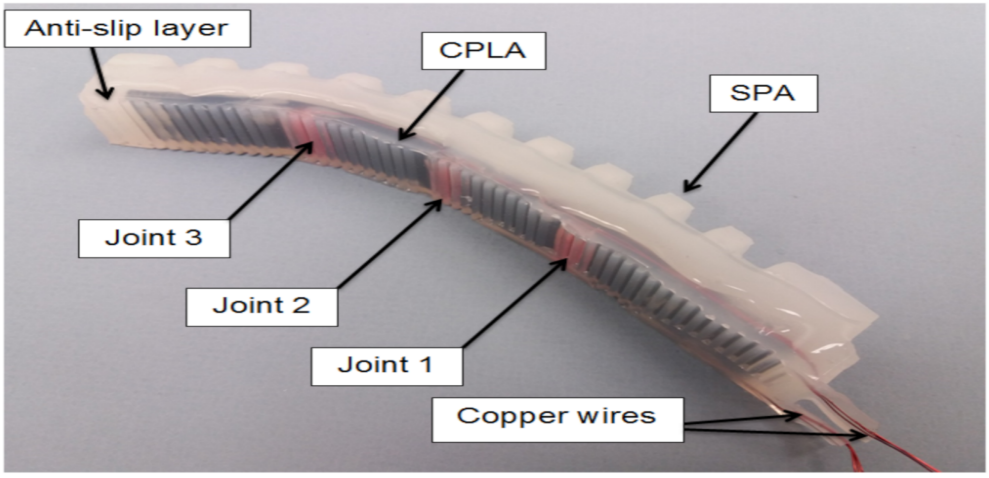

Figure 2.9: A fabricated soft pneumatic actuator (SPA) prototype with an embedded CPLA layer.

Additional experiments have been conducted to test the CPLA-embedded SPAs in a two-finger gripper configuration. The stiffness modulation in each finger can be controlled independently, allowing the generation of different bending angles to suit the shape of the object being manipulated. Multiple objects with various shapes and hardness are tested, where different grasping modes (e.g., scooping, pinching, grabbing.) are executed. In Figure 2.10 (a), (b), and (c), the soft gripper is holding a plastic container using the aforementioned modes, while in Figure 2.10 (d) and (e), a soft mini football and a plastic cup filled with candies are lifted with a constant pressure of 20 psi. Note that in these trials, CPLA enables local shape reconfiguration of the actuators for the execution of different grasping modes.

(a) (b) (c) (d) (e)

Figure 2.10: Grasping of multiple objects using different grasping modes. A plastic container was grasped using (a) scooping, (b) pinching, and (c) parallel grabbing. Additional tests were conducted for grasping (d) a plushy mini football, and (e) a cup filled with candies.

In order to evaluate the payload capacity of the SPA integrated with CPLA, several weights are placed inside a plastic container, which is held by a single finger. The masses range from 50 g to 500 g (Figure 2.11), and the total carried weight is increased in increments of 50 g. The tests are performed for a minimum of 50 g and a maximum of 800 g. Two different SPA states are considered for evaluating the finger strength: pressurized and unpressurized. For the pressurized case, a constant pressure of 22 psi is applied to the SPA inner chambers, and all hinges are active (12 V input) throughout the entire experiment. On the other hand, for the unpressurized case, the SPA is initially supplied with 24 psi pressure, while having all hinges activated, and then the positive pressure is removed (slow decrease down to atmospheric pressure) after the voltage input is turned off and the CPLA layer is completely cooled to room temperature. As shown in Figure 19, for both states, the soft finger is able to withstand the maximum payload of 800 g without causing any device failure or dropping the weights. The ability to hold shape and carry weight without pressure and electrical inputs (and thus no power consumption) is particularly significant for applications that involve holding given postures for long periods of time.

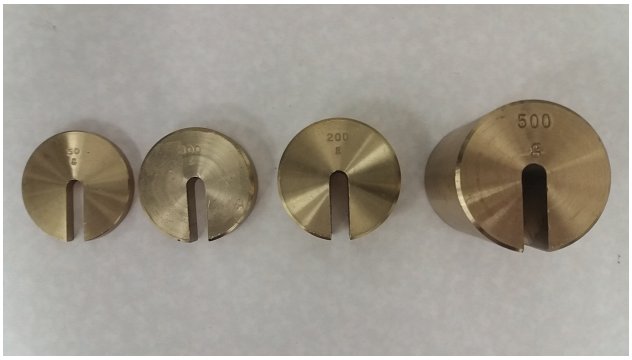

Figure 2.11: Metallic weights (50 g - 500 g) used during the single-finger holding experiment.

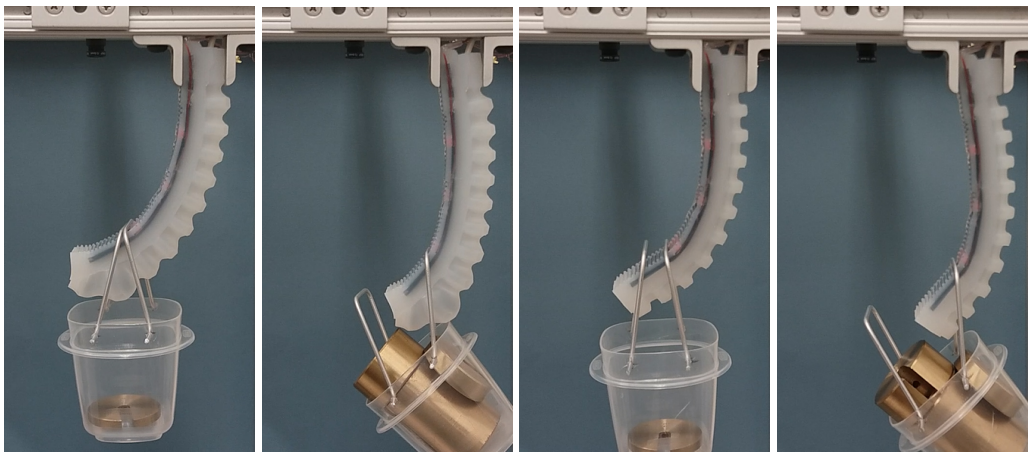

(a) (b) (c) (d)

Figure 2.12: Testing load capacity of the SPA integrated with CPLA. A single-finger SPA-CPLA holding (a) a minimum weight of 50 g, and (b) a maximum of 800 g at 22 psi (inner chambers) and 12 V input at all hinges. Load-carrying tests without pressure input (and hinge voltage inputs off): (c) under a load of 50 g without pressure and electrical inputs, (d) under a load of 800 g without pressure and electrical inputs.

Chapter 3

Fabrication, Characterization and Integration of CNT-based Flexible Sensors

3.1 Screen-Printing-based Sensor Fabrication

As the first step towards proprioceptive feedback in SPAs, we investigated new methods for achieving flexible sensors that can detect strains along a soft actuator bottom layer [69]. In Figure 3.1, we demonstrate how a CNT-based sensor array can be fabricated through simple steps. This design allows the creation of customizable flexible sensors without geometric constraints.

An array of CNT-based strain gauges was fabricated using a screen-printing process. A polyimide film (Kapton, DuPont) was used for designing the pattern of the sensor array and circuit traces. In the first mask, we cut three equally spaced rectangles (10 $\times$ 2 mm) corresponding to the areas for the distributed sensor array along the device structure. A second mask was created to assist in the application of the trace material, with each sensor connected to two traces on its ends. The material used for the sensor substrate was polydimethylsiloxane (PDMS) (Sylgard184, Dow Corning) with a 10:1 base and agent mix ratio. The substrate ($\approx$2 mm thickness) was fabricated using two heat-resistant borosilicate glass sheets (150 $\times$ 150 mm) clamped together and heated over a hotplate for 10 min at 150 °C. A polyester film was adhered to the inner surface of each

glass sheet to help in the removal of the PDMS substrate without causing any tear or wrinkles. The size and shape of the spacer material directly affect the substrate uniformity. In this procedure, we have used microscope slides with identical width and length to separate the glass sheets at opposite edges. After fabrication, the substrate was cut in a rectangular shape (120 $\times$ 25 mm) and treated with electric discharge to convert it to a less hydrophobic surface (wetting). The substrate and the first mask were attached together to allow the application of the sensor material (Figure 3.1a). A single walled CNT (SWCNT) conductive ink, 1 mg/mL CNTs (VC101, Chasm Technologies), was applied over the polyimide film (Figure 3.1b), allowing the deposition of the SWCNTs on the PDMS substrate only through the small cuts. Small variations on ink dispersion can cause deviation in sensing characteristics. A spatula was used to level the CNT paste even with the polyimide film to obtain an ideal dispersion at each sensor location. The substrate was once again heated (60 °C) in order to ensure adhesion between both materials. Once dried, the second mask was attached to the substrate (Figure 3.1c). AgNWs in water (AgNwL50H2O, ACS Material), with 50 nm of diameter and 200 um of length, was applied through the open cuts using a pipette (see Figure 3.1d). The traces were dried at 60 °C for 1 h. As shown in Figure 3.1e, thin copper wires were attached to the endpoints of each trace by fixing them with a silver paste, 60% Ag (PELCO Colloidal Silver, Ted Pella). A second layer of uncured PDMS was applied to the top face of the sensor array to encapsulate the device (Figure 3.1f).

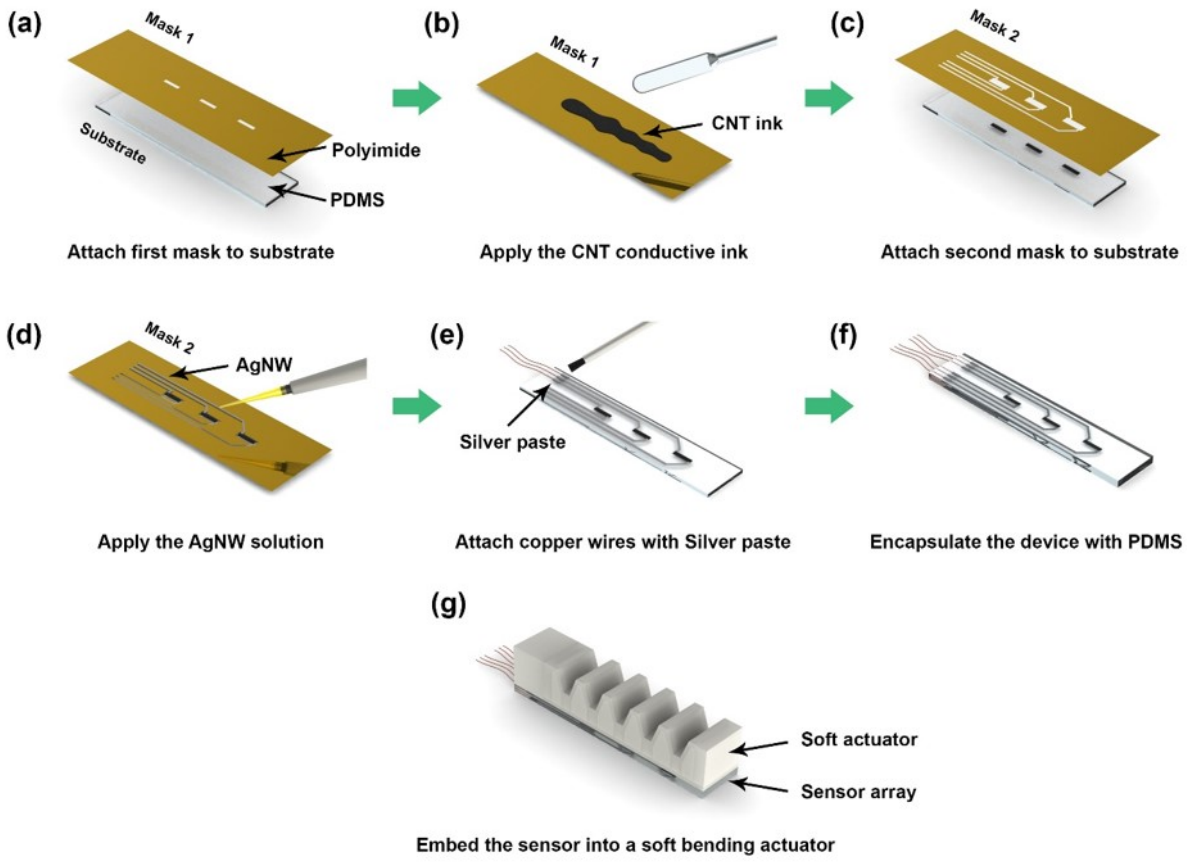

Figure 3.1: Fabrication steps of the flexible CNT-based sensor array: (a) the sensor mask is attached to the polymeric substrate; (b) the CNT conductive ink is applied over the mask surface to create the distributed strain sensors; (c) the trace mask is attached to the substrate; (d) AgNW solution is applied through the mask gaps using a pipette; (e) thin copper wires are attached to the endpoint of each trace with a silver paste; (f) encapsulation of the device with PDMS; (g) and bonding of SPA and sensor array with uncured silicone.

As an example, the sensor array was fabricated with three strain gauges which are referred to as S_1, S_2, and S_3, in this work, with S_1, being closest to the air inlet, and S_3, being close to the distal end of the actuator. The flexible sensor array was characterized and bonded to the bottom surface of the soft actuator using uncured PDMS (Figure 3.1g). The fabricated devices are shown in Figure 3.2.

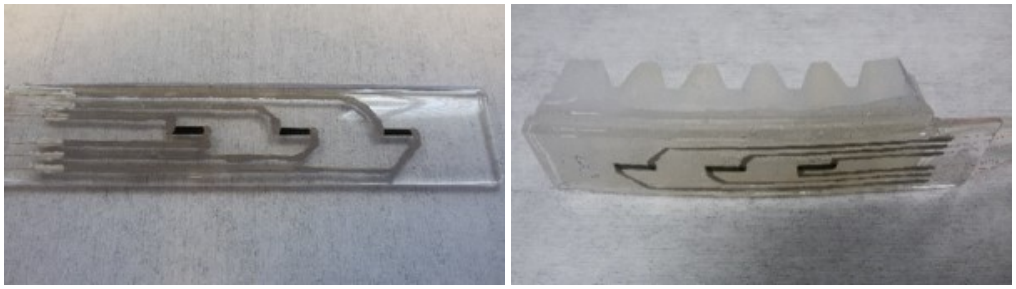

(a) (b)

Figure 3.2: The fabricated CNT-based sensor array. (a) Sensor array device, and (b) a SPA with integrated sensors.

3.2 Sensor Array Measurement and Characterization

The CNT conductive ink has a mesh-like nanostructure which can change its electronic characteristics when subjected to extension or compression. When there is a voltage between both ends of an individual CNT-based sensor, the latter behaves as a variable resistor that changes its resistance value during mechanical deformation. A voltage divider circuit can be used to measure the voltage across the flexible strain gauge sensor and thus its resistance value. By using Ohm's Law, we have:

$$V_s = I_s \times R_s \tag{3.1}$$

$$I_s = \frac{V_i}{R_{ref} + R_s} \tag{3.2}$$

where V_i, V_s are the input voltage and the voltage across the sensor, respectively, I_s is the current going through the sensor, and R_s and R_{ref} are the sensor resistance and the reference resistance, respectively. By combining (3.1) and (3.2), we can get,

$$R_s = \frac{R_{ref}}{V_i/V_s - 1} \tag{3.3}$$

The resistance R_{ref} is selected based on the minimum and maximum resistance values obtained

from each individual sensor (denoted as $R_{s,min}$ and $R_{s,max}$, respectively). This relation can be expressed as:

$$R_{ref} \approx \sqrt{R_{s,min} \times R_{s,max}} \tag{3.4}$$

In order to associate the change in resistance with the amount of strain applied at a sensor position, multiple measurements of the resistance are recorded as the substrate is subjected to different values of strain. The axial strain formula is given by:

$$\varepsilon = \frac{\Delta L_s}{L_{so}} = \frac{L_s - L_{so}}{L_{so}} \tag{3.5}$$

where L_{so} and L_s are the nominal (untensioned) length and the current length of the sensor array, respectively.

The fabricated CNT-based sensor array was placed on a programmable stretching device with both ends clamped (80 mm active length). A loading cycle of ≈10 s (stretch and release) was performed for 60 min for the initial conditioning step of the device (Figure 3.3). The sensor array was subjected to a stretch of 5% (L_s = 84 mm). This is an important process for stabilizing the microscale structural change of the nanomaterials. The conditioning phase was performed until the device achieved rersible and stable electrical signals for a desired range of strain. Although the sensor array had reached its stability margin after 60 min, the stretching cycle was run up to ≈180 min to ensure measurement repeatability. A data acquisition equipment was used in combination with an integrated dataflow software (LabVIEW, National Instruments) for collecting the change in resistance of each strain sensor.

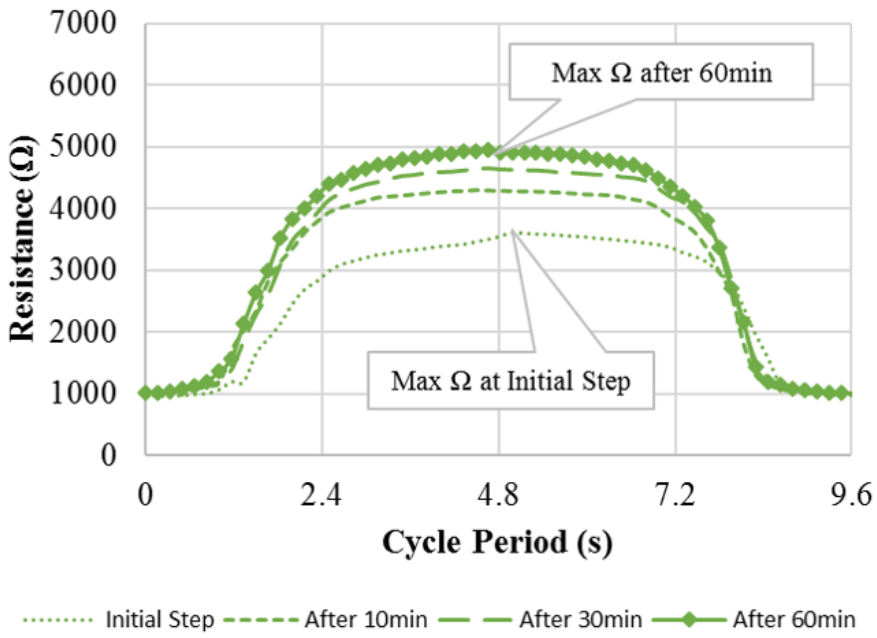

Figure 3.3: Continuous measurement of the resistance change in S_1 during conditioning phase. The depicted lines show the difference in the maximum range of the sensor at initial step and after three time frames: 10, 30, and 60 min of loading cycle.

After the conditioning step, each individual sensor was measured in a sequence. In Figure 3.4, we show a short sample of the collected data from sensors S_1 to S_3 after 96 min of stretching. Each strain gauge experienced different ranges of resistance change since the concentration of the CNT material and the thickness along the substrate can directly affect their measurement range. The sensors fabricated in this work were tested only for stretches below 10%. A larger strain value could increase the number of cracks in the sensors, causing malfunction and unreliable measurements. Other design options that alleviate mechanical stress such as a horseshoe-shape would allow sensor functionality for larger stretches.

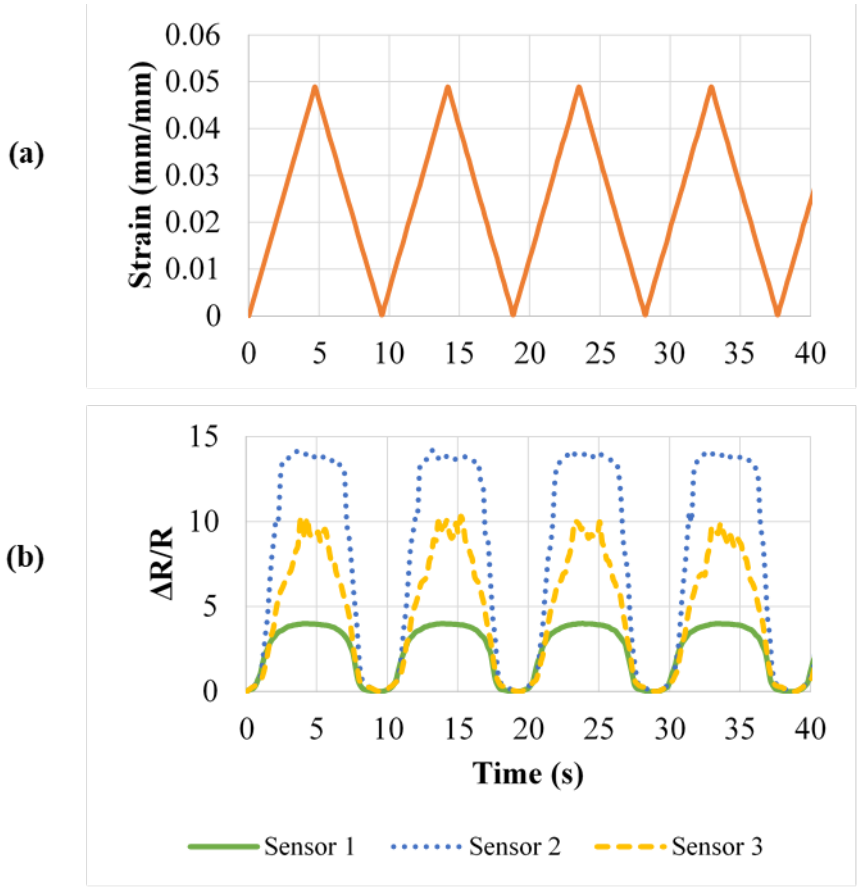

Figure 3.4: Sensor array measurements after initial conditioning: (a) the amount of strain applied in the continuous stretch and release test, (b) and the relative change in resistance ($\Delta R/R$) for sensors S_1, S_2, and S_3.

Based on the data collected from the stretching process, we obtained the resistance-strain relation (gauge factor) for each individual CNT-based sensor (Figure 3.5). As is observed, all three sensors achieve a saturation level at a certain strain value. Since the CNT bundles change their arrangement when the substrate is under strain, the conductive path within the nanomaterial is modified. The change in each sensor's shape during stretching can also contribute to a saturated strain behavior. For small strain values, the gauge factor of each strain gauge is defined as:

$$GF = \frac{\Delta R/R}{\varepsilon} = \frac{\Delta R_s/R_{so}}{\Delta L_s/L_{so}} = \frac{\Delta R_s L_{so}}{R_{so}(L_s - L_{so})} \tag{3.6}$$

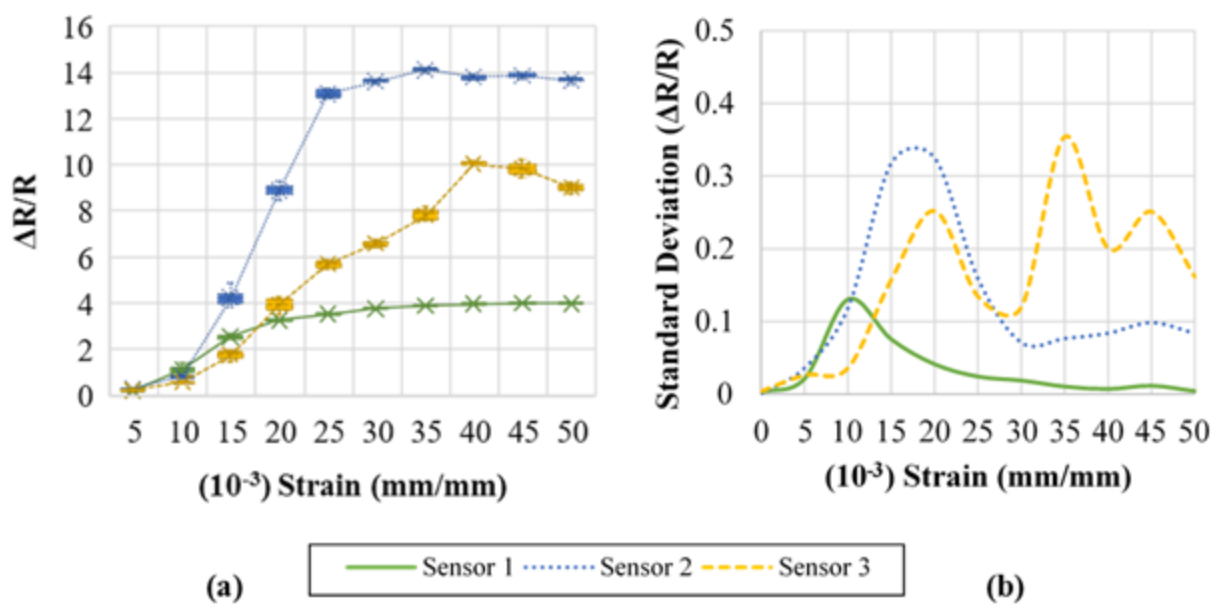

Figure 3.5: Gauge factor of each strain gauge. (a) Strain and $\Delta R/R$ relationship based on different sets of data (with mean lines) obtained through the cyclic stretching of the sensor array substrate, and (b) the standard deviation of $\Delta R/R$ from the measured samples.

3.3 Soft Actuator with Integrated Sensors Testing

The performance of the integrated soft actuator-sensor was evaluated in experiments. In this procedure, the sensor S_2 was not included since the process of embedding the sensor array substrate with the SPA caused a malfunction of this sensor. A pressure gauge sensor (ASDX Series, Honeywell) was used for detecting the inner pressure of the soft pneumatic actuator during the bending motion. The soft actuator inlet was connected to a 12VDC miniature air compressor (P_{max} = 28 psi) through a polyurethane tubing. During this test, we measured the resistance change of S_1 and S_3. When the sensor array was combined with the soft actuator, the minimum and maximum resistance values were changed due to the contribution of residual strain from the soft structure. By measuring Rs1 and Rs3 with a multimeter during the actuator inflation, we registered the new values as: $R_{s1,min} \approx 1.3$ kΩ and $R_{s1,max} \approx 2.7$ kΩ; $R_{s3,min}$ and 1.8 kΩ and $R_{s3,max} \approx 3.6$ kΩ. From (3.4), we obtained the value for the reference resistors as $R_{ref,s1} \approx 1.8$ kΩ, $R_{ref,s3} \approx 2.4$ kΩ,

and a series circuit was built using trim potentiometers.

The sensor outputs (pressure and strain gauges) were sent to a microcontroller (Mega 2560, Arduino), which was connected to a computer using USB interface for communication with the data acquisition software. All measurements were obtained with a sampling time of 25 ms, and a solenoid valve connected to an air pump was controlled using pulse-modulation width (PWM) at 50 Hz. As shown in Figure 3.6a, the fabricated soft actuator achieved 90° bending angle with an internal pressure of 60 kPa (≈8.7 psi), which is close to the FEM simulation results. The curvature of the soft actuator inner radius was captured with a digital camera, recording individual frames that correspond to a constant pressure value. The percentage of the PWM duty cycle was computed by a PID function within LabVIEW, with the process variable being the median of the pressure sensor output after thirty measurements. Various setpoints were tested with the control system, and the respective resistance values in each strain gauge were captured, as shown in Figure 3.6b.

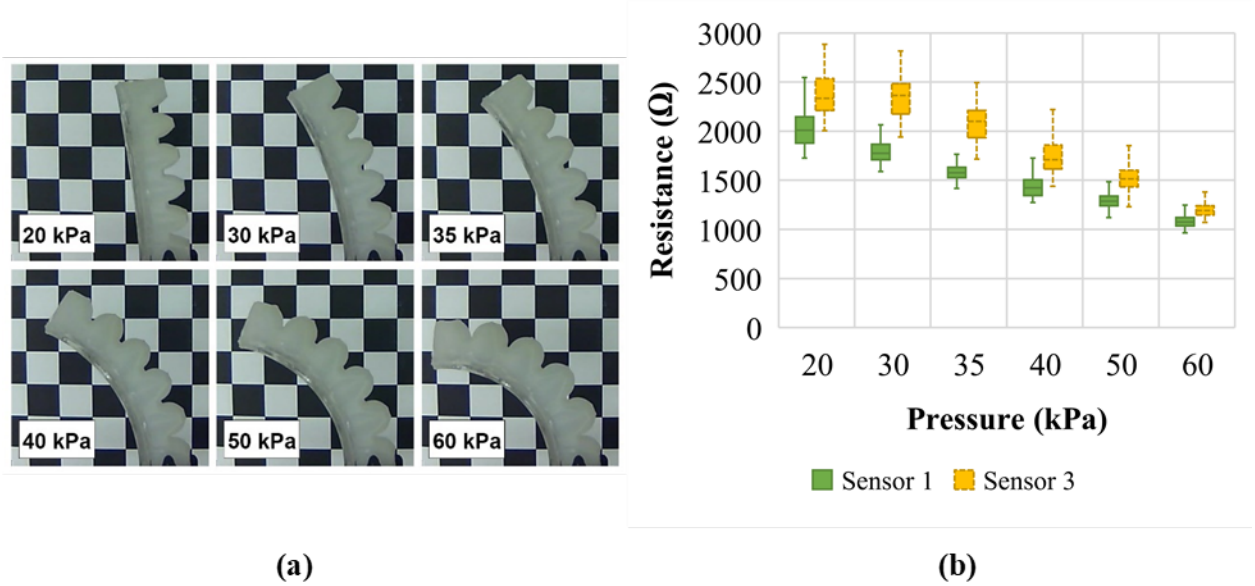

Figure 3.6: The sequence of images of the SPA with embedded CNT-based sensors, showing the curvature and sensor values at different applied pressures. (a) Captured images during activation of the SPA, and (b) the strain gauge array measurement at various constant pressure setpoints.

The SPA can be applied in several tasks such as reaching, grasping and touching. In order

to have an accurate estimation about the actuator position or curvature, the sensor array must be able to capture the deformation during motion. In Figure 3.7a, b, we show the measurements of the difference in the sensor output response (hysteresis) during inflation (loading) and deflation (unloading), with a range of pressure setpoints varying every 0.8 ms. The total operating time is 16 s, with the setpoint increasing from 0 to 60 kPa, and vice versa (Figure 3.7c).

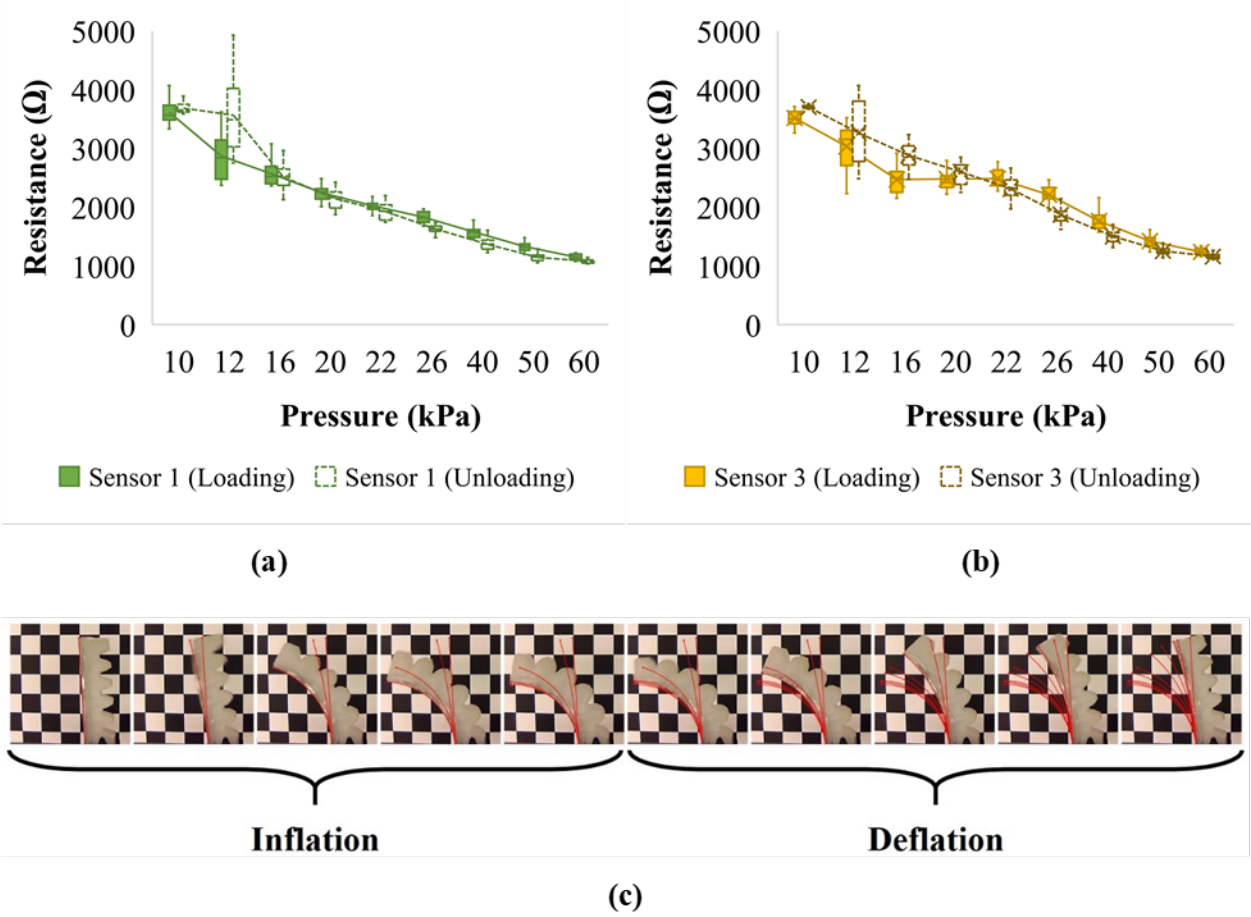

Figure 3.7: Pressure and resistance relationship for the fabricated SPA with embedded sensor array. The variation in resistance (with meanlines) for both inflation (loading) and deflation (unloading) steps are shown for sensors S_1 (a) and S_3 (b), when the pressure setpoint was varying from 0 to 60 kPa. (c) A sequence of frames showing the actuation steps and the curvature of the SPA.

With the gauge factor obtained during the sensor array characterization process, we estimated the amount of strain in the SPA at different curvatures. The actual curvature of the SPA was measured from the captured image frames during bending. An image processing software (Vision

Assistant, National Instruments) was used to measure the SPA inner radius of curvature for each pressure setpoint. The arc length of a specific bending shape was measured and inserted in (3.5) (with L_{so} = 100 mm) to find its correspondent axial strain value. In Figure 3.8, we compare both sensor and actual measurements when the curvature increases. These results agree with the compression observed in the bottom layer of the SPA during positive pressure.

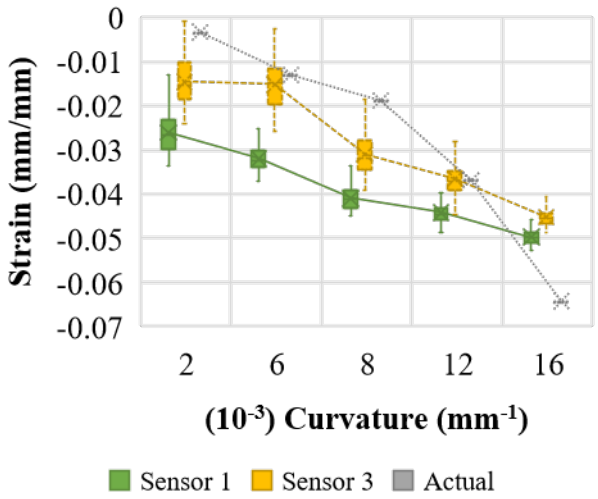

Figure 3.8: The relationship between strain and curvature of the SPA based on the range of resistance values captured by the sensor array. The actual value represents the measured curvature from the SPA inner radius.

By integrating multiple strain gauges along the soft actuator structure, the sensor array can provide angular measurement, contact detection or proprioceptive sensing for a soft robotic system. The distributed measurements allow estimation of the actuator deformation and the locations and forces of interactions between the actuator and foreign objects. Since the sensors are fabricated through screen printing process, customization can be applied according to the soft actuator geometry and strain directions of interest. In addition, the number of strain sensors and their position can be optimally chosen based on the regions which experience large deformations. The sensor array design presents some constraints regarding the number of sensors that can be fabricated in a single substrate. Since the trace width can affect the sensor reading, reducing its dimension to increase the amount of strain gauges can impact the reliability of the sensor measurement. In-

creasing the thickness of each trace may allow the design of thinner features, but this process was not investigated in this current work. The manual fabrication method applied in this work brings challenges for achieving a uniform substrate thickness and CNT ink dispersion. Automated mass production ultraviolet (UV) curing and screen-printing processes could reduce the uncertainties and issues identified in the investigated method.

Chapter 4

3D-Printing of Liquid Metal-Based Stretchable Conductors and Pressure Sensors

4.1 Microfluidic Structure Design and Fabrication

4.1.1 Conventional Fabrication Methods

Traditionally, microchannel structures for sensing devices are fabricated using labor-intensive and cumbersome methods. The literature in its majority has reported microchannel-based sensors by following fabrication techniques such as laser micromachining to create molds [83], vapor deposition of hydrophobic monolayers for easy demolding [84], spin coating of PDMS to create thin elastomer films [85], cross-linking of silicones through oven-curing [86], and oxygen plasma treatment to construct the microchannel cavities [87]. A liquid metal-based soft artificial skin was created using silicone casting over a 3D-printed mold [88]. Besides many additional fabrication steps, the silicone curing process took more than three hours. Curvature sensors with microchannels filled with EGaIn can be produced using a combination of photolithography and replica moldin [89]. However, the entire fabrication process including vapor deposition, silicone cross-linking, oxy-

gen plasma treatment, and elastomer film bonding is approximately four hours long. Furthermore, PDMS microchannel tiles in devices tailored to laser axotomy and long-term microelectrode arrays (MEA) can take more than two days for fabrication when using soft lithography procedures [90]. In addition, a broad range of approaches for the application of 3D printing technology to rapidly prototype microchannel structures have been explored, accelerating the research and development of microfluidic sensors and devices [91][92]. On the other hand, some rapid manufacturing techniques such as using polyethylene glycol (PEG) as a sacrificial layer through ink-jet printing required a 10-hour long curing process of the PDMS-based substrate [93]. Modified photocurable materials have also been explored for 3D-printing of soft pressure sensors, but a custom-built printing system is required to develop these devices [94]. These previously reported methods present some disadvantages and challenges such as time-consuming procedures, limited materials selection, removal of the sacrificial layer, and microchannel device replication. Consequently, there is a demand for new manufacturing techniques to address these issues.

4.1.2 Microchannel 3D-Printing

The fabrication of the microfluidic structure for the pressure sensing device was inspired based on the technique presented in [95]. This previous study conducted investigation on 3D-printing enclosed microfluidic channels without photocurable supports in rigid materials. The method utilizes a viscous liquid support instead, requiring minimal to no postprocessing to form sealed channels. In this work, we sought to improve this method by exploring it on soft substrates in order to achieve flexible and stretchable 3D-printable microchannel-based conductors and sensors. A PolyJet-based 3D-printer (J750, Stratasys) and a UV-cured resin with post-cured rubber-like properties (Agilus30, Stratasys) were used to create the microchannel cavities. This fabrication process followed a three-step procedure: 3D-printing of the bottom substrate containing open microchannel cavities, filling the microchannel cavities with liquid support material, followed by 3D-printing a top-substrate directly onto the bottom substrate to close the microchannels. These steps can be repeated several times depending on the number of microchannel or substrate layers.

Traditionally, 3D-printing of devices with enclosed hollow channels requires initially printing the channel so that it is filled with a sacrificial photocurable support material. This material is then manually removed in post-processing, a procedure that can take hours to days, and it is impossible to remove from small channels with complex geometries (spirals or serpentines). The method used here allows fabrication of channels without any photocurable support material. The 3D geometry design for the microfluidic soft substrate was separated in two parts: a bottom layer with the microchannel cavities, and a top flat layer with holes in each end of the microchannel for removing the liquid support material. This design process can be easily stacked, although we did not investigate sensor designs with these characteristics in this current work. First, the soft substrate bottom layer was 3D-printed over a transparency film (Premium Transparency, Xerox) to facilitate the final substrate removal from the 3D-printer bed. Next, once the bottom layer printing process was finalized, a liquid sacrificial layer, composed of glycerol (Glycerol 99.5%, Sigma-Aldrich) and isopropanol (2-Propanol 99.5%, Sigma-Aldrich) mixture (70:30 v:v), was manually dispersed over the microchannel cavities using an 1 ml plastic syringe. A small flexible spatula was used to distribute the mixture evenly throughout the exposed microchannels. In addition, during the liquid dispersion phase, the top layer printing process was already initialized, with the 3D-printer head performing automatic calibration outside the print bed for 30 seconds. This is an important process to avoid beading of the liquid support material between each layer, which could lead to clogging or irregular cavities. The entire printing process, including manual liquid dispersion, took approximately 6 minutes. This method was tested for fabricating up to 6 sensor substrates simultaneously.

As an initial investigation, we first created a 3D CAD model of a substrate with 2 mm overall thickness and multiple straight microchannels (SolidWorks, Dassault Systemes) to determine the minimum cavity cross-section height and width for 3D-printing microchannels into a soft material. We selected several dimensions based on reported results from literature regarding liquid conductor-based sensors [96][97]. The width of the straight microchannels had a range from 300 μm down to 100 μm, and a height range from 200 μm down to 100 μm. As shown in Figure

4.1, the smallest achievable microchannel had 150 μm $\times$ 150 μm cross-section, with applicable microfluidics in a soft substrate.

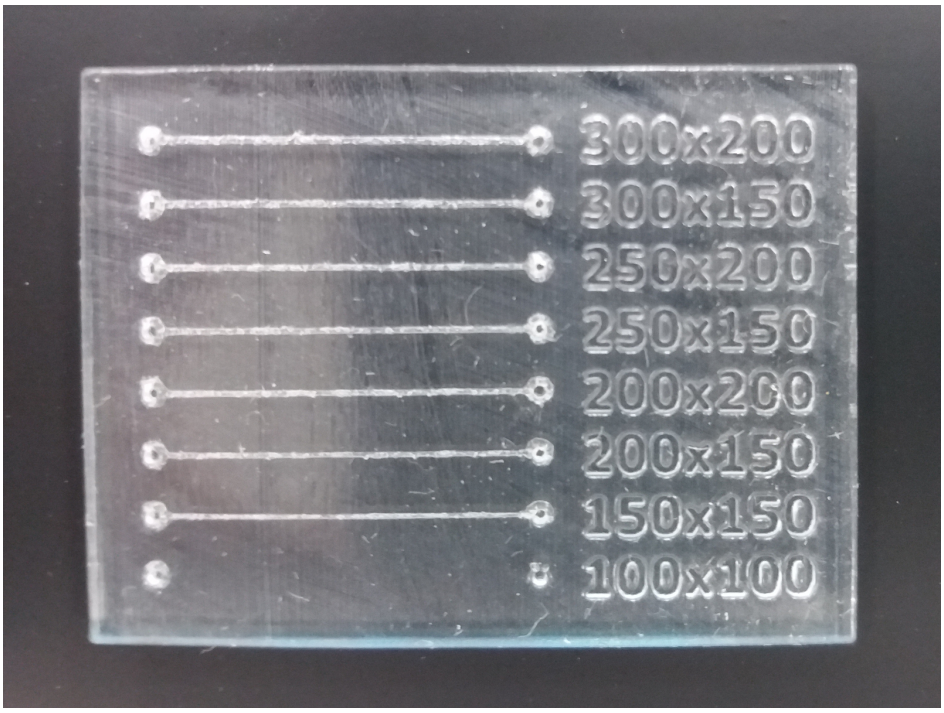

Figure 4.1: 3D-printed straight microchannels over a soft substrate (Agilus30) with 2 mm overall thickness. The minimum microchannel cross-section size identified was of 150 μm $\times$ 150 μm (height/width).

4.1.3 Pressure Sensor Design Parameters

A microfluidic pressure sensor was developed by designing spiral-shaped microchannels into a soft substrate. This makes the sensor suitable for pressure detection, since it will not respond to uniaxial stretches due to counter-balanced electrical resistance change in perpendicular directions [86]. Although it was found that the minimal microchannel size for the fabrication technique in this work is 150 μm $\times$ 150 μm, this dimension prevents the removal of the glycerol/IPA mixture from the inner cavities when designed as a spiral. We have identified that microchannel cross-section sizes higher than 350 μm $\times$ 350 μm are better suited for this type of sensor design (Figure 4.2).

The pressure sensor was designed with a 1.5 mm thickness substrate (30 mm $\times$ 25 mm rectangular shape), and the spiral microchannel was centered at the middle. The microchannel design

was comprised of a 3-turn spiral (inwards and outwards) and 1.3 mm spacing between channels, with a total sensor active area of 20 mm in diameter. A mix ratio of 70A durometer between Agilus30 and VeroClear materials was selected in order to balance the sensor compliance. Since the bottom layer and cavity structure all combined had a total height of 925 μm, a very thin upper layer (575 μm) enabled fast sensor production. The complete fabrication process is explained in Figure 4.3.

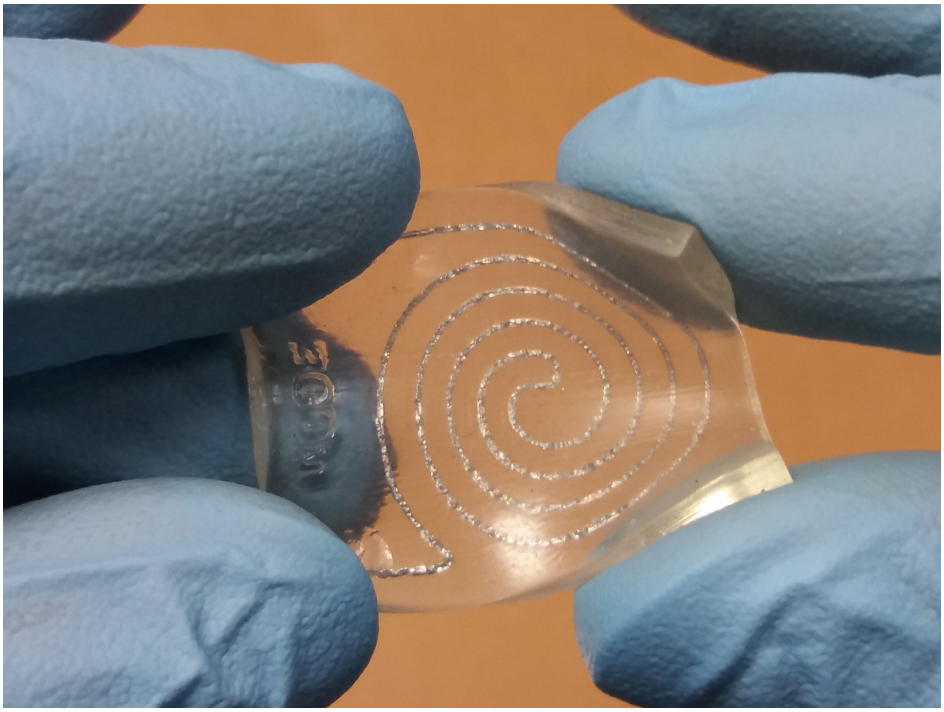

Figure 4.2: 3D-printed microfluidic spiral-shaped soft pressure sensor with embedded liquid metal (EGaIn).

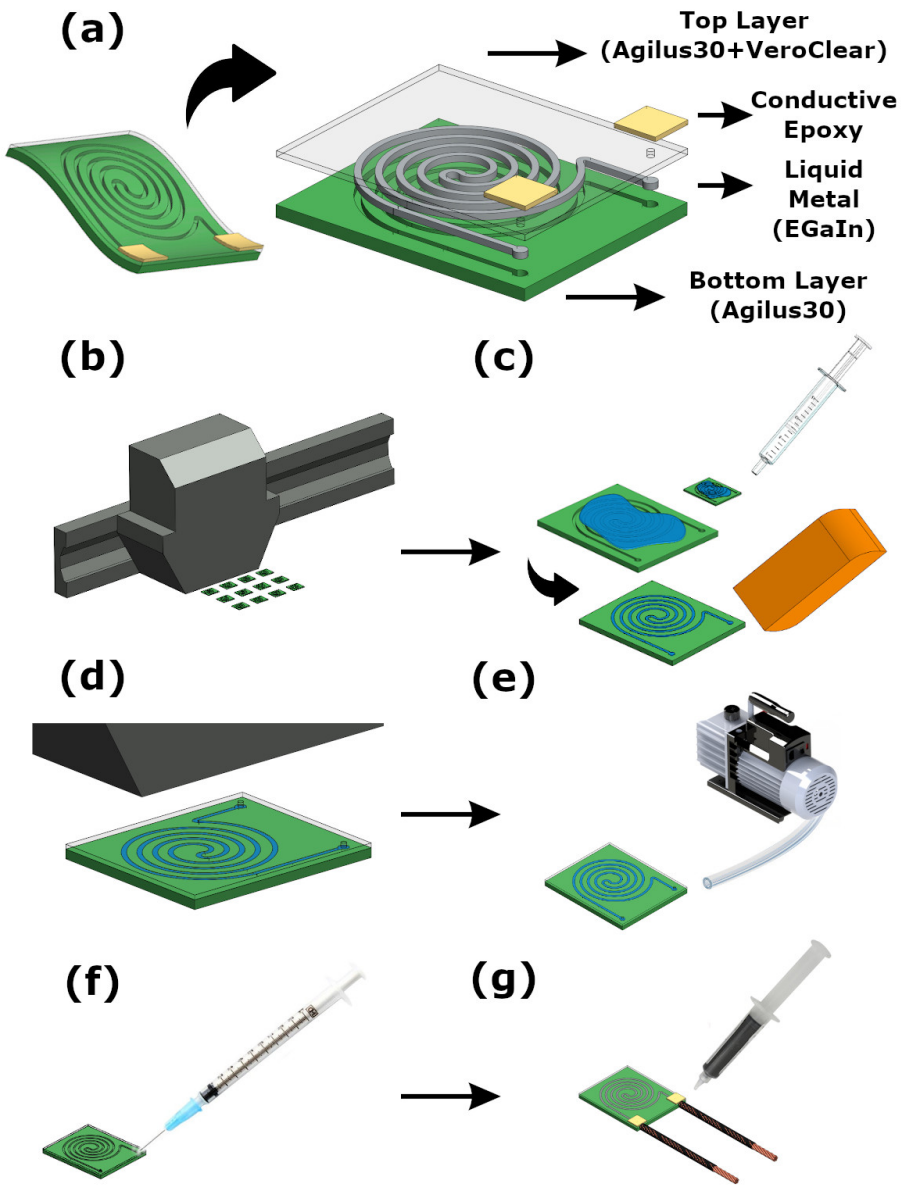

Figure 4.3: Design and fabrication steps of the 3D-printed pressure sensor embedded with LM. (a) The sensor components: a bottom layer made of pure Agilus30, a top layer made of Agilus30 and VeroClear mixture (70A Shore Hardness), a microchannel structure for filling with liquid metal (EGaIn), and two end terminals encapsulated with conductive epoxy; the fabrication steps were: (b) 3D-printing of the bottom layer with microchannel cavities of cross-section size 350×350 μm, (c) manual dispersion of the glycerol-IPA mixture, (d) 3D-printing of the top layer with outlets at each end, (e) vacuum-based removal of liquid sacrificial layer, (f) manual injection of EGaIn, and (g) encapsulation of both terminals and soldering of copper stranded wires with conductive epoxy.

4.1.4 Liquid Metal Embedding and Encapsulation

The microfluidic electronics in this study are fabricated using EGaIn, which has a high electrical conductivity ($\sigma = 3.4 \times 10^6$S m^{-1}), a resistivity of $\rho = 29.4 \times 10^{-8}\ \Omega$ m^{-1}, and low toxicity [98]. After completion of the 3D-printing process for the substrate, a small tubing connected to a vacuum pump was inserted into one of the microchannel ports to extract the glycerol mixture. The removal process only takes approximately 3 to 5 seconds for each device. Once all the liquid support was removed, a 1 mL syringe with 22 gauge needle (0.70 mm) was used to inject the liquid-phase alloy (EGaIn, Sigma-Aldrich), composed of $\geq$99.9% trace metal basis, inside the microchannel cavities (Figure 4.3f).

Uncured Agilus30 was initially used to encapsulate the open microchannel ports which were connected to thin copper wires. However, as it was reported in previous works [89], motion of the wires interfacing the LM in the microchannels with multimeter probes causes scattering during pressure testing. Therefore, we have explored an alternative method by sealing the microchannel ports with conductive epoxy (8331 Silver Conductive Epoxy Adhesive, MG Chemicals), and then gluing thick braided copper wires to each electrode with the same adhesive. To expedite the manufacturing procedure, a hot plate was used to speed up the adhesive curing process to 10 minutes at 70°C. This allowed a great interface between soft and hard conductive materials.

4.2 Pressure Sensor FEM Simulation

Finite elements analysis (FEA) of the 3D-printed soft pressure sensor device was carried out using a multiphysics software (Abaqus/CAE, Dassault Systemes). The simulation was conducted to understand the range of compressive strains experienced by the sensor, which will be instrumental in deriving the gauge factor of the sensor when the latter is treated as a strain gauge sensor. A simple geometry representing the sensor substrate was created following the same physical dimensions. In this study, to facilitate computation, we have considered the microchannel cavities and the liquid metal as solid but soft materials with similar properties as the substrate. The material property

was set as Agilus30 using the Odgen hyperelastic model (Table A1) with parameters μ_1 = 0.2127 MPa, α_1 = 1.3212, μ_2 = 0.0375 MPa, α_2 = 4.318, μ_3 = 0.001, α_3 = 1.0248 which were determined in previous work [99]. A quasi-static uniaxial strain was simulated by applying a pressure input of up to 1 MPa with increments of 0.1 MPa per step. The sensor substrate was meshed with 280 quadratic hexahedral elements and 2058 nodes (C3D20RH). A fixed boundary condition was set on the bottom surface of the sensor to prevent planar rotation and displacement. The pressure on the top surface was defined by circle with a diameter of 16 mm centered at the sensor active area in order to replicate the experimental setup. Figure 4.4 shows the obtained contour plots for von-Mises stress, displacement and logarithmic strain along the load axis. The average strain was computed among all nodes inside the applied pressure region (Figure 4.5).

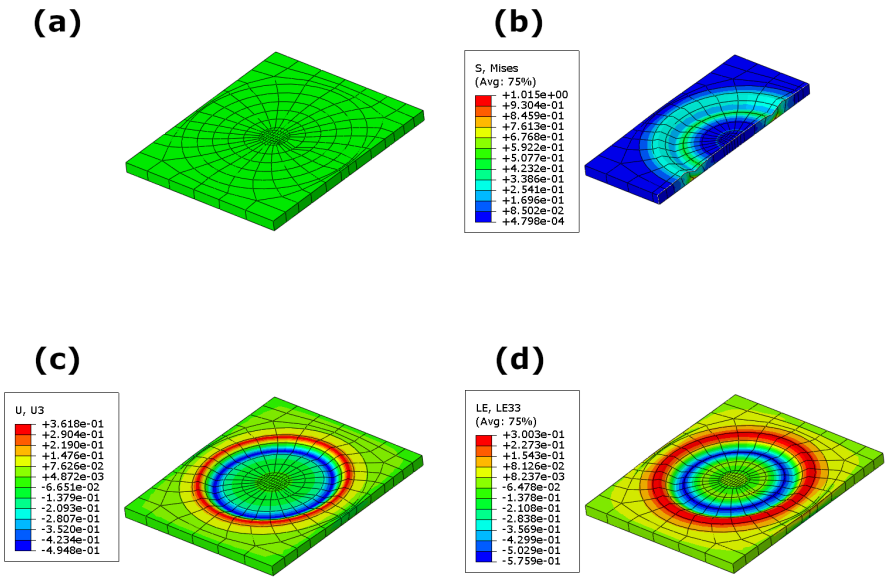

Figure 4.4: Contour plots of the simulated soft pressure sensor for an applied pressure of 1 MPa. (a) Substrate geometry meshed with hexahedral elements of type C3D20RH; (b) cut-view of the von Mises stress; (c) spatial displacement at z-direction; (d) logarithmic strain at z-direction.

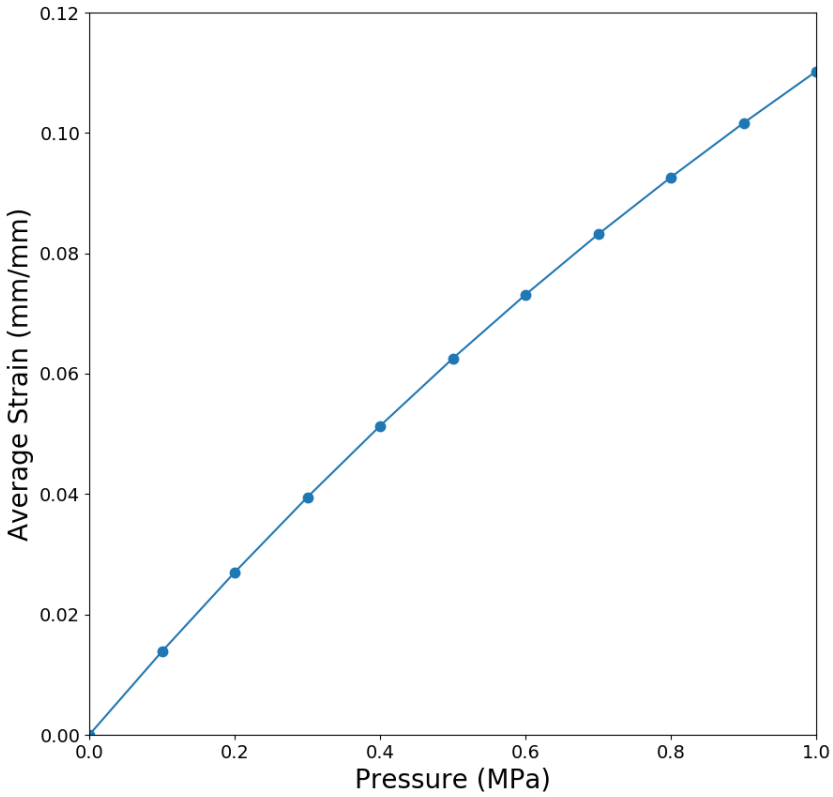

Figure 4.5: Pressure versus strain plot obtained from the FEA simulation results. The strain values correspond to the average strain among all nodes inside the applied load region (172 nodes).

4.3 Experimental Setup, Sensor Measurements and Modeling

4.3.1 Experimental Setup

A force testing device was built for conditioning and characterizing the microfluidic pressure sensors. We used a pneumatic cylinder (1.06DPSR02.0, Parker Hannifin) with a bore diameter of 1.0625 inches (≈27 mm) and rod diameter of 0.3125 inches (≈8 mm) and mounted to a rigid frame in a vertical position. A custom-built metallic force concentrator (6061 Aluminum) of 16 mm in diameter (80% of sensor active area) was threaded to its rod end in order to distribute the

applied pressure over the sensor top surface. The sensors were adhered to a flat surface under the air cylinder rod end, while keeping it concentric to the microchannel spiral shape (Figure 4.6). A miniaturized pneumatic controller board was used to control the pressure of a compressed air pipeline source. The wall outlet maximum pressure was set to 80 psi with a pneumatic filter regulator. The air pressure at the pneumatic cylinder was controlled by a solenoid valve (VQ110U-6M, SMC USA) connected to a MOSFET switch, which was modulated via a programmable microcontroller (Arduino Mega 2560, Arduino) using a PID controller algorithm for pressure setpoint tracking. Sensor measurements were collected using a voltage divider circuit ($R_{ref} = 47\Omega$) and connected to the same programming board using its analog-to-digital converter pins with the default internal voltage of 5 V. Two insulated copper test leads with alligator clips were used to connect the pressure sensor terminals to the voltage divider circuit. All sensor data was recorded via serial communication using a Python script running on a workstation computer during both conditioning and characterization procedures. The total pressure at the sensor top surface, P_{surf}, was determined by

$$P_{surf} = \frac{P_{gauge} \times A_{bore}}{A_{puck}} = \frac{F_{rod}}{2.01 \times 10^{-4} m^2} \tag{4.1}$$

where P_{gauge} is the total pressure inside the air cylinder, A_{bore} is the bore area, A_{puck} is the area of the force concentrator, and F_{rod} is the force generated at the rod.

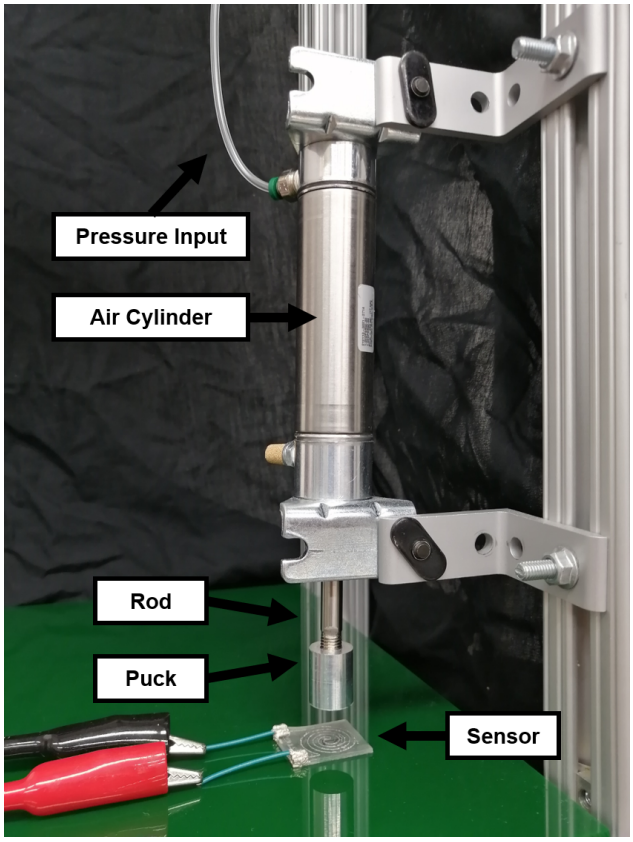

Figure 4.6: Test rig for measuring and characterizing the 3D-printed pressure sensors. A vertically mounted fluidic cylinder with custom-built force concentrator (16 mm diameter) and controlled by a pneumatic power source.

4.3.2 Pressure Sensor Response

The relative change in electrical resistance of the 3D-printed microchannel filled with liquid conductor, $\Delta R/R$, was recorded as a function of the generated pressure at the force concentrator, P_{surf}. The sensor response was first evaluated by applying a step signal of 30 psi at the gauge (P_{surf} = 0.6 MPa). The obtained experimental result shows that the sensor can quickly respond to the pressure input, but then takes about 500 seconds to reach the steady-state, with $\Delta R/R \approx 7.2$ as shown in Figure 4.7. This observed creep can be partly explained by the viscoelasticity of the 3D-printed resin material as discussed in [100].

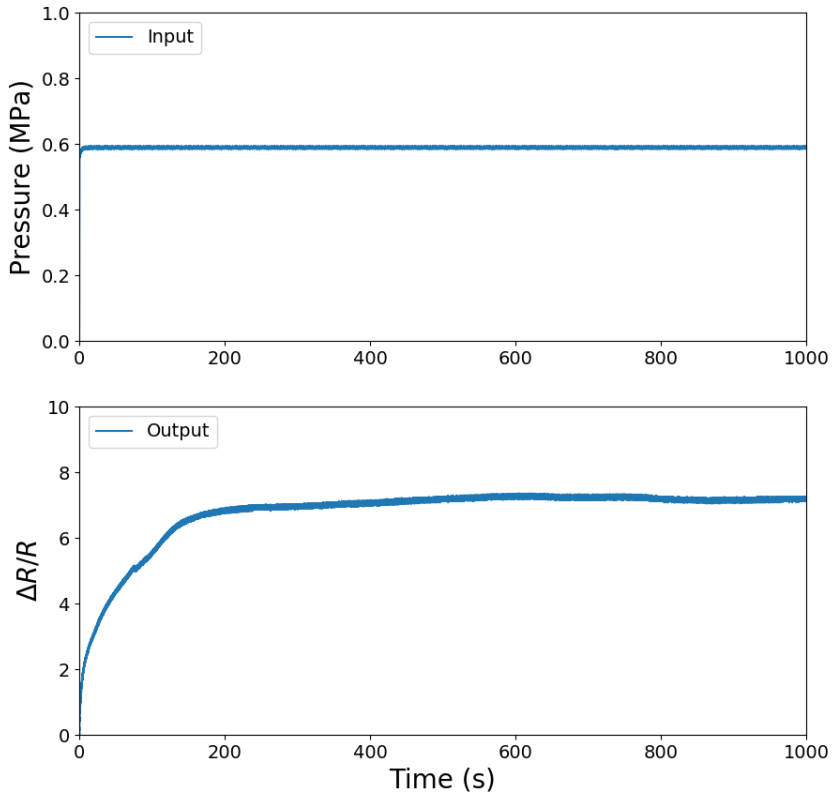

Figure 4.7: Step response collected from the pressure sensor for a constant input of 0.6 MPa. The top graph shows the input pressure and the bottom graph shows the measured relative change in resistance.

Further computational study was performed to identify a model with these intrinsic characteristics. The sensor data obtained during the step response experiment was imported in a software (MATLAB, Mathworks) to estimate a transfer function model. Equation 4.2 shows the estimated transfer function model from the time-domain data with a fit to estimated data of 93.23% and represented as a second order system with two poles and one zero. In Figure 4.8, we can observe a comparison between the experimental data and obtained transfer function step responses. The step response characteristics of the identified model were a rise time t_r = 150 seconds, a settling time t_s = 272 seconds, and a peak time t_p = 512 seconds.

$$G(s) = \frac{\Delta R/R}{P_{surf}} = \frac{1.406s + 0.07097}{s^2 + 0.4516s + 0.005858} \tag{4.2}$$

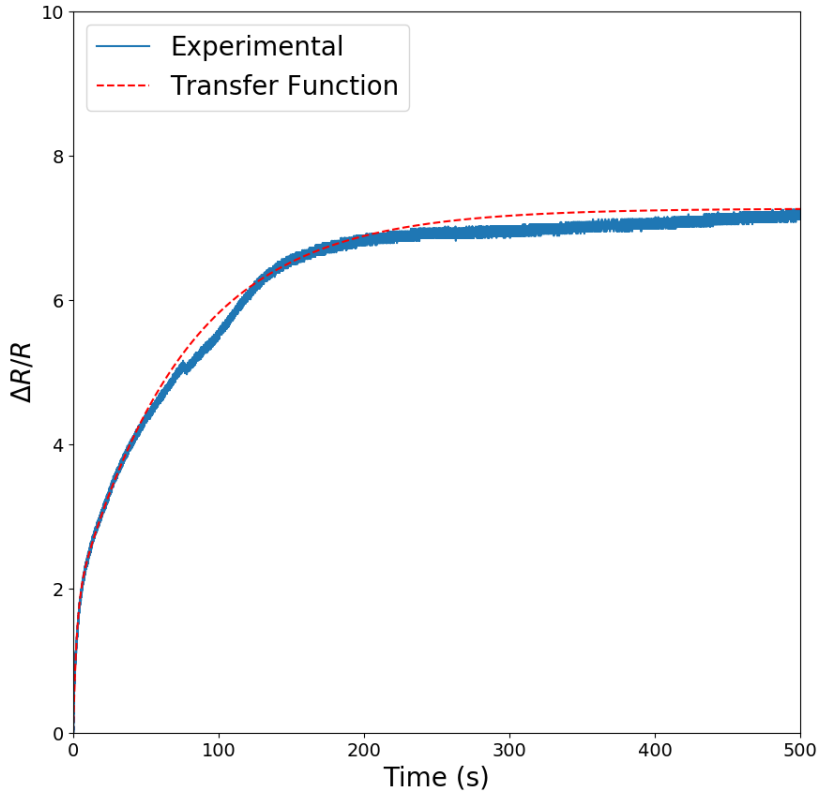

Figure 4.8: Comparison of a step response for both the experimental data and the obtained transfer function through model fitting.

To analyze the sensor response at multiple frequencies, a sinusoidal wave was generated with frequency f_s = 0.1 Hz, 0.25 Hz, 0.5 Hz and 1 Hz, bias of 30 psi and amplitude of 20 psi at the gauge (0.2 MPa $< P_{surf} <$ 0.977 MPa). Figure 4.9 shows the relative change in resistance when this cyclic signal was applied for a period of 2000 seconds at each frequency value. A mean curve shows the average values of $\Delta R/R$ computed at each respective T_s cycle. A close view of each measurement is shown in Figure 4.10. The particular creep phenomenon is still observed under he

cylic inputs, and the time it takes the mean curve to reach the steady state is comparable to the case of a quasi-static input (Figure 4.7). The sensor output versus pressure graphs on Figure 4.11 were generated by capturing the relative change in resistance after the sensor has reached its steady-state regime ($>$ 1000 seconds).

Although the electrical characteristics of the sensor have not been investigated during the simulation analysis, the resistance of the sensor output was collected at different pressure values for further correlational study between simulation and experimental results. In order to measure the sensor resistance close to steady-state regime at multiple pressures, a staircase pressure signal with increment size of 0.1 MPa and duration of 2000 seconds per step was applied to the control board. An average value for the relative change in resistance at each pressure step was computed for a range of 100 points along the steady-state regime (Figure 4.12). By combining the simulation results from Figure 4.5 with the experimental results from Figure 4.12, we have achieved a correlation between the pressure sensor average strain inside the load region and the observed relative change in resistance for a given applied pressure value (Figure 4.13).

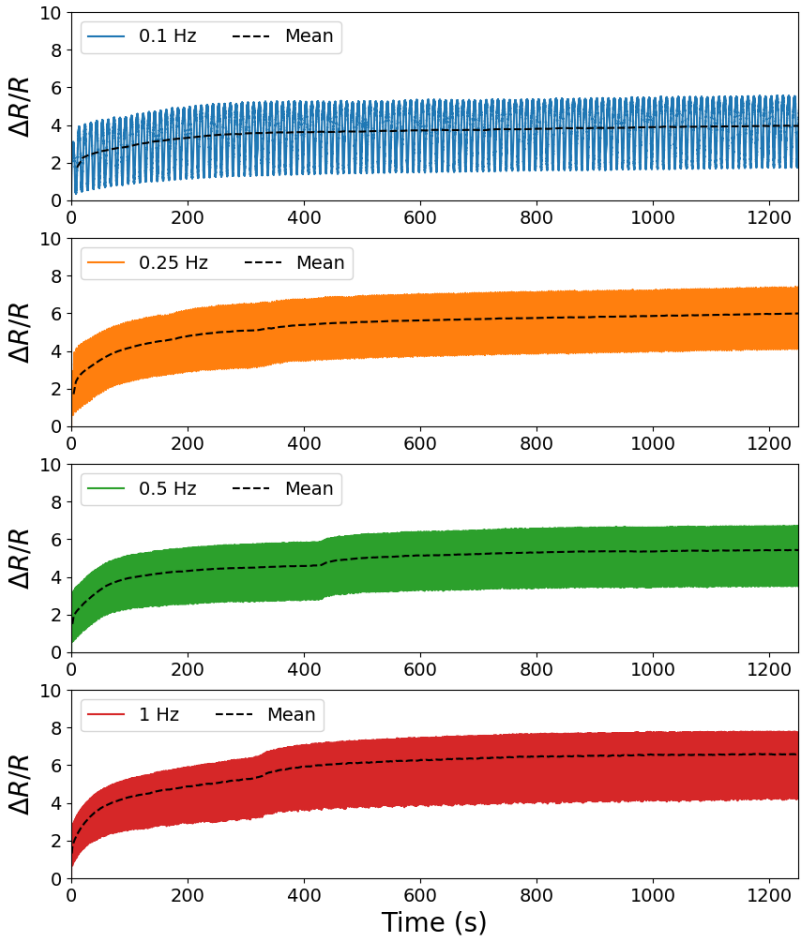

Figure 4.9: The pressure sensor output under sinusoidal sensor input with range from 0.2 to 0.977 MPa, with four different frequencies (0.1 Hz, 0.25 Hz, 0.5 Hz, and 1 Hz). The dashed lines show the mean curve of the continuous measurements.

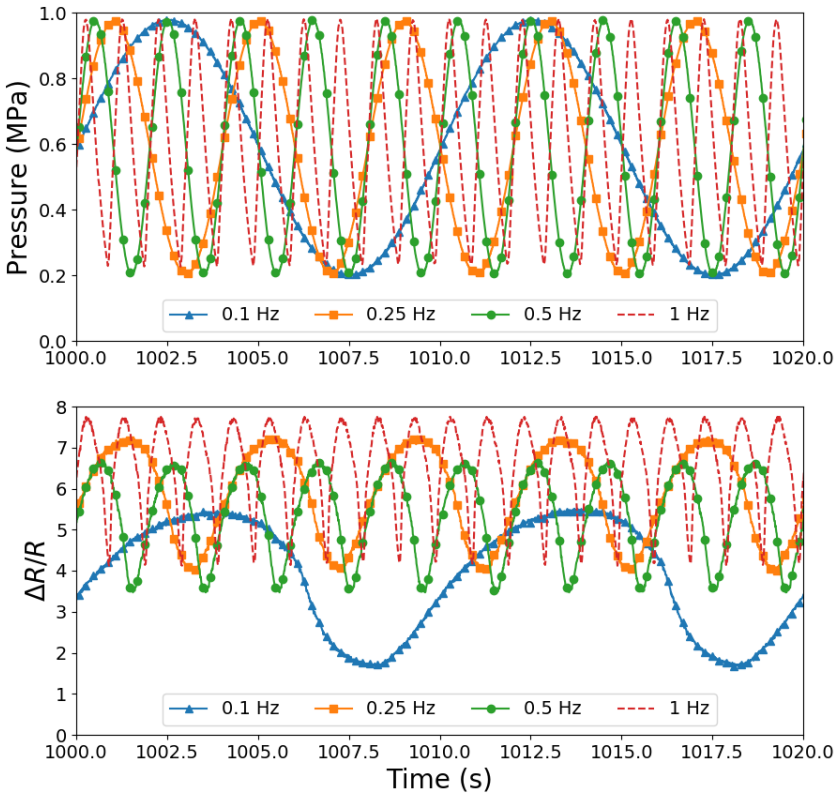

Figure 4.10: Sinusoidal response for multiple input frequencies (frame view of 20 seconds). Each measurement was collected for >2000 seconds at 0.1 Hz, 0.25 Hz, 0.5 Hz, and 1 Hz, with a pressure range of 0.2 MPa to 0.977 MPa.

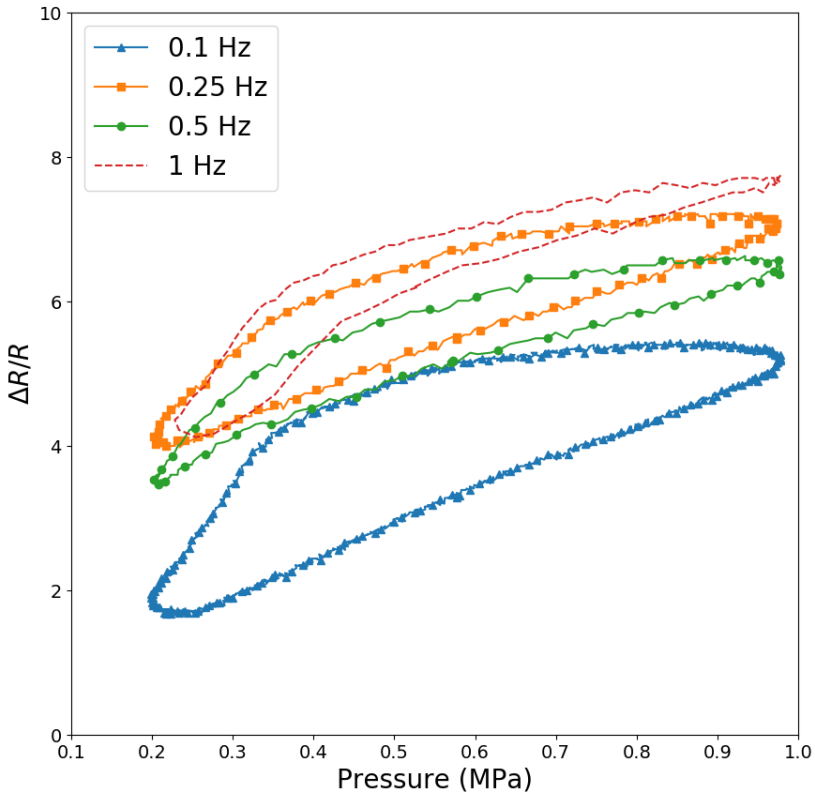

Figure 4.11: Graph for each sinusoidal input frequency after reaching the steady-state.

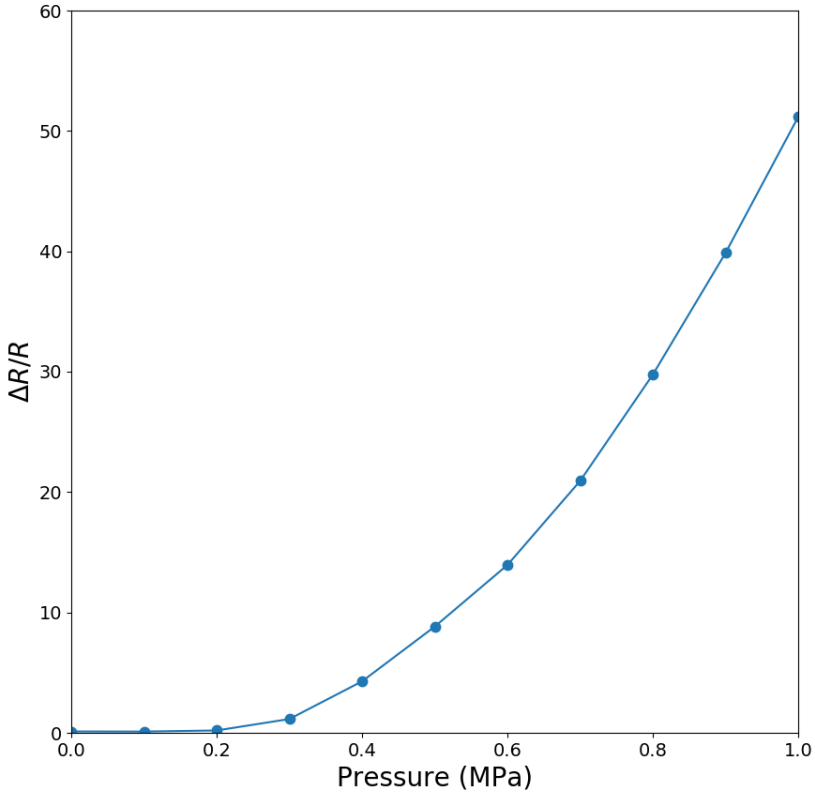

Figure 4.12: The relative change in resistance versus the pressure input for a staircase input signal. The average value of $\Delta R/R$ was computed for a range of 100 points along the steady-state regime, with a pressure input from 0 to 1 MPa, increment size of 0.1 MPa, and duration of 2000 seconds per step.

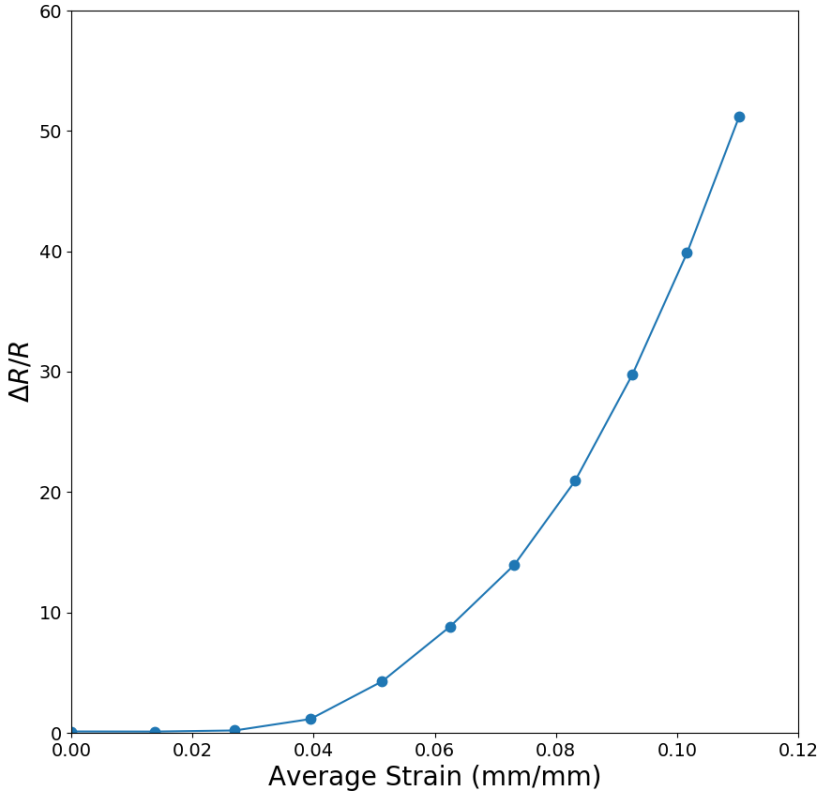

Figure 4.13: The correlation between the computed average strain from FEA simulation at the sensor active area and the relative change in resistance measured from the physical pressure sensor device.

4.3.3 Further Discussions

Dispersion of the liquid sacrificial material is still a challenge process in the fabrication technique presented here, since accidental formation of beads can cause clogging or irregular structure design of the microfluidic channels. Moreover, the manual removal of the liquid support material through suction with a vacuum pump, and the manual injection of liquid metal using syringes have varied fabrication time due to non-uniform tool manipulation and material handling. A way to improve our fabrication method would be to make these procedures automated by the same 3D-printing mechanism.

The intrinsic viscoelasticy of the rubber-like photocurable material has shown some impact on the soft pressure sensor response time, taking up to 500 seconds for the sensor to reach a steady-state regime. Additional investigations on substrates made of different mixing ratios between soft and rigid 3D-printable photopolymers and overall thicknesses are required in order to analyze their impact on the sensor performance.

Encapsulation of the pressure sensor inlets was performed by using silver epoxy as an interface between the liquid conductor and copper stranded wires. Other methods have been tested initially such as deposition of uncured Agilus30 on the sensor terminals with thin copper wires attached at each end, and curing process using UV-light flashlight. However, poor quality deposition or curing caused leakage of the liquid metal when subjecting the sensor to very high pressure values. 3D-printing of an encapsulation layer has also been tested, but the attached thin wires and the liquid metal exposed surface made it a challenging process due to blockage or undesired contamination of the printer head. Although the selected silver epoxy showed great adhesion and encapsulation properties, further study is needed to analyze its effect on the sensor characteristics. Also, the surface oxide skin on a liquid metal can affect the effective surface tension and viscosity (non-spherical droplets formation), which can reduce its contact with other materials and potentially impacting its electrical properties.

Chapter 5

Computational Evolution of Control and Tactile Perception for Soft Robots

5.1 Evolutionary Robotics with Soft Robots

Although many studies can be performed within a simulated world about robots with evolved control systems or morphologies, an evolved AI model can potentially be transferred to a real-world robot to improve its physical functionalities. The limitations of a virtual environment used in the evolution of robot controllers and body-plans are determined by the simulator capabilities. A real-world robot with multiple degrees of freedom that will interact with different objects or obstacles on its workspace requires a simulator that can compute a large number of variables in order to closely represent the characteristics of the world around it. Physics engines are commonly used in evolutionary systems since they provide a collection of libraries that can perform real-time computation of rigid body kinematics/dynamics, collision detection, mass-spring systems, and fluid mechanics in 2D and 3D spaces [101]. As an example, one study approach uses a physics engine (Nvidias PhysX) to coevolve the material properties and locomotive gaits of complex soft bodies built out of tetrahedral meshes [102]. In addition, evolving soft robots with multiple materials and generative encoding such a compositional pattern-producing network (CPPN) can lead

to soft-voxel based systems (VoxCAD) with a large diversity of complex, natural, multi-material creatures [58][60][103]. Results have shown that this evolutionary process can generate soft robots with different morphologies and gaits, squishy creatures that can reach or squeeze through tight apertures, and multiple locomotion strategies for space-exploration. An investigation using Covariance Matrix Adaptation Evolutionary Strategy (CMA-ES) demonstrated that evolving controllers for a knifefish-inspired soft robot is feasible directly on the physical robot, which was able to outperform a hand-designed controller in terms of robot travel speed [104]. Since soft robotics is still a growing field, new simulation techniques are being developed to overcome some of the ongoing challenges in real-time computation of soft actuation and sensing mechanisms.

An open-source simulator with multi-model representation shows great potential for simulating soft robots and their interactions with the outside world. The Simulation Open Framework Architecture (SOFA) is a computational library primarily targeted for simulating tissues, muscles, organs, and bones in medical applications [105]. Since programming the interaction of rigid and deformable materials requires various techniques in geometric modeling, computation mechanics, numerical analysis, collision detection, and rendering, the SOFA architecture was built based on a highly modular framework that facilitates collaboration between researchers while being able to focus on a certain domain of expertise. Each simulated object can be decomposed into multiple subcomponents describing the model features such as mesh topology, mass, forces, integration scheme, and constraints, in a scene graph data structure. In particular, a new method was studied to control soft robots for object manipulation or rolling motion using finite element method (FEM), friction contacts, and quadratic program with complementarity constraints in SOFA [106]. Moreover, a geometric computing framework which predicts the deformation of continuum soft bodies under geometric actuations can be tested both in physical and simulated robots, allowing relationship studies between material properties and shape parameters [107]. The development of an efficient soft-hand simulator based in SOFA enabled the feasibility study of co-designing morphology of soft hands and their control strategies for grasping, with computation time fast enough to simulate more than a million grasps per day [108].

As an initial step towards the evolution of controllers for soft robots, we explored the integration of standard neural networks (ANN, RNN) with the SOFA platform for computing the desired behavior of a SPA in a specific task space (curvature, positioning, or grasping). Neural networks can be described as mathematical models defining a function, or depending on its structure size (number of layers), a composite function with many subfunctions within it. Some components of a neural network are neurons, connections, weights, biases, and activation functions. The structure of a given neural network can be computationally evolved using genetic algorithms. Since the mathematical modeling of soft robots presents difficulty at many levels (nonlinear material properties, parameter uncertainties), and it is a crucial process for designing controllers in robotics, a neural network can potentially be used for converging a simulated soft-bodied robot to a targeted behavior. In one study, a type of recurrent neural network called a long short-term memory (LSTM) network was used for learning the time series mapping of redundant and unstructured sensor topology embedded in a soft actuator, enabling the modeling of a soft continuum actuator in real time while being robust to sensor nonlinearities and drift [109].

Robust object manipulation in unstructured environments is a challenging problem in robotics due to the uncertainty associated with complex and unpredictable environments, and with object shape and hardness. Conventional object grasping techniques involve prior knowledge of the robot workspace such as 3D models of objects and manipulators, as well as their weight and friction properties. These methods are limited to applications where the robotic hand model is known and the object shape is well-defined or simplified by geometric primitives. Although rigid articulated fingers can assist with predicting a specific grasping configuration, these mechanisms can be expensive to fabricate and control. In addition, they are not suitable for grasping and handling soft, fragile objects. As an alternative, compliant robotic hands can be fabricated using soft materials, allowing adaptivity when handling irregularly shaped or delicate objects, and increasing the tolerance with uncertainties in perception and actuation. However, specific configuration at a given time is hard to know due to the hand compliance, requiring advanced internal sensing mechanisms and novel sensory-motor interface models for soft robots. By training a three-dimensional deep con-

volutional neural network (3D CNN) for grasping unknown objects with soft hands, a soft robotic hand was able to estimate suitable grasp poses from multiple grasping directions and wrist orientations, with 87% successful grasping on previously unseen objects [21]. Proprioceptive capabilities for soft robotic hands can be achieved by using a clustering algorithm for autonomous object identification and force-controlled grasping with pose uncertainty [22]. However, this approach is limited by constrained sensor designs and requires a camera in order to detect approximate object locations.

In order to evolve controllers for soft robotic hands, which can potentially identify object hardness or provide pose estimation for decision making tasks, it is necessary to use a model that can facilitate the switching between multiple desired states. A Markov Brain (MB) can be used as the substrate, where the robot controllers are networks built from individual computational components [110]. These components interact with each other and the outside world and can be defined as deterministic or probabilistic logic gates, thresholding functions, timers and counters. In addition, an MB is composed of a state buffer (state vector) where each element represents one node. An MB update applies a set of computations defined by the MB components in this buffer. Multiple inputs can be written into a part of this buffer before the MB update, and outputs can be retrieved from a subset of this buffer once an MB computation is completed. The state of an MB can be changed much more easily, which makes MB a better approach for fine-grained behavior, and well-suited for the integration of temporal information [111][112].

In this chapter, we have investigated the evolution of MBs using the Modular Agent Based Evolver (MABE), which is a modular and reconfigurable digital evolution tool for biology and engineering research [113]. Furthermore, multiple AI models such as ANNs, Cartesian Genetic Programming (CGPs), and MBs have been evolved in MABE to properly classify the shape and stiffness of grasped objects as well as the soft hand parameters. These artificial brains can potentially be transferred to real-world soft robots to evaluate their task performance and facilitate prototyping. Evolved controllers for a given coupled body-plan/actuation mechanism will contribute to building more adaptive and resilient soft machines in the near future.

5.2 Evolving Markov Brain Controllers for Robotic Grasping

This work involves the evolution of proprioceptive sensing-capable controllers for soft robotic grippers using MBs for potential transferring the evolved controllers to real-world soft robots. We first investigated the implementation of an FEM-based curvature feedback control of a SPA using a PID controller and the SOFA simulator. The control algorithm runs in parallel with the FEM simulation, which computes the soft actuator mesh deformation in relation to its chamber inner pressure. The curvature is calculated with respect to the fixed-end and distal-end mesh nodes (centerline) along the SPA bottom surface (inextensible layer). The PID gains for this experiment were tuned based on trial and error. As shown in Figure 5.1, the desired SPA curvature is achieved for the given setpoint value.

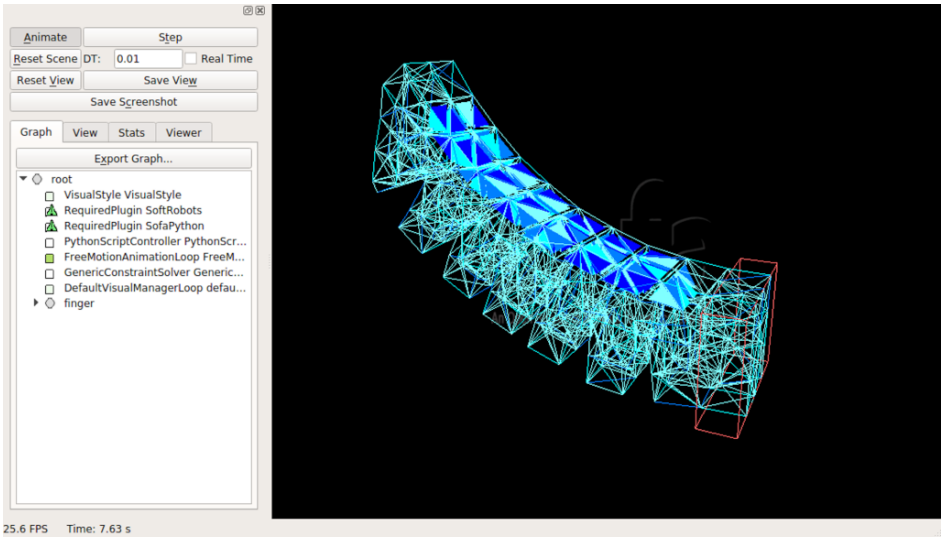

Figure 5.1: An FEM-based real-time curvature feedback control of a SPA. The results were achieved using a PID controller and FEM-based simulation in SOFA with different material properties.

We have simulated multiple soft pneumatic grippers with different numbers of fingers using the SOFT ROBOTS plugin (DEFROST Team, INRIA) for SOFA and manually controlled them with a Human-Machine Interface (HMI) (see Figure 5.2a-d). All geometries have been simulated with tetrahedron meshes using the TetrahedronFEMForceField component and contact detection

and handling through the default collision pipeline. In addition, a Python script was developed to control the soft gripper in real-time, varying the simulated internal pressure based on the feedback from bending sensors embedded within a soft wearable glove. The sensor analog signals were processed by a microcontroller (Arduino Uno Rev3, Arduino) and converted to grasping actions via serial (USB) communication.

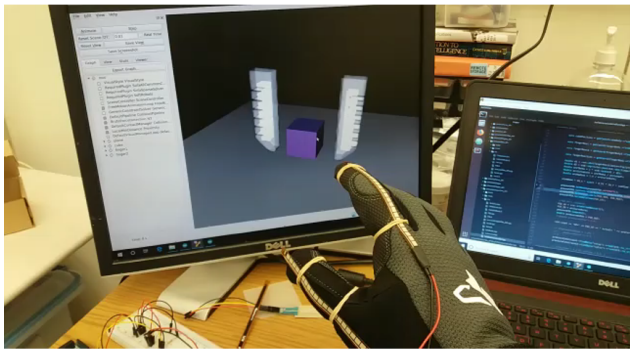

(a)

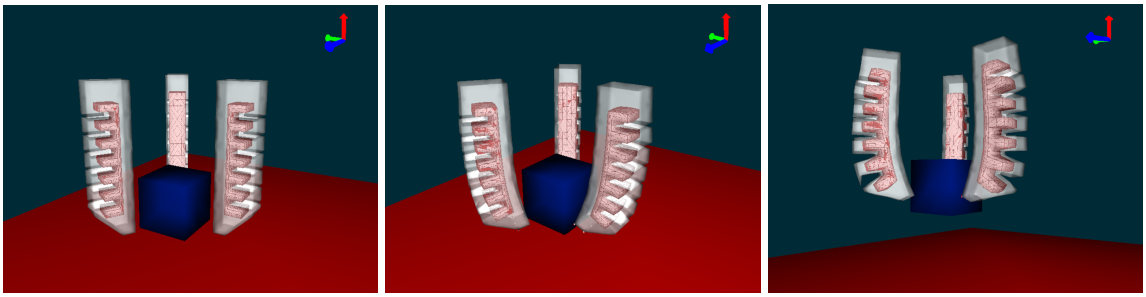

(b) (c) (d)

Figure 5.2: Soft robotic gripper manual control using Human-Machine Interface (HMI) with SOFA. (a) A soft wearable glove with bending sensors connected to a microcontroller for processing the analog signals, (b) soft gripper with three fingers in unactuated state; (b) soft fingers touching an object with collision detection; (c) object being lifted by the soft gripper with pinching grasping mode.

Even though external inputs from wearable devices were capable of controlling a simulated soft robotic gripper in real-time, additional information from the simulation environment is required for achieving controllers with proprioceptive feedback. For achieving such a goal, we have defined a classification task challenge for evolving artificial brains capable of determining different conditions from the simulation environment. In order to detect an object shape and stiffness, force

values on specified mesh nodes (see Figure 5.3) were measured at the soft pneumatic actuator tip and saved to a spreadsheet file during each iteration. The simulation run time was set to 1.25 seconds, with a timestep of 10 milliseconds and an increment size of 0.01 for total internal surface pressure. The following values were recorded in the file: current simulation time, soft finger internal pressure value, and force values at XYZ directions for all three selected nodes. These 11 data types were used as inputs for training artificial brains capable of performing a classification task.

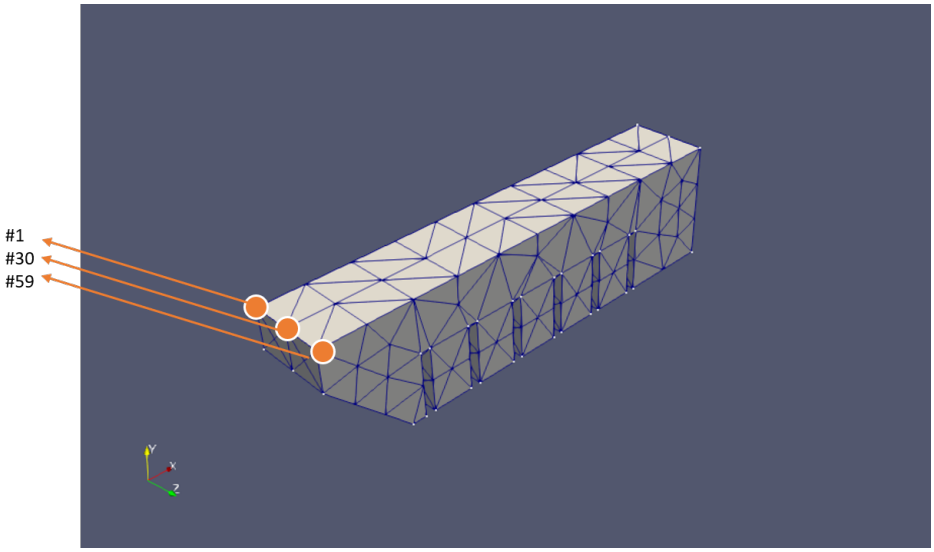

Figure 5.3: Soft finger mesh node locations for probing force values during each iteration step in the simulated workspace. The following mesh node numbers at the SPA tip were selected: 1, 30, and 59.

The first approach was to test the classification of three distinct soft grasping characteristics: object shape, object stiffness, and the number of contact fingers. In order to facilitate the evolutionary process, we have constrained the problem to two different object shapes (cube or sphere), three stiffness levels (soft, medium, or hard), and two types of contacts (one or two fingers). The stiffness values for each simulated component are presented in Table A4. Figure 5.4 shows the soft fingers interaction for a cube object, and the respective emulated force measurements are presented in Figure **??**. Similarly, Figure 5.6 shows the soft fingers interaction for a sphere object, and the respective emulated force measurements are presented in Figure **??**. We have used the Modular Agent-Based Evolver (MABE) platform to evolve multiple artificial brains using different types

of connecting logics such as standard ANNs, Markov Brains, and Cartesian Genetic Programming (CGPs). The classification task was evolved offline, with all force measurements stored in spreadsheets being loaded to the artificial brain for each evaluation case. The loaded files followed a naming convention according to the simulated conditions (object type, numbers of fingers, and object stiffness), with each condition represented by a bit value (Table A5). The number of input neurons and output neurons were defined based on the number of data columns in a spreadsheet (11 inputs) and the number of conditions (5 outputs), respectively. A scoring was set as 1 point for each correct output, with a maximum of 5 points in classifying each case correctly. The maximum fitness value achieved in a solution was defined as 120, where:

$$Maximum\ Fitness = 12\ cases \times 2\ runs \times 5\ conditions = 120 \tag{5.1}$$

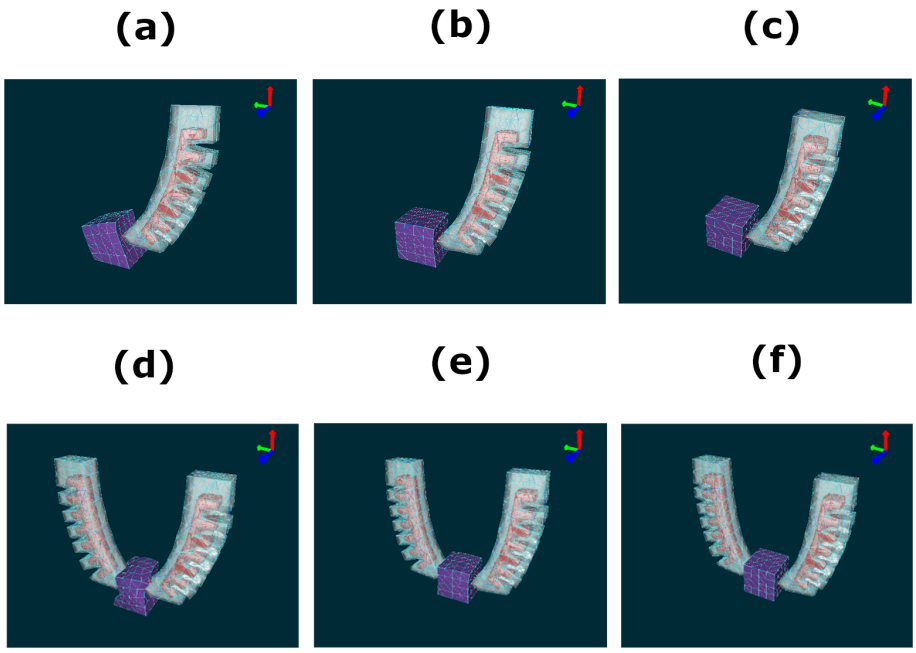

Figure 5.4: Soft fingers at final simulation timestep (maximum inner chamber pressure) in contact with a cubic object with different stiffness values. Single soft finger in contact with (a) soft, (b) medium, and (c) hard cube. A dual soft finger gripper in contact with (d) soft, (e) medium, and (f) hard cube.

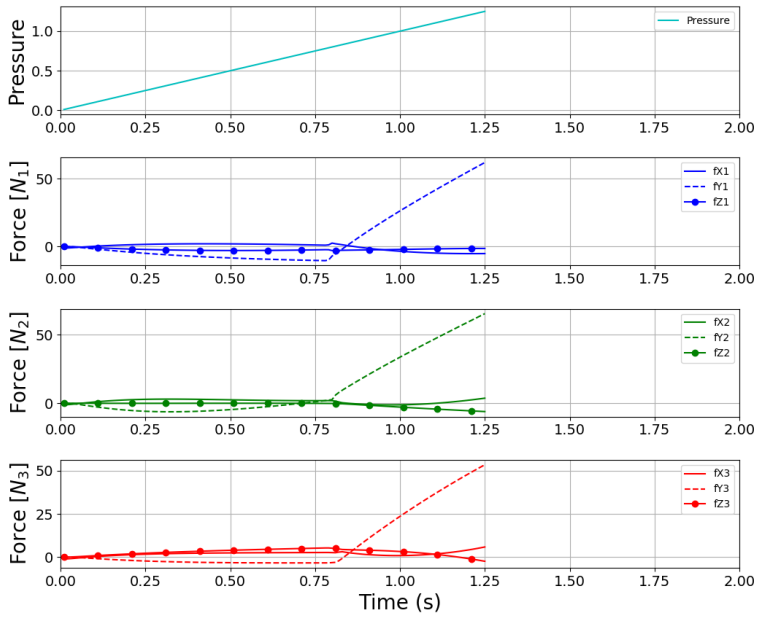

(a)

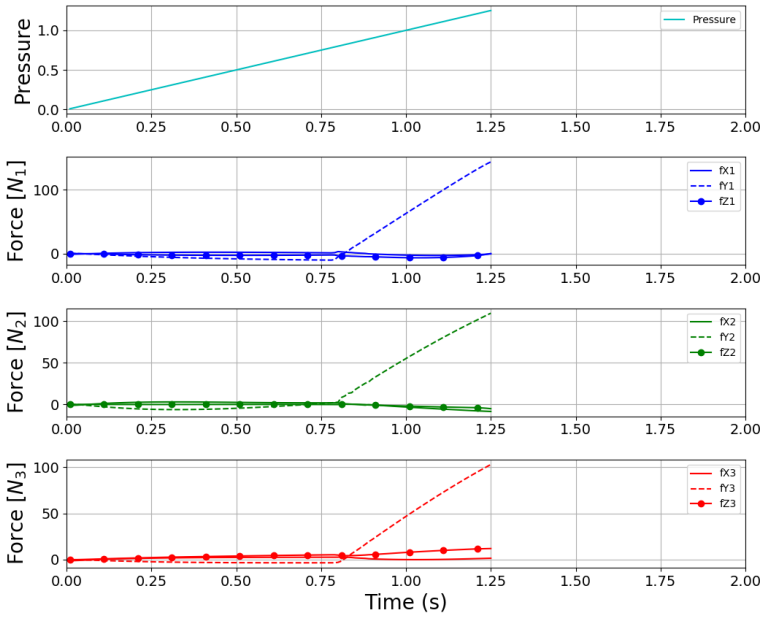

(b)

Figure 5.5: Force values (XYZ directions) at the SPA tip in contact with a cube. Probed mesh nodes for a single finger and a dual finger gripper in contact with a soft (a-b), medium (c-d), and hard (e-f) cubic object.

Figure 5.5 (cont'd)

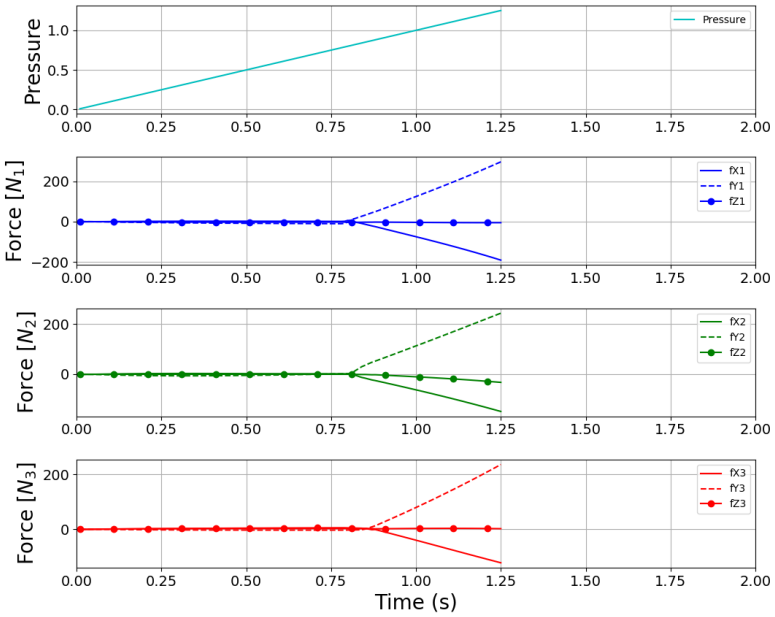

(c)

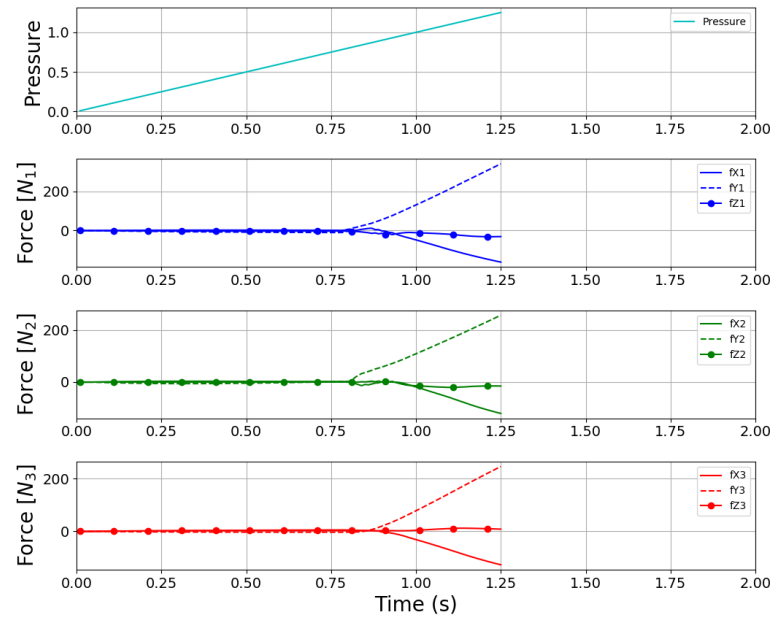

(d)

Figure 5.5 (cont'd)

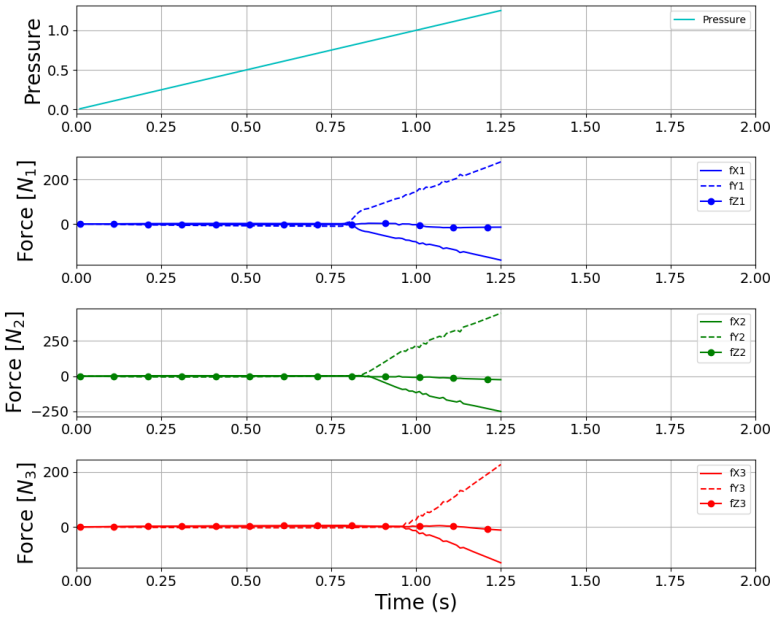

(e)

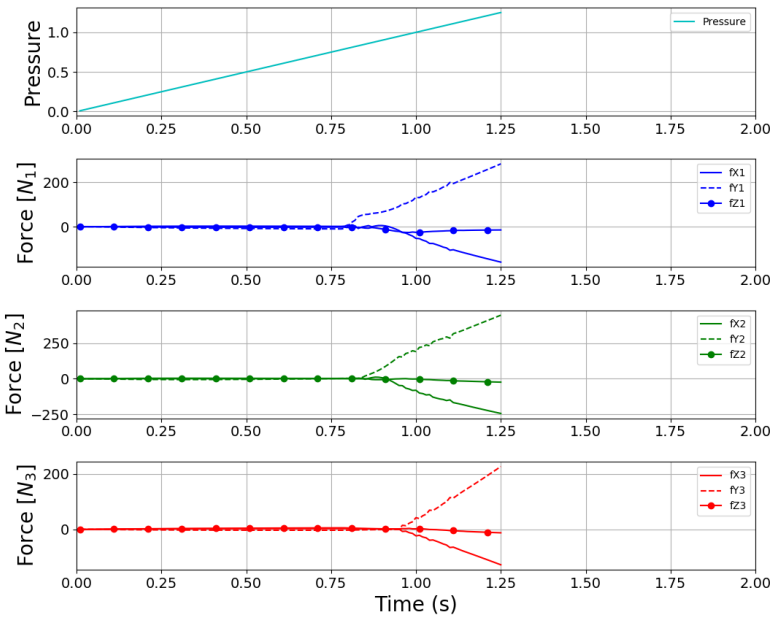

(f)

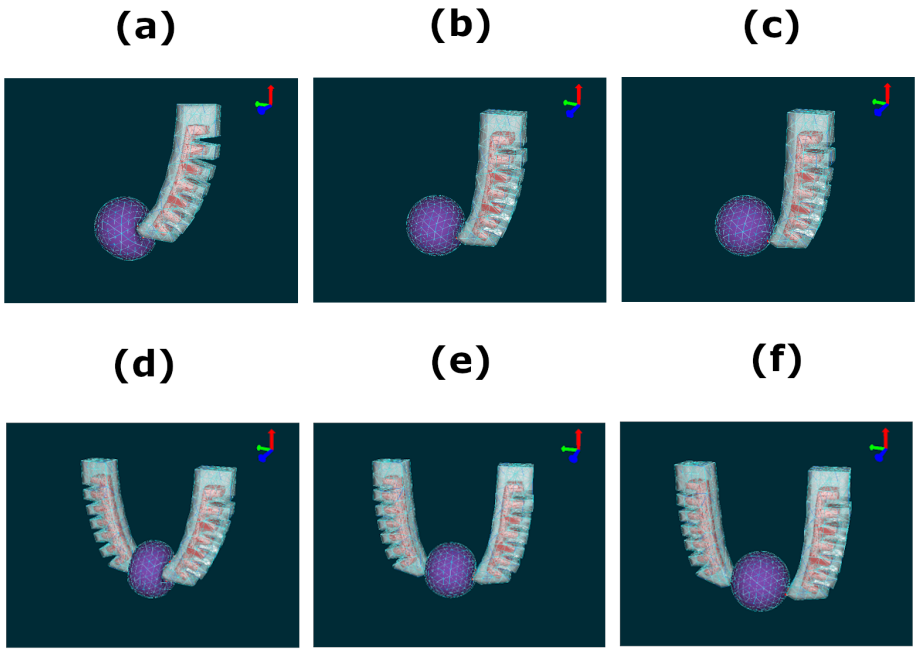

Figure 5.6: Soft fingers at final simulation timestep (maximum inner chamber pressure) in contact with a spherical object with different stiffness values. Single soft finger in contact with (a) soft, (b) medium, and (c) hard sphere. A dual soft finger gripper in contact with (d) soft, (e) medium, and (f) hard sphere.

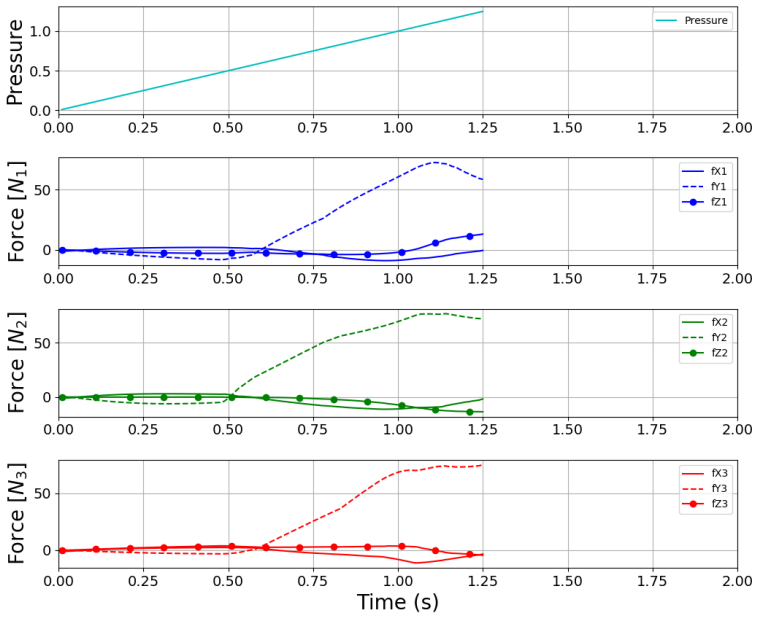

(a)

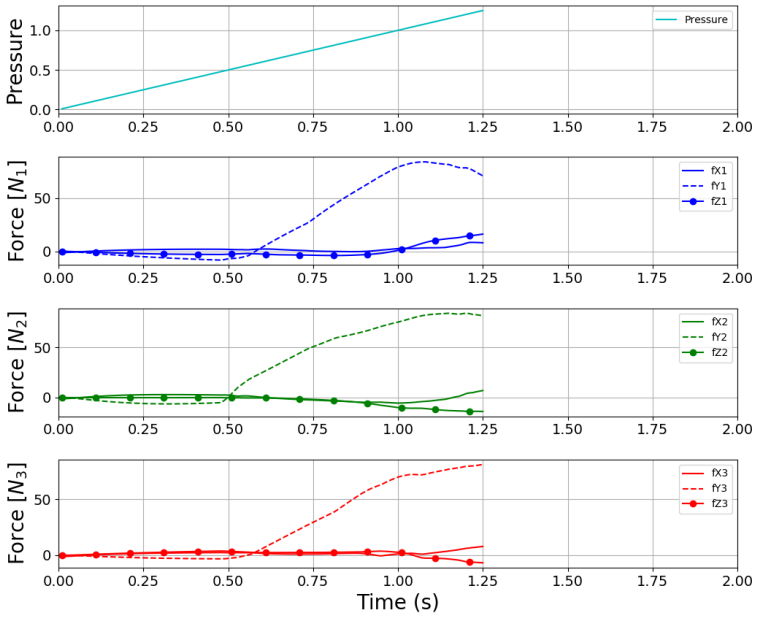

(b)

Figure 5.7: Force values (XYZ directions) at the SPA tip in contact with a sphere. Probed mesh nodes for a single finger and a dual finger gripper in contact with a soft (a-b), medium (c-d), and hard (e-f) spherical object.

Figure 5.7 (cont'd)

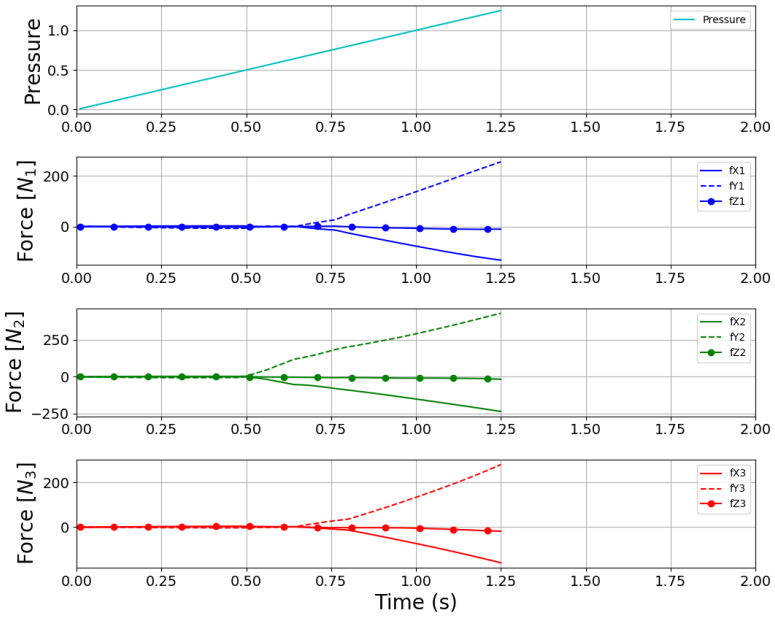

(c)

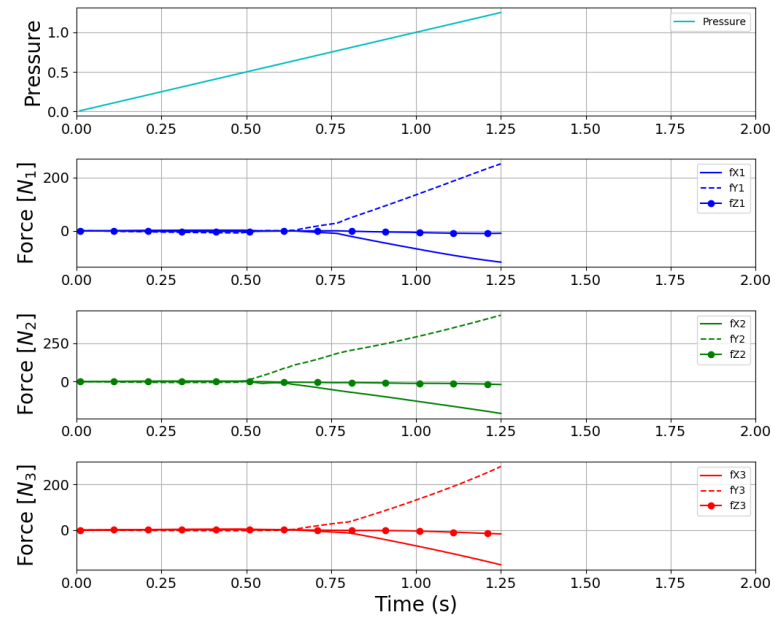

(d)

Figure 5.7 (cont'd)

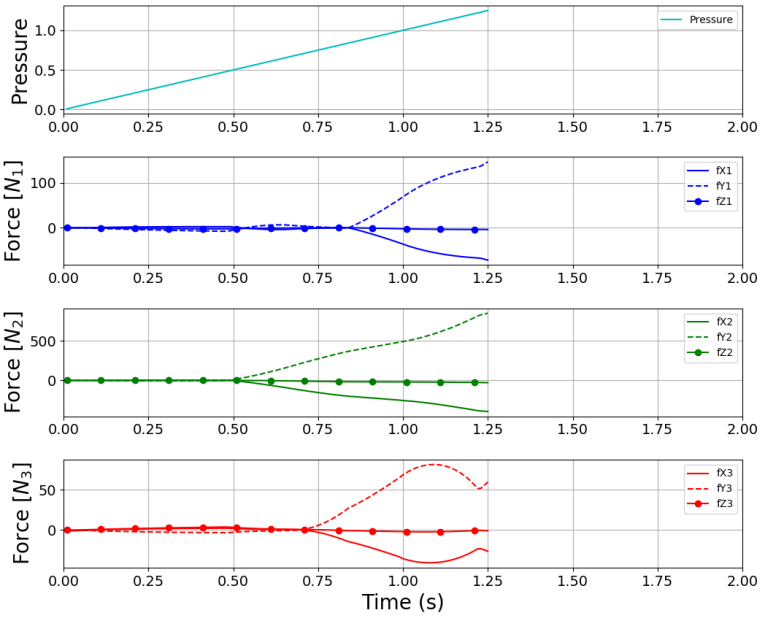

(e)

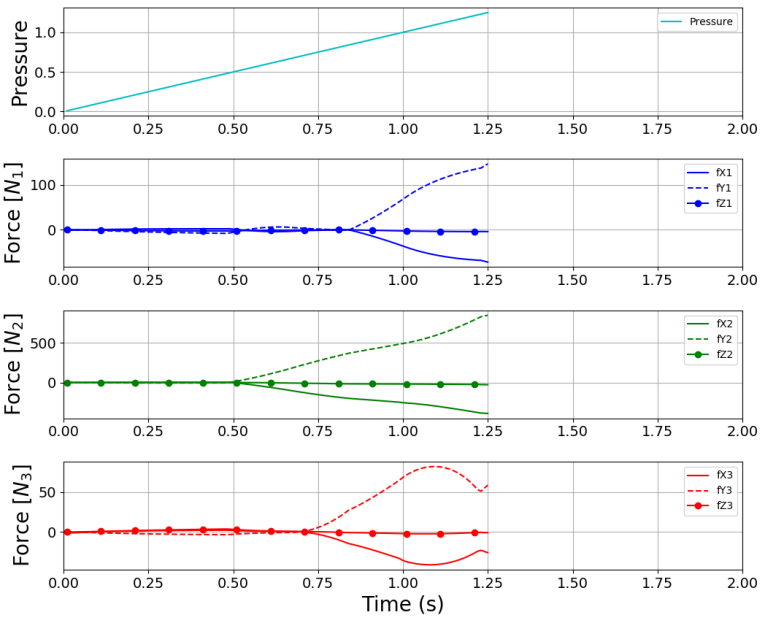

(f)

In this neuroevolution procedure, we have selected Tournament Selection method as the optimizer type, with a tournament size of 25. As an initial test, we have defined a population size of 100 agents with all candidate solutions competing against each other for 1,000 generations. The initial genome size was defined as 5,000, with a minimum size of 2,000 and maximum size 20,000. Copy and deletion mutations had an insert rate of 0.00002 and the point mutation rate was set as 0.015 (select genome site and randomize its value). In MABE, the MBs were configured with 8 hidden nodes and a starting number of gates of 6. In addition, their internal gates were set as TRIT types, where outputs can have values of 1, 0, or -1, and GP types, where outputs are continuous values generated via mathematical operations and functions. A custom-built world (interface between brains and simulated states) was designed in MABE to import the spreadsheets corresponding to each classification case and evaluate the entire population of agents (artificial brains). The evolutionary process followed a sequence of iterations where brain inputs were mapped to world states (spreadsheet lines), followed by brain updates (input buffer). After completing the file reading for a specific case a score was calculated (output buffer). Once all files were evaluated, a final fitness value was computed for the evolved artificial brain. Finally, genetic algorithm operations were performed based on preset mutation rate parameters. A new sequence of evaluations was initiated with a new population obtained from the Tournament Selection optimization process (Algorithm 1). The evolved solutions of 50 replicates were exported from MABE with computed scores of the fittest individual in the population for every 10 generations.

Figure 5.8 shows the evolutionary progression for each brain output neuron (5 environment conditions) in all 12 cases, with a 95% confidence against replicates. The evolved standard ANN artificial brains have achieved the highest classification score for all conditions. Although the MB classifiers have not reached higher scores than ANNs, some replicates have approached similar solutions for some conditions such as detecting between one or two contact fingers (Figure 5.9e). The fitness value during each update was calculated using Equation 5.1, and its evolutionary history is shown in Figure 5.10. The maximum evolved fitness score was 108 points for a single replicate of ANN brain type. Since better solutions are usually identified with extensive computational runs,

a longer neuroevolution attempt was taken to further investigate the classification performance of all brain types. In this additional trials, we have run the algorithm for 40,000 generations without modifying any simulation settings. As shown in Figure 5.11, the final fitness value was $MB_w \approx 0.82$, $CGP_w \approx 0.85$, and $ANN_w \approx 0.86$.

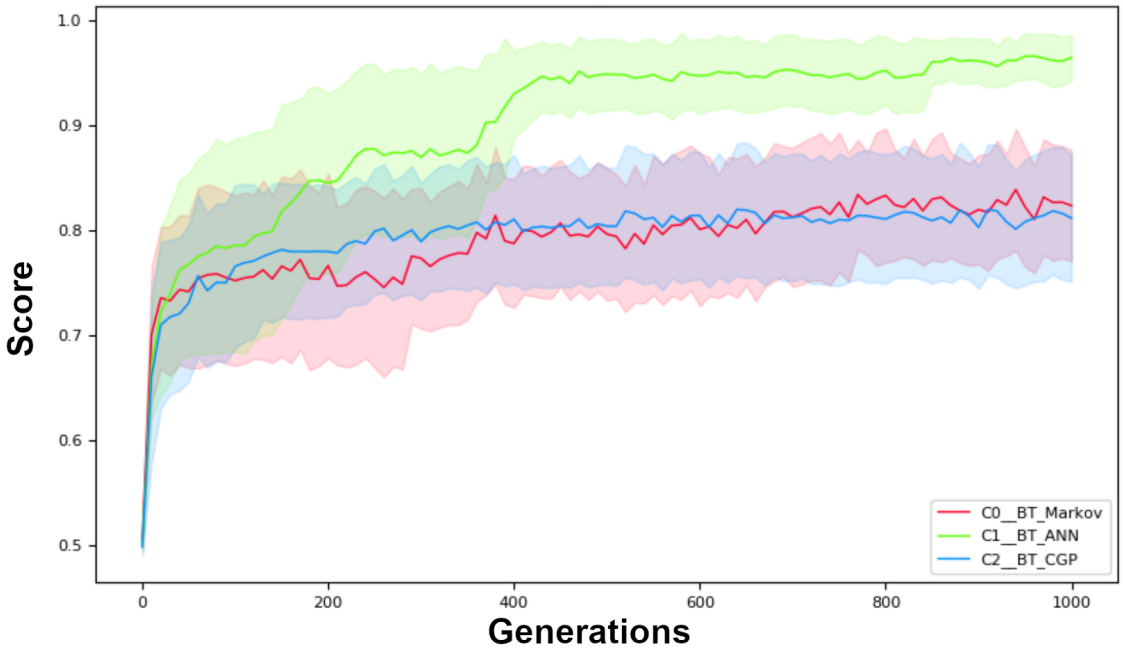

(a)

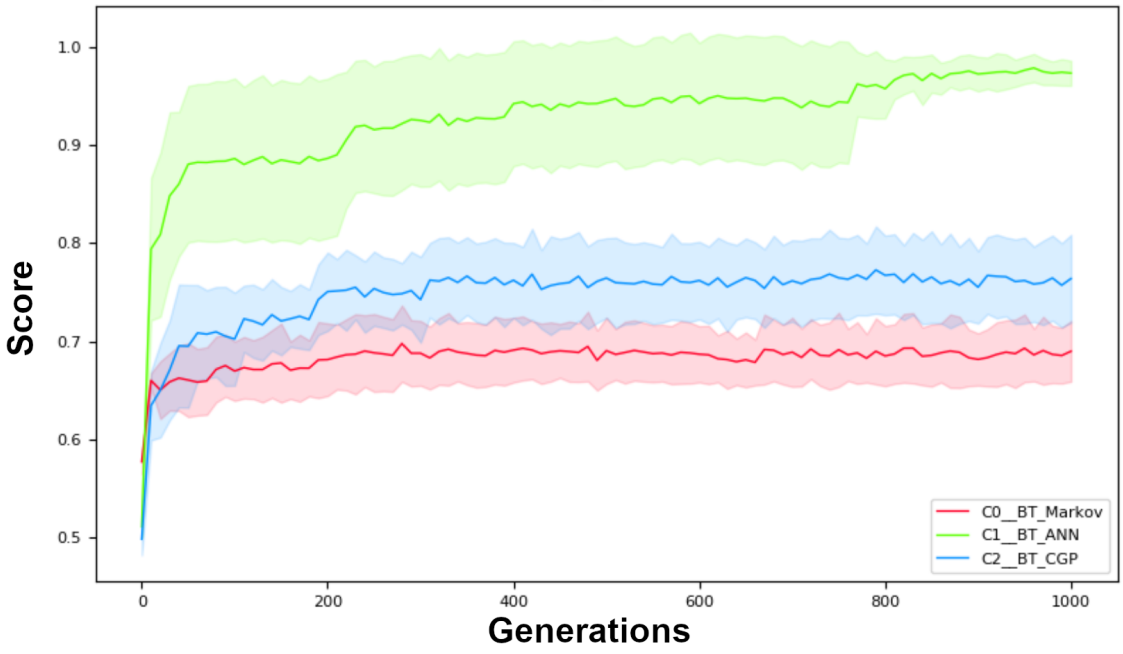

(b)

Figure 5.8: Evolutionary progression for each brain output neuron (average of all 12 cases), with a 95% confidence against replicates. Each graph shows the classification performance of a certain environment condition: (a) object shape, (b-d) object stiffness, and (e) numbers of contact fingers.

Figure 5.8 (cont'd)

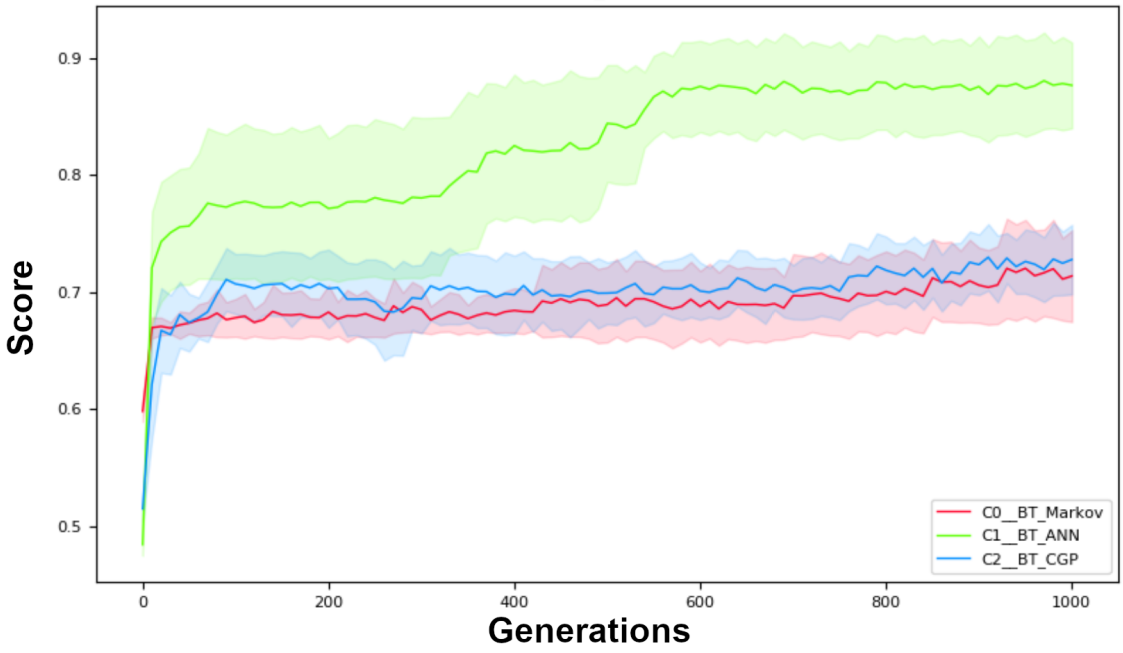

(c)

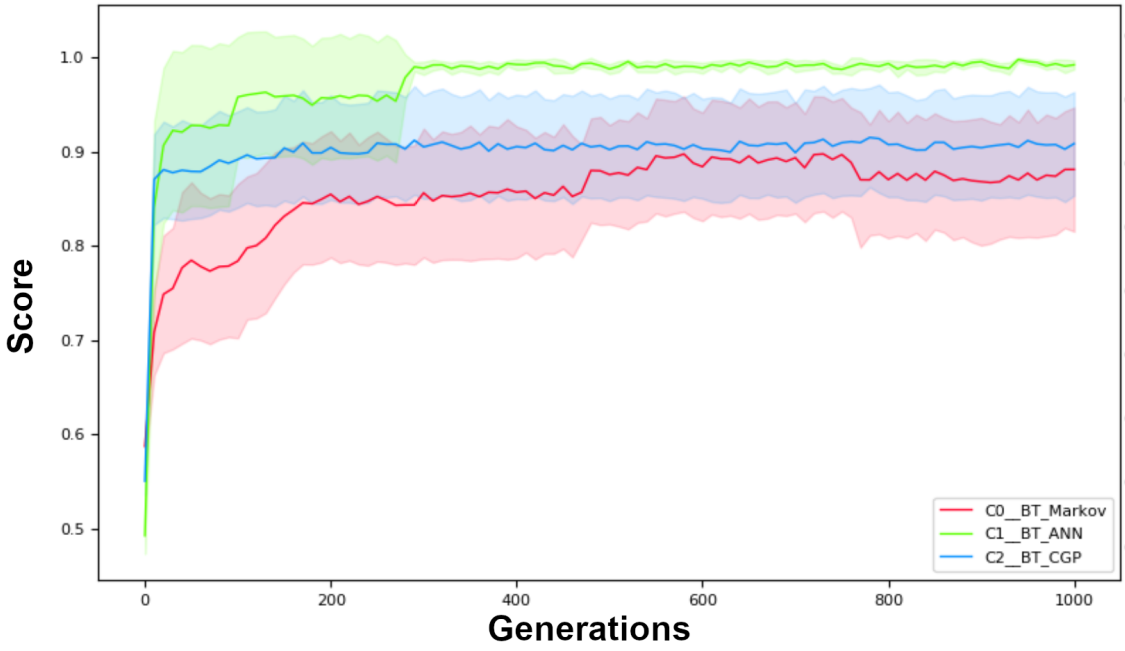

(d)

Figure 5.8 (cont'd)

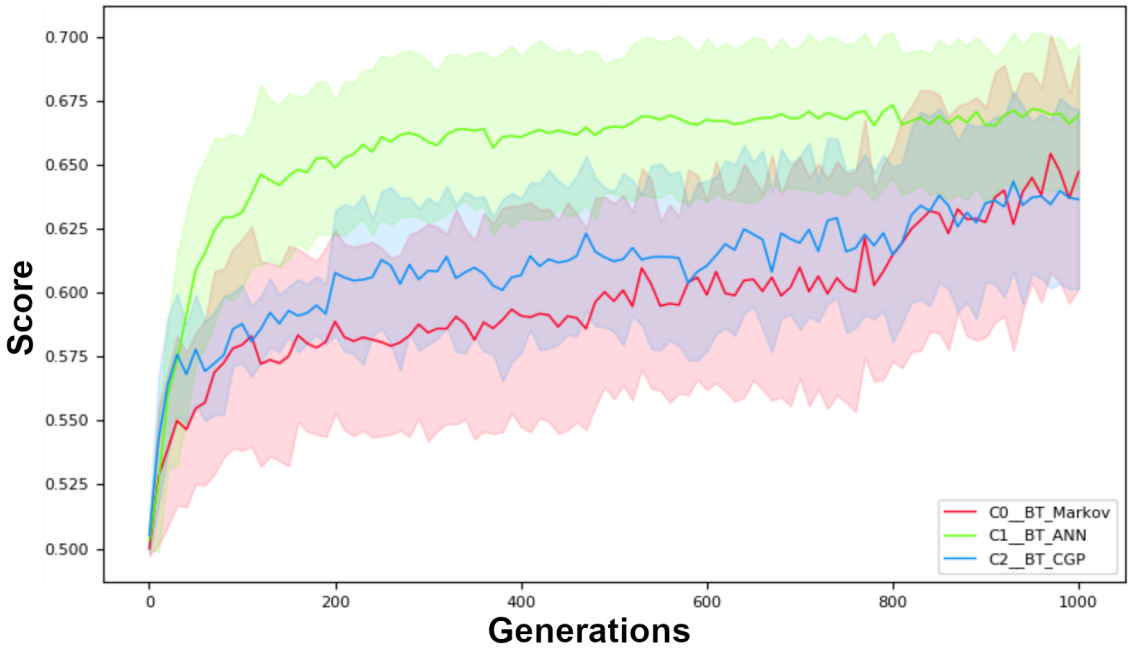

(e)

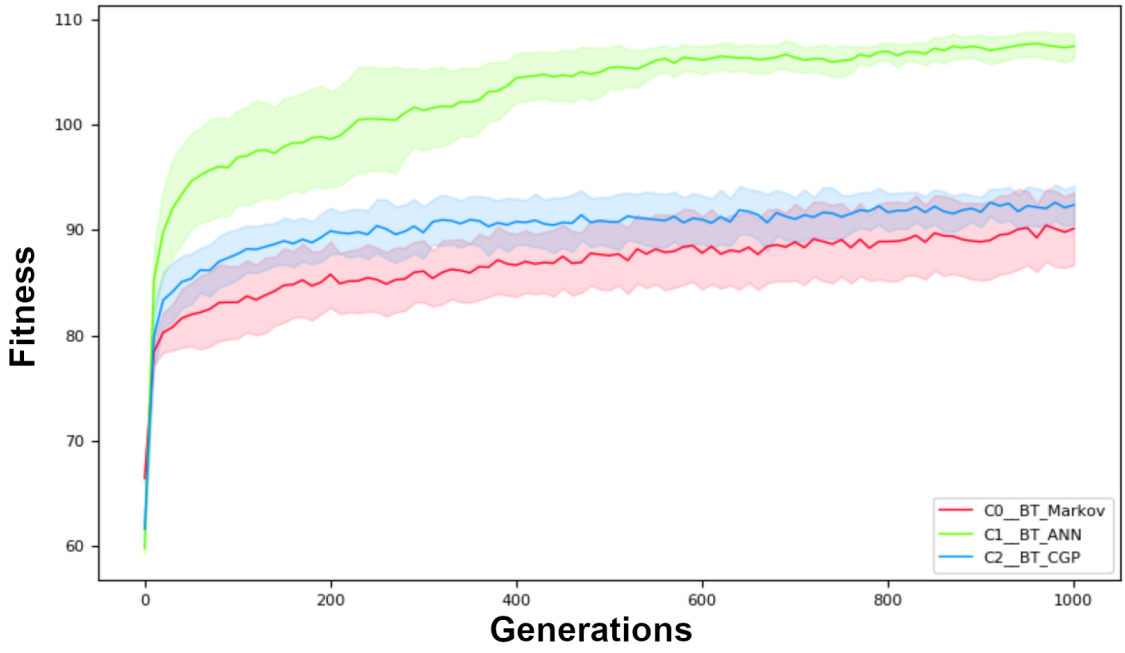

Figure 5.9: Fitness value for each evolved artificial brain type: ANNs, Markov Brains, and CGPs. The average score was computed from all 12 cases and their respective replicates.

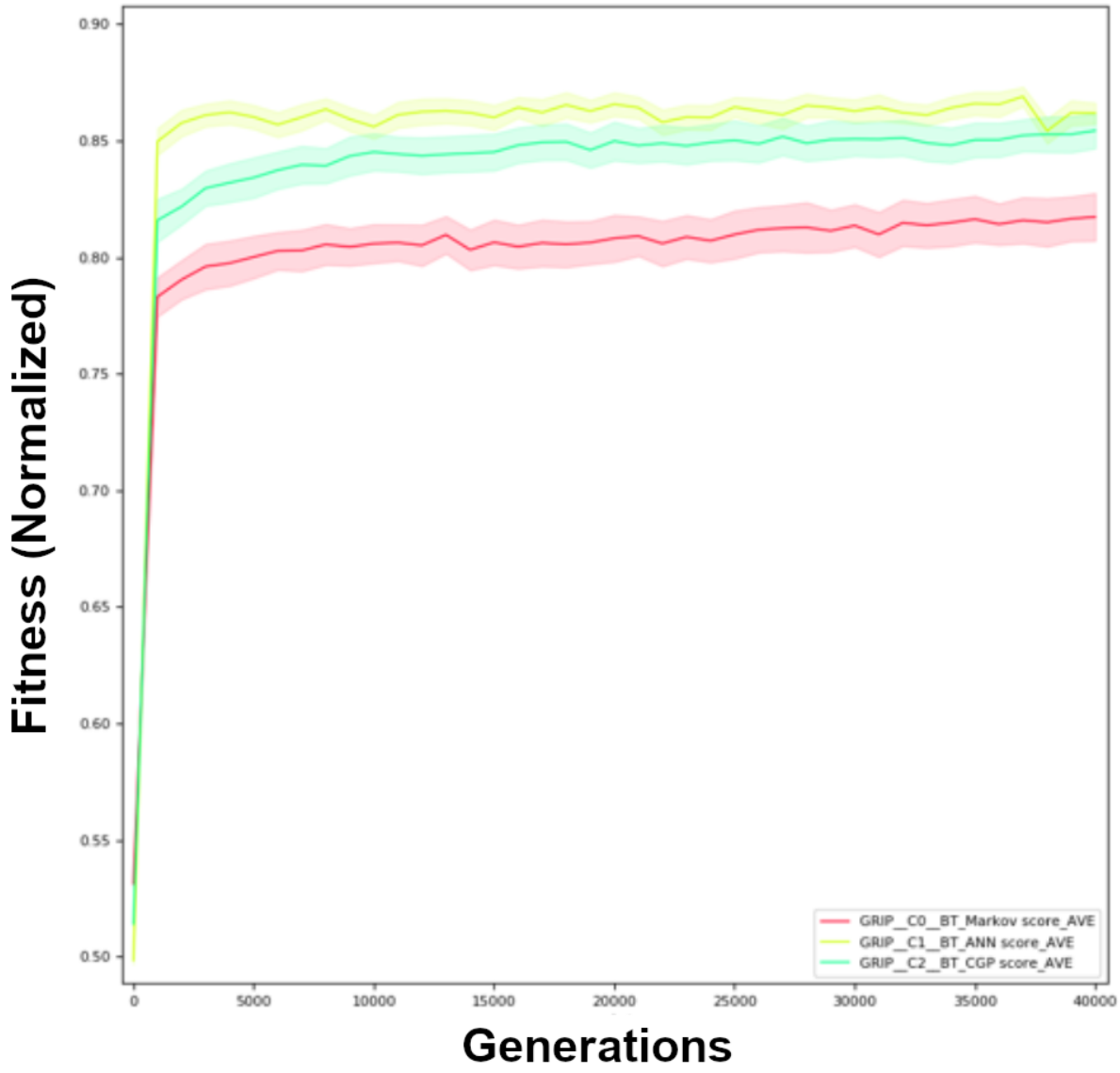

Figure 5.10: Longer neuroevolution of soft grasping classification task with varied workspace conditions for 40,000 generations.

5.3 Discussions and Future Work

We have demonstrated some initial steps as well as preliminary results for achieving real-time simulation of soft actuators with satisfactory computation time and evolution of artificial brains for

classification tasks in soft grasping using different AI models. The SOFA simulation tool allowed the use of a PID algorithm to control the bending of a SPA based on its bottom surface curvature. Moreover, we have shown that it can be used in combination with an HMI device such as a soft wearable glove to control a soft robotic gripper for grasping and manipulating objects in a simulated environment. In addition, we have exported force measurements from the tip of multiple soft fingers when in contact with objects of varied shapes and stiffnesses and used this data to train artificial brains capable of classifying diverse conditions in a robotic gripper workspace. Simulated data was imported into MABE platform for evolving standard ANNs, Markov Brains, and CGPs models to classify three different simulated conditions, object shape, object stiffness, and the number of fingers in contact during grasping. Obtained results through neuroevolution showed acceptable classification capabilities for all evolved brain types. A neuroevolution of 40,000 generations reached a level of fitness up to 0.85 (maximum value of 1) for standard ANNs, while Markov Brains models found solutions with fitness value around $\approx$0.8. While these results presented great classification characteristics in evolved artificial brains using offline method (no interface with physics engine), additional investigation is needed in order to achieve fully proprioceptive grasping with real-time feedback sensing.

An intelligent soft grasping technique should be able to recognize object shapes and stiffnesses by interacting with certain objects on strategic points that provide enough information about its workspace. Moreover, these representations of elements of the environment within which the soft gripper operates would provide adaptive behavior during decision-making tasks. A road map for achieving such goals should involve exhaustive neuroevolution training for thousands of generations with a certain level of control of the soft grippers by the artificial brains. First, an interface between SOFA and MABE is required to link output neurons to a group of actions like performing gripper rotations and individual control of the pressure level for each soft finger. Second, various pieces of information from the workspace should be passed to input neurons for detecting applied forces and changes in curvature while manipulating particular objects in each simulation iteration. A robust artificial brain should be able to decide whether to provide a few pinching actions or

completely envelope the object of interest in order to infer attributes about it. Furthermore, prior knowledge of an object characteristics would open up the prospect for robots to efficiently handle delicate objects or use tools for specific tasks. Future work should include both evolution of controllers for soft robotic hands in simulated environment as well as transferability of artificial brains with successful solutions to real-word settings, bridging the gap between simulation and reality. These enhanced manipulation skills would enable robots to have dexterity and adaptative grasping in complex workspaces alongside human beings.

Chapter 6

Summary and Discussion

Soft robotic devices can achieve suitable grasping performance with low cost materials and simple actuation mechanisms, while providing adaptivity for unstructured objects. In this thesis, we have investigated the design, fabrication and simulation of soft actuators with different geometries and materials. Our goal was to improve soft robotic grasping through a combination of soft fingers, stretchable sensors, and intelligent object classification, in order to reach a step closer to dexterity, stability and fine manipulation in varied scenarios.

A novel approach to stiffness modulation of soft actuators was achieved by using a 3D-printed CPLA-based component integrated to a SPA for variable stiffness control via electrical signals. This allowed modulation of the SPA hardness at different joints while grasping objects with irregular structure. A two-fingered gripper, composed of two CPLA-embedded SPAs, demonstrated the ability to change the grasping posture to suit the shape, size, and texture of the objects being grasped. Also, the SPA showed that it could be effectively locked in a desired bending configuration while carrying a weight, up to 800 g, even in the absence of pressure or voltage input. This work can lead to feedback control of stiffness modulated soft grippers to achieve a more arbitrary desired shape for the SPA under a fixed pressure input, and realize an even broader range of shape changes for handling different objects.

Moreover, a novel type of CNT-based strain sensors was presented, which can be embedded

in the structure of a soft robotic component. This array of strain gauges was used as a distributed sensor network along with the compliant mechanism. The sensor size and shape can be customized for many different applications. We performed experiments with the CNT-based strain sensor for detecting deformation at different locations at the bottom surface of an SPA. Both sensor measurements (strain data) and camera recording (image data) agreed with the compression (curvature) observed in the bottom layer of the SPA during positive pressure. The results provided initial steps in the implementation of a sensor array for monitoring local deformation on a soft robotic mechanism.

Furthermore, we have presented new methods for achieving 3D-printed stretchable pressure sensors and conductors using liquid metal as a circuit component for potential use in robotic hands. A PolyJet 3D-printer was used to create a microchannel structure inside the soft substrate in combination with a viscous liquid mixture for the sacrificial layer. Functional straight-shaped microchannels were fabricated with a cross-sectional area down to 150 $\times$ 150 μm. A spiral-shaped pressure sensor was designed with 350 $\times$ 350 μm microchannel cross-section and injected with liquid metal manually using syringes. Experimental results showed that the multimaterial-based sensor with the mixture of Agilus30 and VeroClear (70A Shore Hardness) and overall thickness of 1.5 mm was able to withstand high pressures up to 1 MPa. This pressure sensor is suitable for applications that require resistance to very high deformations such as in modern electronics for several fields and industry, including wearable or implantable devices, military and soft robotics.

Finally, we have performed preliminary computational exploration of intelligent grasping using 3D physics engines and tools for evolving and analyzing digital brains. In particular, we have analyzed a classification task of soft grasped objects through neuroevolution processes of various artificial brains. Simulation with the SOFA framework has been conducted to produce the emulated contact force measurements during real-time pressure control of soft fingers. The obtained data was used to train artificial neural networks by using the MABE platform to properly classify the shape and stiffness of the grasped objects. Several AI models have been computationally evolved, such as standard ANNs, Markov Brains, and CGPs, to classify three different simulated

soft grasping conditions: object's shape, object's stiffness level, and the number of fingers in contact during grasping. All evolved brain types showed acceptable classification capabilities using a neuroevolution offline method, which found solutions higher than 0.8 fitness value after 40,000 generations. These initial results provided guidelines to generate brains that can potentially store representations of elements from the soft gripper workspace and assist on dexterity and adaptive behavior during decision-making tasks in complex environments.

We expect the investigation from this dissertation to contribute new control algorithms and fabrication methods that synergistically use tactile feedback, multimodal object recognition, and stable grasp estimation, to enhance the performance of dexterous manipulation by soft robotic hands and grippers operating in the highly varying environments of the real world.

APPENDIX

APPENDIX

Table A1: Hyperelastic constitutive models for describing the mechanical behavior of incompressible rubber materials.

Hyperelastic material models	**Strain-energy functions**
Neo-Hookean	$\Psi = C_1(I_1 - 3)$ Shear Modulus: $\mu = 2C_1$
Yeoh	$\Psi = \sum_{i=1}^{3} C_i(I_1 - 3)^i$ Shear Modulus: $\mu = 2C_1$
Mooney-Rivlin	$\Psi = \sum_{i=1}^{2} C_i(I_i - 3)$ Shear Modulus: $\mu = 2(C_1 + C_2)$
Ogden	$\Psi = \sum_{i=1}^{N} \frac{\mu_i}{\alpha i}(\lambda_1^{\alpha_i} + \lambda_2^{\alpha_i} + \lambda_3^{\alpha_i} - 3)$ Shear Modulus: $\mu = \frac{1}{2}\sum_{i=1}^{N} \mu_i \alpha_i$
Arruda-Boyce	$\Psi = C_1 \sum_{i=1}^{5} \alpha_i \beta^{i-1}(I_1^i - 3^i)$ Shear Modulus: $\mu = C_1(1 + \frac{3}{5\lambda_m^2} + \frac{99}{175\lambda_m^4} + \frac{513}{875\lambda_m^6} + \frac{42039}{67375\lambda_m^8})$ $\beta = \frac{1}{\lambda_m^2}; \alpha_1 = \frac{1}{2}; \alpha_2 = \frac{1}{20}; \alpha_3 = \frac{11}{1050}; \alpha_4 = \frac{19}{7000}; \alpha_5 = \frac{1}{673750}$

Table A2: Mechanical properties of rubber-like materials used in the fabrication of soft actuators, flexible sensors and structures for soft robots.

Material	**Density** (g/cm^3)	**Durometer** (Shore)	**Tensile Strength** (N/mm^2)	**Tear Strength** (N/mm)	**Elongation at Break** (%)
Smooth-On Ecoflex 00-30	1.07	30-00	1.38	6.65	900
Smooth-On Dragon Skin 30	1.08	30A	3.45	18.90	340
Dow Corning Sylgard 184	1.03	44A	7.10	2.00	120

Table A3: The dimensions of parts in the fabricated SPA with embedded CPLA.

Parameter	**Dimension**
SPA length	140 mm
SPA width	20 mm
SPA wall thickness	2 mm
CPLA length	135 mm
CPLA width	16 mm
CPLA thickness	3 mm
Anti-slip feature thickness	2 mm

Table A4: Stiffness values of each component in the SOFA simulation.

Component	**Young Modulus (MPa)**
Soft Finger Bellows	500
Soft Finger Inextensible Layer	1500
Grasped Object = Soft	1
Grasped Object = Medium	10
Grasped Object = Hard	100

Table A5: The binary value of each correspondent workspace condition in the simulation environment of SOFA.

Condition	**Binary Value**
Object Type = Cube	0
Object Type = Sphere	1
Object Stiffness = Soft	0,0,1
Object Stiffness = Medium	0,1,0
Object Stiffness = Hard	1,0,0
Number of Contact Fingers = 1	0
Number of Contact Fingers = 2	1

Algorithm 1: Fitness Evaluation and Genetic Optimization in MABE

Require: Simulated SPA measurements from SOFA software

Input: Spreadsheet files with force values in XYZ directions at each mesh node

Output: Artificial brains genome sequence and their respective fitness scores

```
initialization;
while i ≤ maximum number of generations (updates) do
    while j ≤ maximum number of cases (files) do
        get file;
        reset brain;
        while not end of j-file do
            read line at j-file;
            update brain;
        end
        calculate output score;
    end
    compute fitness value;
    run Tournament Selection optimizer;
end
```

BIBLIOGRAPHY

BIBLIOGRAPHY

[1] D. Rus and M. T. Tolley, "Design, fabrication and control of soft robots," *Nature*, vol. 521, no. 7553, pp. 467–475, 2015.

[2] K. Suzumori, S. Iikura, and H. Tanaka, "Development of flexible microactuator and its applications to robotic mechanisms," in *Proceedings of the 14th International Conference on the Synthesis and Simulation of Living Systems (ALIFE)*, 1991, pp. 1622–1627.

[3] D. Trivedi, D. Dienno, and C. D. Rahn, "Optimal, model-based design of soft robotic manipulators," *Journal of Mechanical Design*, vol. 130, no. 9, p. 091402, 2008.

[4] M. Otake, Y. Kagami, M. Inaba, and H. Inoue, "Motion design of a starfish-shaped gel robot made of electro-active polymer gel," *Robotics and Autonomous Systems*, vol. 2-3, pp. 185–191, 2002.

[5] A. D. Marchese, C. D. Onal, and D. Rus, "Autonomous soft robotic fish capable of escape maneuvers using fluidic elastomer actuators," *Soft Robotics*, vol. 1, no. 1, pp. 75–87, 2014.

[6] E. W. Hawkes, L. H. Blumenschein, J. D. Greer, and A. M. Okamura, "A soft robot that navigates its environment through growth," *Science Robotics*, vol. 2, no. 8, p. eaan3028, 2017.

[7] S. W. Kuffler, J. G. Nicholls, and A. R. Martin, *From neuron to brain: A cellular approach to the function of the nervous system*, 2nd ed. Sinauer Associates, 1984.

[8] C. Eyzaguirre and S. W. Kuffler, "Processes of excitation in the dendrites and in the soma of single isolated sensory nerve cells of the lobster and crayfish," *The Journal of General Physiology*, vol. 39, no. 1, pp. 87–119, 1955.

[9] P. Rabischong, "Phylogeny of the hand," *The Hand*, pp. 3–7, 1981.

[10] R. Malek, "The grip and its modalities," *The Hand*, pp. 469–476, 1981.

[11] V. B. Mountcastle, *The sensory hand: neural mechanisms of somatic sensation*, 1st ed. Harvard University Press, 2005.

[12] B. Boom. Mechanoreceptors in the skin. [Online]. Available: https://biologyboom.com/wp-content/uploads/2014/07/b30_m1_022_l.jpg

[13] E. Naito, P. E. Roland, and H. H. Ehrsson, "I feel my hand moving: a new role of the primary motor cortex in somatic perception of limb movement," *Neuron*, vol. 36, no. 5, pp. 979–988, 2002.

[14] E. Naito and H. H. Ehrsson, "Somatic sensation of hand-object interactive movement is

associated with activity in the left inferior parietal cortex," *Journal of Neuroscience*, vol. 26, no. 14, pp. 3783–3790, 2006.

[15] M. R. Cutkosky, *Robotic grasping and fine manipulation*, 1st ed. Kluwer Academic Publishers, 1985.

[16] S. C. Jacobsen, E. K. Iversen, D. Knutti, R. T. Johnson, and K. B. Biggers, "Design of the Utah/MIT dextrous hand," in *Robotics and Automation (ICRA), 1986 IEEE International Conference on*, 1986, pp. 1520–1532.

[17] E. Brown, N. Rodenberg, J. Amend, A. Mozeika, E. Steltz, M. R. Zakin, H. Lipson, and H. M. Jaeger, "Universal robotic gripper based on the jamming of granular material," *Proceedings of the National Academy of Sciences*, vol. 107, no. 44, pp. 18 809–18 814, 2010.

[18] K. C. Galloway, K. P. Becker, B. Phillips, J. Kirby, S. Licht, D. Tchernov, R. J. Wood, and D. F. Gruber, "Soft robotic grippers for biological sampling on deep reefs," *Soft Robotics*, vol. 3, no. 1, pp. 23–33, 2016.

[19] P. Polygerinos, Z. Wang, K. C. Galloway, R. J. Wood, and C. J. Walsh, "Soft robotic glove for combined assistance and at-home rehabilitation," *Robotics and Autonomous Systems*, vol. 73, pp. 135–143, 2015.

[20] H. In, B. B. Kang, M. Sin, and K.-J. Cho, "Exo-Glove: a wearable robot for the hand with a soft tendon routing system," *IEEE Robotics & Automation Magazine*, vol. 22, no. 1, pp. 97–105, 2015.

[21] C. Choi, W. Schwarting, J. DelPreto, and D. Rus, "Learning object grasping for soft robot hands," *IEEE Robotics and Automation Letters*, vol. 3, no. 3, pp. 2370–2377, 2018.

[22] B. S. Homberg, R. K. Katzschmann, M. R. Dogar, and D. Rus, "Robust proprioceptive grasping with a soft robot hand," *Autonomous Robots*, pp. 1–16, 2018.

[23] C. Duriez, "Control of elastic soft robots based on real-time finite element method," in *2013 IEEE international conference on robotics and automation*. IEEE, 2013, pp. 3982–3987.

[24] A. D. Marchese, K. Komorowski, C. D. Onal, and D. Rus, "Design and control of a soft and continuously deformable 2D robotic manipulation system," in *2014 IEEE international conference on robotics and automation (ICRA)*. IEEE, 2014, pp. 2189–2196.

[25] V. Vikas, P. Grover, and B. Trimmer, "Model-free control framework for multi-limb soft robots," in *2015 IEEE/RSJ International Conference on Intelligent Robots and Systems (IROS)*. IEEE, 2015, pp. 1111–1116.

[26] N. Lu and D.-H. Kim, "Flexible and stretchable electronics paving the way for soft robotics," *Soft Robotics*, vol. 1, no. 1, pp. 53–62, 2014.

[27] D. Qi, K. Zhang, G. Tian, B. Jiang, and Y. Huang, "Stretchable electronics based on pdms

substrates," *Advanced Materials*, p. 2003155, 2020.

[28] H. Wu, T. W. Odom, D. T. Chiu, and G. M. Whitesides, "Fabrication of complex three-dimensional microchannel systems in PDMS," *Journal of the American Chemical Society*, vol. 125, no. 2, pp. 554–559, 2003.

[29] S. Sareh, A. Jiang, A. Faragasso, Y. Noh, T. Nanayakkara, P. Dasgupta, L. D. Seneviratne, H. A. Wurdemann, and K. Althoefer, "Bio-inspired tactile sensor sleeve for surgical soft manipulators," in *2014 IEEE International Conference on Robotics and Automation (ICRA)*. IEEE, 2014, pp. 1454–1459.

[30] C. Suh, J. C. Margarit, Y. S. Song, and J. Paik, "Soft pneumatic actuator skin with embedded sensors," in *2014 IEEE/RSJ International Conference on Intelligent Robots and Systems*. IEEE, 2014, pp. 2783–2788.

[31] G. M. Whitesides, "The origins and the future of microfluidics," *Nature*, vol. 442, no. 7101, p. 368, 2006.

[32] D. M. Vogt, Y.-L. Park, and R. J. Wood, "Design and characterization of a soft multi-axis force sensor using embedded microfluidic channels," *IEEE sensors Journal*, vol. 13, no. 10, pp. 4056–4064, 2013.

[33] J.-B. Chossat, H.-S. Shin, Y.-L. Park, and V. Duchaine, "Soft tactile skin using an embedded ionic liquid and tomographic imaging," *Journal of Mechanisms and Robotics*, vol. 7, no. 2, p. 021008, 2015.

[34] J.-B. Chossat, Y.-L. Park, R. J. Wood, and V. Duchaine, "A soft strain sensor based on ionic and metal liquids," *IEEE Sensors Journal*, vol. 13, no. 9, pp. 3405–3414, 2013.

[35] B. E. Schubert and D. Floreano, "Variable stiffness material based on rigid low-melting-point-alloy microstructures embedded in soft poly (dimethylsiloxane)(PDMS)," *Rsc Advances*, vol. 3, no. 46, pp. 24 671–24 679, 2013.

[36] M. H. Zarifi, H. Sadabadi, S. H. Hejazi, M. Daneshmand, and A. Sanati-Nezhad, "Non-contact and nonintrusive microwave-microfluidic flow sensor for energy and biomedical engineering," *Scientific Reports*, vol. 8, no. 1, pp. 1–10, 2018.

[37] A. Koh, D. Kang, Y. Xue, S. Lee, R. M. Pielak, J. Kim, T. Hwang, S. Min, A. Banks, P. Bastien *et al.*, "A soft, wearable microfluidic device for the capture, storage, and colorimetric sensing of sweat," *Science translational medicine*, vol. 8, no. 366, pp. 366ra165–366ra165, 2016.

[38] J. Choi, D. Kang, S. Han, S. B. Kim, and J. A. Rogers, "Thin, soft, skin-mounted microfluidic networks with capillary bursting valves for chrono-sampling of sweat," *Advanced healthcare materials*, vol. 6, no. 5, p. 1601355, 2017.

[39] J. Choi, R. Ghaffari, L. B. Baker, and J. A. Rogers, "Skin-interfaced systems for sweat

collection and analytics," *Science Advances*, vol. 4, no. 2, p. eaar3921, 2018.

[40] X. Wang, R. Guo, and J. Liu, "Liquid metal based soft robotics: materials, designs, and applications," *Advanced Materials Technologies*, vol. 4, no. 2, p. 1800549, 2019.

[41] M. D. Dickey, R. C. Chiechi, R. J. Larsen, E. A. Weiss, D. A. Weitz, and G. M. Whitesides, "Eutectic gallium-indium (egain): a liquid metal alloy for the formation of stable structures in microchannels at room temperature," *Advanced Functional Materials*, vol. 18, no. 7, pp. 1097–1104, 2008.

[42] M. D. Dickey, "Stretchable and soft electronics using liquid metals," *Advanced Materials*, vol. 29, no. 27, p. 1606425, 2017.

[43] Y. Mengüç, Y.-L. Park, E. Martinez-Villalpando, P. Aubin, M. Zisook, L. Stirling, R. J. Wood, and C. J. Walsh, "Soft wearable motion sensing suit for lower limb biomechanics measurements," in *2013 IEEE International Conference on Robotics and Automation*. IEEE, 2013, pp. 5309–5316.

[44] Y. Mengüç, Y.-L. Park, H. Pei, D. Vogt, P. M. Aubin, E. Winchell, L. Fluke, L. Stirling, R. J. Wood, and C. J. Walsh, "Wearable soft sensing suit for human gait measurement," *The International Journal of Robotics Research*, vol. 33, no. 14, pp. 1748–1764, 2014.

[45] J.-B. Chossat, Y. Tao, V. Duchaine, and Y.-L. Park, "Wearable soft artificial skin for hand motion detection with embedded microfluidic strain sensing," in *2015 IEEE international conference on robotics and automation (ICRA)*. IEEE, 2015, pp. 2568–2573.

[46] F. L. Hammond, R. K. Kramer, Q. Wan, R. D. Howe, and R. J. Wood, "Soft tactile sensor arrays for force feedback in micromanipulation," *IEEE Sensors Journal*, vol. 14, no. 5, pp. 1443–1452, 2014.

[47] Y.-L. Park and R. J. Wood, "Smart pneumatic artificial muscle actuator with embedded microfluidic sensing," in *SENSORS, 2013 IEEE*. IEEE, 2013, pp. 1–4.

[48] J. Morrow, H.-S. Shin, C. Phillips-Grafflin, S.-H. Jang, J. Torrey, R. Larkins, S. Dang, Y.-L. Park, and D. Berenson, "Improving soft pneumatic actuator fingers through integration of soft sensors, position and force control, and rigid fingernails," in *2016 IEEE International Conference on Robotics and Automation (ICRA)*. IEEE, 2016, pp. 5024–5031.

[49] Y. Hao, T. Wang, Z. Xie, W. Sun, Z. Liu, X. Fang, M. Yang, and L. Wen, "A eutectic-alloy-infused soft actuator with sensing, tunable degrees of freedom, and stiffness properties," *Journal of Micromechanics and Microengineering*, vol. 28, no. 2, p. 024004, 2018.

[50] C. Ladd, J.-H. So, J. Muth, and M. D. Dickey, "3d printing of free standing liquid metal microstructures," *Advanced Materials*, vol. 25, no. 36, pp. 5081–5085, 2013.

[51] J. W. Boley, E. L. White, G. T.-C. Chiu, and R. K. Kramer, "Direct writing of gallium-indium alloy for stretchable electronics," *Advanced Functional Materials*, vol. 24, no. 23,

pp. 3501–3507, 2014.

[52] D. P. Parekh, C. Ladd, L. Panich, K. Moussa, and M. D. Dickey, "3D printing of liquid metals as fugitive inks for fabrication of 3D microfluidic channels," *Lab on a Chip*, vol. 16, no. 10, pp. 1812–1820, 2016.

[53] S. Russel and P. Norvig, *Artificial intelligence: A modern approach*, 3rd ed. Prentice Hall, 2010.

[54] S. Nolfi and D. Floreano, *Evolutionary robotics: The biology, intelligence, and technology of self-organizing machines*, 1st ed. The MIT Press, 2000.

[55] M. Dorigo, V. Trianni, E. Şahin, R. Groß, T. H. Labella, G. Baldassarre, S. Nolfi, J.-L. Deneubourg, F. Mondada, D. Floreano, and L. M. Gambardella, "Evolving self-organizing behaviors for a swarm-bot," *Autonomous Robots*, vol. 17, no. 2-3, pp. 223–245, 2004.

[56] J. Yosinski, J. Clune, D. Hidalgo, S. Nguyen, J. C. Zagal, and H. Lipson, "Evolving robot gaits in hardware: the HyperNEAT generative encoding vs. parameter optimization," in *Proceedings of the 11th European Conference on Artificial Life (ECAL)*, 2011, pp. 890–897.

[57] R. Pfeifer and J. Bongard, *How the body shapes the way we think: A new view of intelligence*, 1st ed. The MIT Press, 2006.

[58] N. Cheney, R. MacCurdy, J. Clune, and H. Lipson, "Unshackling evolution: evolving soft robots with multiple materials and a powerful generative encoding," in *Proceedings of the 15th Annual Conference on Genetic and Evolutionary Computation (GECCO)*, 2013, pp. 167–174.

[59] N. Cheney, J. Clune, and H. Lipson, "Evolved electrophysiological soft robots," in *Proceedings of the 14th International Conference on the Synthesis and Simulation of Living Systems (ALIFE)*, 2014, pp. 222–229.

[60] N. Cheney, J. Bongard, and H. Lipson, "Evolving soft robots in tight spaces," in *Proceedings of the 2015 Annual Conference on Genetic and Evolutionary Computation (GECCO)*, 2015, pp. 935–942.

[61] F. Corucci, N. Cheney, H. Lipson, C. Laschi, and J. Bongard, "Evolving swimming soft-bodied creatures," in *Proceedings of the 15th International Conference on the Synthesis and Simulation of Living Systems (ALIFE)*, 2016, p. 6.

[62] C. Majidi, "Soft robotics: a perspectivecurrent trends and prospects for the future," *Soft Robotics*, vol. 1, no. 1, pp. 5–11, 2014.

[63] R. W. Ogden, *Non-linear elastic deformations*. Courier Corporation, 1997.

[64] P. Polygerinos, N. Correll, S. A. Morin, B. Mosadegh, C. D. Onal, K. Petersen,

M. Cianchetti, M. T. Tolley, and R. F. Shepherd, "Soft robotics: Review of fluid-driven intrinsically soft devices; manufacturing, sensing, control, and applications in humanrobot interaction," *Advanced Engineering Materials*, vol. 19, no. 12, p. 1700016, 2017.

[65] C.-P. Chou and B. Hannaford, "Measurement and modeling of mckibben pneumatic artificial muscles," *IEEE Transactions on robotics and automation*, vol. 12, no. 1, pp. 90–102, 1996.

[66] A. D. Marchese, R. K. Katzschmann, and D. Rus, "A recipe for soft fluidic elastomer robots," *Soft Robotics*, vol. 2, no. 1, pp. 7–25, 2015.

[67] T. J. Wallin, J. Pikul, and R. F. Shepherd, "3D printing of soft robotic systems," *Nature Reviews Materials*, vol. 3, pp. 84–100, 2018.

[68] J. C. Breger, C. Yoon, R. Xiao, H. R. Kwag, M. O. Wang, J. P. Fisher, T. D. Nguyen, and D. H. Gracias, "Self-folding thermo-magnetically responsive soft microgrippers," *ACS applied materials & interfaces*, vol. 7, no. 5, pp. 3398–3405, 2015.

[69] T. Pinto, L. Cai, C. Wang, and X. Tan, "CNT-based sensor arrays for local strain measurements in soft pneumatic actuators," *International Journal of Intelligent Robotics and Applications*, vol. 1, no. 2, pp. 157–166, 2017.

[70] B. Mosadegh, P. Polygerinos, C. Keplinger, S. Wennstedt, R. F. Shepherd, U. Gupta, J. Shim, K. Bertoldi, C. J. Walsh, and G. M. Whitesides, "Pneumatic networks for soft robotics that actuate rapidly," *Advanced Functional Materials*, vol. 24, no. 15, pp. 2163–2170, 2014.

[71] Y. Elsayed, A. Vincensi, C. Lekakou, T. Geng, C. Saaj, T. Ranzani, M. Cianchetti, and A. Menciassi, "Finite element analysis and design optimization of a pneumatically actuating silicone module for robotic surgery applications," *Soft Robotics*, vol. 1, no. 4, pp. 255–262, 2014.

[72] R. V. Martinez, J. L. Branch, C. R. Fish, L. Jin, R. F. Shepherd, R. M. Nunes, Z. Suo, and G. M. Whitesides, "Robotic tentacles with three-dimensional mobility based on flexible elastomers," *Advanced materials*, vol. 25, no. 2, pp. 205–212, 2013.

[73] M. T. Tolley, R. F. Shepherd, B. Mosadegh, K. C. Galloway, M. Wehner, M. Karpelson, R. J. Wood, and G. M. Whitesides, "A resilient, untethered soft robot," *Soft robotics*, vol. 1, no. 3, pp. 213–223, 2014.

[74] R. K. Katzschmann, J. DelPreto, R. MacCurdy, and D. Rus, "Exploration of underwater life with an acoustically controlled soft robotic fish," 2018.

[75] N. W. Bartlett, M. T. Tolley, J. T. Overvelde, J. C. Weaver, B. Mosadegh, K. Bertoldi, G. M. Whitesides, and R. J. Wood, "A 3d-printed, functionally graded soft robot powered by combustion," *Science*, vol. 349, no. 6244, pp. 161–165, 2015.

[76] M. Wehner, R. L. Truby, D. J. Fitzgerald, B. Mosadegh, G. M. Whitesides, J. A. Lewis, and R. J. Wood, "An integrated design and fabrication strategy for entirely soft, autonomous

robots," *Nature*, vol. 536, no. 7617, pp. 451–455, 2016.

[77] A. Miriyev, K. Stack, and H. Lipson, "Soft material for soft actuators," *Nature communications*, vol. 8, no. 1, p. 596, 2017.

[78] M. Wehner, M. T. Tolley, Y. Mengüç, Y.-L. Park, A. Mozeika, Y. Ding, C. Onal, R. F. Shepherd, G. M. Whitesides, and R. J. Wood, "Pneumatic energy sources for autonomous and wearable soft robotics," *Soft Robotics*, vol. 1, no. 4, pp. 263–274, 2014.

[79] D. P. Holland, E. J. Park, P. Polygerinos, G. J. Bennett, and C. J. Walsh, "The soft robotics toolkit: shared resources for research and design," *Soft Robotics*, vol. 1, no. 3, pp. 224–230, 2014.

[80] M. Manti, V. Cacucciolo, and M. Cianchetti, "Stiffening in soft robotics: a review of the state of the art," *IEEE Robotics & Automation Magazine*, vol. 23, no. 3, pp. 93–106, 2016.

[81] M. Al-Rubaiai, T. Pinto, D. Torres, N. Sepulveda, and X. Tan, "Characterization of a 3d-printed conductive pla material with electrically controlled stiffness," in *ASME 2017 Conference on Smart Materials, Adaptive Structures and Intelligent Systems*. American Society of Mechanical Engineers, 2017, pp. V001T01A003–V001T01A003.

[82] M. Al-Rubaiai, T. Pinto, C. Qian, and X. Tan, "Soft actuators with stiffness and shape modulation using 3d-printed conductive polylactic acid material," *Soft robotics*, vol. 6, no. 3, pp. 318–332, 2019.

[83] S. Prakash and S. Kumar, "Fabrication of microchannels: A review," *Proceedings of the Institution of Mechanical Engineers, Part B: Journal of Engineering Manufacture*, vol. 229, no. 8, pp. 1273–1288, 2015.

[84] J. K. Paik, R. K. Kramer, and R. J. Wood, "Stretchable circuits and sensors for robotic origami," in *2011 IEEE/RSJ International Conference on Intelligent Robots and Systems*. IEEE, 2011, pp. 414–420.

[85] C. Majidi, R. Kramer, and R. Wood, "A non-differential elastomer curvature sensor for softer-than-skin electronics," *Smart Materials and Structures*, vol. 20, no. 10, p. 105017, 2011.

[86] Y.-L. Park, C. Majidi, R. Kramer, P. Bérard, and R. J. Wood, "Hyperelastic pressure sensing with a liquid-embedded elastomer," *Journal of Micromechanics and Microengineering*, vol. 20, no. 12, p. 125029, 2010.

[87] B.-H. Jo, L. M. Van Lerberghe, K. M. Motsegood, and D. J. Beebe, "Three-dimensional micro-channel fabrication in polydimethylsiloxane (PDMS) elastomer," *Journal of microelectromechanical systems*, vol. 9, no. 1, pp. 76–81, 2000.

[88] Y.-L. Park, B.-R. Chen, and R. J. Wood, "Design and fabrication of soft artificial skin using embedded microchannels and liquid conductors," *IEEE Sensors Journal*, vol. 12, no. 8, pp.

2711–2718, 2012.

[89] R. K. Kramer, C. Majidi, R. Sahai, and R. J. Wood, "Soft curvature sensors for joint angle proprioception," in *2011 IEEE/RSJ International Conference on Intelligent Robots and Systems*. IEEE, 2011, pp. 1919–1926.

[90] R. Habibey, A. Golabchi, S. Latifi, F. Difato, and A. Blau, "A microchannel device tailored to laser axotomy and long-term microelectrode array electrophysiology of functional regeneration," *Lab on a chip*, vol. 15, no. 24, pp. 4578–4590, 2015.

[91] A. K. Au, W. Huynh, L. F. Horowitz, and A. Folch, "3D-printed microfluidics," *Angewandte Chemie International Edition*, vol. 55, no. 12, pp. 3862–3881, 2016.

[92] R. Amin, S. Knowlton, A. Hart, B. Yenilmez, F. Ghaderinezhad, S. Katebifar, M. Messina, A. Khademhosseini, and S. Tasoglu, "3D-printed microfluidic devices," *Biofabrication*, vol. 8, no. 2, p. 022001, 2016.

[93] A. Alfadhel, J. Ouyang, C. G. Mahajan, F. Forouzandeh, D. Cormier, and D. A. Borkholder, "Inkjet printed polyethylene glycol as a fugitive ink for the fabrication of flexible microfluidic systems," *Materials & design*, vol. 150, pp. 182–187, 2018.

[94] M. O. F. Emon, F. Alkadi, D. G. Philip, D.-H. Kim, K.-C. Lee, and J.-W. Choi, "Multimaterial 3d printing of a soft pressure sensor," *Additive Manufacturing*, vol. 28, pp. 629–638, 2019.

[95] A. D. Castiaux, C. Pinger, E. A. Hayter, M. E. Bunn, R. S. Martin, and D. M. Spence, "Polyjet 3D-printed enclosed microfluidic channels without photocurable supports," *Analytical chemistry*, 2019.

[96] Y.-L. Park, B.-r. Chen, and R. J. Wood, "Soft artificial skin with multi-modal sensing capability using embedded liquid conductors," in *SENSORS, 2011 IEEE*. IEEE, 2011, pp. 81–84.

[97] H.-S. Shin, J. Ryu, C. Majidi, and Y.-L. Park, "Enhanced performance of microfluidic soft pressure sensors with embedded solid microspheres," *Journal of Micromechanics and Microengineering*, vol. 26, no. 2, p. 025011, 2016.

[98] R. C. Chiechi, E. A. Weiss, M. D. Dickey, and G. M. Whitesides, "Eutectic gallium–indium (egain): a moldable liquid metal for electrical characterization of self-assembled monolayers," *Angewandte Chemie International Edition*, vol. 47, no. 1, pp. 142–144, 2008.

[99] F. F. Abayazid and M. Ghajari, "Material characterisation of additively manufactured elastomers at different strain rates and build orientations," *Additive Manufacturing*, p. 101160, 2020.

[100] D. M. Dykstra, J. Busink, B. Ennis, and C. Coulais, "Viscoelastic snapping metamaterials," *Journal of Applied Mechanics*, vol. 86, no. 11, 2019.

[101] F. Corucci, N. Cheney, S. Kriegman, J. Bongard, and C. Laschi, "Evolutionary developmental soft robotics as a framework to study intelligence and adaptive behavior in animals and plants," *Frontiers in Robotics and AI*, vol. 4, p. 34, 2017.

[102] J. Rieffel, F. Saunders, S. Nadimpalli, H. Zhou, S. Hassoun, J. Rife, and B. Trimmer, "Evolving soft robotic locomotion in physx," in *Proceedings of the 11th annual conference companion on genetic and evolutionary computation conference: Late breaking papers*. ACM, 2009, pp. 2499–2504.

[103] G. Methenitis, D. Hennes, D. Izzo, and A. Visser, "Novelty search for soft robotic space exploration," in *Proceedings of the 2015 annual conference on Genetic and Evolutionary Computation*, 2015, pp. 193–200.

[104] F. Veenstra, J. Jørgensen, and S. Risi, "Evolution of fin undulation on a physical knifefish-inspired soft robot," in *Proceedings of the Genetic and Evolutionary Computation Conference*, 2018, pp. 157–164.

[105] INRIA. SOFA - Simulation Open Framework Architecture. [Online]. Available: https://www.sofa-framework.org/

[106] E. Coevoet, A. Escande, and C. Duriez, "Soft robots locomotion and manipulation control using fem simulation and quadratic programming," in *2019 2nd IEEE International Conference on Soft Robotics (RoboSoft)*. IEEE, 2019, pp. 739–745.

[107] G. Fang, C.-D. Matte, R. B. Scharff, T.-H. Kwok, and C. C. Wang, "Kinematics of soft robots by geometric computing," *IEEE Transactions on Robotics*, 2020.

[108] R. Deimel, P. Irmisch, V. Wall, and O. Brock, "Automated co-design of soft hand morphology and control strategy for grasping," in *2017 IEEE/RSJ International Conference on Intelligent Robots and Systems (IROS)*. IEEE, 2017, pp. 1213–1218.

[109] T. G. Thuruthel, B. Shih, C. Laschi, and M. T. Tolley, "Soft robot perception using embedded soft sensors and recurrent neural networks," *Science Robotics*, vol. 4, no. 26, 2019.

[110] A. Hintze, J. A. Edlund, R. S. Olson, D. B. Knoester, J. Schossau, L. Albantakis, A. Tehrani-Saleh, P. Kvam, L. Sheneman, H. Goldsby *et al.*, "Markov brains: A technical introduction," *arXiv preprint arXiv:1709.05601*, 2017.

[111] S. Chapman, D. Knoester, A. Hintze, and C. Adami, "Evolution of an artificial visual cortex for image recognition," in *Artificial Life Conference Proceedings 13*. MIT Press, 2013, pp. 1067–1074.

[112] R. S. Olson, J. H. Moore, and C. Adami, "Evolution of active categorical image classification via saccadic eye movement," in *International Conference on Parallel Problem Solving from Nature*. Springer, 2016, pp. 581–590.

[113] C. Bohm and A. Hintze, "MABE (Modular Agent Based Evolver): A framework for digital